PACIFIC EARTHQUAKE ENGINEERING RESEARCH CENTER

Estimation of Shear Demands on Rock Socketed Drilled Shafts subjected to Lateral Loading

Pedro Arduino

Long Chen

Christopher R. McGann

Department of Civil and Environmental Engineering
University of Washington

PEER Report No. 2018/06
Pacific Earthquake Engineering Research Center

PEER 2018/06
December 2018

Estimation of Shear Demands on Rock-Socketed Drilled Shafts subjected to Lateral Loading

Pedro Arduino
Long Chen
Christopher R. McGann

Department of Civil and Environmental Engineering
University of Washington

PEER Report No. 2018/06

Pacific Earthquake Engineering Research Center
Headquarters, University of California, Berkeley
December 2018

ABSTRACT

This report presents results of an evaluation study on the applicability of current design procedures (based on p-y curves) to the analysis of large-diameter shafts socketed in rock, and the identification of enhanced moment transfer mechanisms not considered in current design methodologies. For this purpose simplified models, and possible three-dimensional (3D) finite-element method (FEM) models are studied to shed some light on the response of drilled shafts socketed in rock. A parametric study using p-y and considering a wide range of rock properties and rock-socket depths, different criteria to define the soil and rock p-y curves, different beam theories, and different interface frictional resistances are presented and compared with 3D FEM simulations. A new element is discussed to account for the shaft toe and underlain rock interaction, which could provide benefit to reduce shear demands when the socket is shallow.

ACKNOWLEDGMENTS

The authors would like to acknowledge the generous support of the Pacific Earthquake Engineering Research Center. This research was funded under Grant number NC9M01. The opinions, findings, conclusions, or recommendations expressed in this publication are those of the author(s) and do not necessarily reflect the views of the study's sponsor (PEER) or the Regents of the University of California.

CONTENTS

LIST OF TABLES

LIST OF FIGURES

1 Introduction

1.1 BACKGROUND

Drilled shafts socketed in rock are widely used as foundations for bridges and other important structures. They are also used to stabilize unsafe slopes and landslides. The main loads applied to drilled shafts are axial (compressive or uplift) as well as lateral loads with accompanying moments. Although there exist several analysis and design methods especially for rock-socketed drilled shafts subjected to lateral loading, these methods tend to be based on simplified assumptions that have not been thoroughly validated with field load tests and advanced numerical analysis. This is particularly true when considering large lateral loads and moments acting on drilled shafts.

Several studies have shown Turner (2006) that p-y analysis of laterally loaded rock-socketed shafts result in unexpectedly high values of shear and question whether the results are realistic. In particular, when a rock socket in relatively strong rock is subjected to a lateral load and moment at its head, values of shear near the top of the socket may be much higher than the applied lateral load. This result is accepted given the bending moment and load transfer mechanisms that are commonly used in these types of analyses. When the lateral load has a high moment arm, such as occurs in an elevated structure, the lateral load transmitted to the top of the drilled shaft may be small or modest, but the moment may be relatively large. The principal mechanism of moment transfer from the shaft to the rock mass is through the mobilized lateral resistance. If a large moment is transferred over a relatively short depth, the lateral resistance is also concentrated over a relatively short length of the shaft, resulting in shear loading that may be higher in magnitude than that of the lateral load.

Although this mechanism and resulting shear demands are valid in most cases, there is some question whether the high values of shear predicted by p-y methods of analysis for such cases exist in reality or are artifacts of the analysis. Some designers suggest that the structural model of the shaft does not account properly for shear deformation, resulting in unrealistically high shear values. Other suggest the p-y curves commonly used for drilled shafts socketed in rock are not accurate and some researchers indicate that different load-transfer mechanisms are also possible.

A correct evaluation of shear demand at soil–rock socket interfaces is important since the shear demand may govern the drilled shaft reinforced-concrete structural design. When shear occurs in addition to axial compression, the section is then checked by comparing the factored shear loading with the factored shear resistance. The need for additional transverse reinforcement, beyond that required for compression, can be determined using conventional design procedures as presented in the AASHTO LRFD Bridge Design Specifications (2004). For the majority of rock-socketed shafts, the transverse reinforcement required to satisfy compression criteria combined with the shear resistance provided by the concrete will be adequate to resist the factored shear loading without the need for additional transverse reinforcement. However, in cases where high lateral loads or bending moments are to be distributed to the ground over a relatively small distance, factored shear forces may be high and the shaft dimensions and reinforcement may be governed by shear; i.e., a short stubby socket in high-strength rock. In these cases, the designer is challenged to provide a design that provides adequate shear resistance without incurring excessive cost increases or adversely affecting constructibility by constricting the flow of concrete.

To handle high shear loading in the reinforced-concrete shaft, the designer has several options: (1) increase the shaft diameter, thus increasing the area of shear-resisting concrete; (2) increase the shear strength of the concrete; or (3) increase the amount of transverse reinforcing, either spiral or ties, to carry the additional shear. Although each option has advantages and disadvantages, in general they result in more expensive structures and in some case designs that cannot be constructed.

In this context, the main objective of this research is to better understand the shear and bending demands in rock-socketed drilled shafts subjected to lateral loads and establish design recommendations for this case. For this purpose, this report reviews current practices for the design of socketed piles in rock, takes advantage of current 3D finite element modeling (FEM) capabilities to evaluate shear demands on drilled shafts, and compares these results with solutions obtained using conventional methods based on p-y curves. Today's FEM codes allow for accurate evaluation of the response of rock-socketed piles subjected to lateral loads. Of particular importance for the socketed pile case is the estimation of shear and bending demands near the soil–rock interface. This localized response can be investigated using refined meshes, fiber beam elements and appropriate contact elements. In contrast, conventional Beam on Nonlinear Winkler Foundation (BNWF) methods based on p-y curves, although very useful, suffer from the fact that the p-y curves are often based on findings from experimental tests performed on small-diameters piles and soil conditions that do not account for the presence of a soil–rock interface. They also presume a load transfer mechanism based solely on shear forces; thus, they tend to overestimate shear and bending demands and result in overly designed drilled shafts. Although some tests have been performed with the specific goal of estimating the response of socketed piles, more research is needed. Among them recent studies on this topic several reports and papers are relevant, including:

- V. Ramakrishna K. Rajagopal, and S. Karthigeyan, (2004), Behavior of Rock Socketed Short Piles under Lateral Loads, IGC 2004.
- C.F. Leung and Y.K. Chow, (2008) Performance of Laterally Loaded Socketed Piles.
- K. Yang, (2006), Analysis of Laterally Loaded Shafts in Rocks, PhD dissertation, University of Akron, Akron.

This research builds on these studies and aims to evaluate the applicability of current design procedures (based on p-y curves) to the analysis of large diameters shafts socketed in rock, and then identify enhanced moment transfer mechanisms not considered in current design methodologies. This study is similar to recent research topics conducted at the Pacific Earthquake Engineering Research Center (PEER). In recent years, PEER has funded several projects on the validation and application of p-y curves to the analysis of pile foundations subjected to lateral spreading and related loading conditions. These studies have included analytical/numerical analyses as well as experimental (field /centrifuge) tests. In addition, the California Department of Transportatoin (Caltrans) has been supporting experimental and analytical studies on pile–soil interaction for many years. In this context, this project is focused on rock-socketed piles subjected to lateral loads. Results from this project may provide better insight on how to address this problem.

1.2 OBJECTIVES

This research addresses the following main topics, the findings of which will be summarized and recommendations presented in a final report:

- Review of recent work on design of rock-socketed drilled shafts
- Review of current numerical modeling strategies for predicting demands on rock-socketed drilled shafts
- Development of OpenSees 3D models to represent the soil–rock–pile domain
- Parametric analysis using different rock-socketed drilled shaft configurations and soil–rock material properties
- Identification and evaluation of enhanced moment transfer mechanisms to resist lateral loads and external bending moments
- Development of practical design recommendations based on the improved modeling strategies

1.3 REPORT ORGANIZATION

This report is organized as follows:

1. Chapter 2 presents different modeling strategies to address the problem of rock-socketed shafts subjected to lateral loads. These models range from simple beams with simple boundary conditions and beams supported with nonlinear springs (i.e., BNWF), to 3D FEM models where the pile is represented either by beam elements or brick elements.

2. Chapter 3 presents a parametric analysis study using different p-y spring formulations for different rock conditions and comparisons with results obtained from OpenSees simulations using 3D brick elements to represent the rock.

3. Chapter 4 presents the formulation of a 3D finite element to describe the resisting force and bending moment at the shaft toe as a function of vertical deformation and rotation. The model accounts for nonuniform distribution of stresses and toe partial uplift. The chapter also includes notes on the numerical implementation and results for selected cases.

4. Chapter 5 presents a summary, conclusions and recommendations for future research.

2 Modeling Rock-Socketed Drilled Shafts

2.1 INTRODUCTION

The response of a drilled shaft socketed in rock subjected to lateral loads can be investigated using different models including p-y based models and 3D FEM models. p-y based models, i.e., BNWF models, have been extensively studied and are extremely easy to use. Three-dimensional FEM models are computationally more expensive but, when properly done, provide more detailed information compared to BNWF p-y methods. Independent of the method used, defining proper boundary conditions are important to accurately represent this problem. This chapter begins with a presentaton of simplified basic models and then introduces possible 3D FEM models that could shed some light to the response of drilled shafts socketed in rock.

2.2 PROBLEM STATEMENT AND BASIC MODELS

Figure 2.1 shows a schematic of a typical drilled shaft socketed in rock subjected to lateral loads. In the figure, the drilled shaft is represented by a cylinder subjected to axial and lateral loads. The upper section of the shaft is surrounded by soil (represented in yellow in the figure) and its lower section is embedded (socketed) in rock (represented in brown in the figure). Typical models used to characterize this problem range from very simple beam models to advanced 3D FE models. The use of beam theory is natural for this type of problem. By using traditional formulations (e.g., Bernoulli or Timoshenko) and adequate boundary conditions (representing the rock region or socket), it is possible to obtain a first representation of the response of socketed drilled shafts subjected to lateral loads. Although very simple, these models can help identify possible mechanisms that may be useful in understanding the response of rock-socketed drilled shafts. Figure 2.2 shows three of these simple beam models where the soil is completely eliminated (assuming its resistance negligible compared to that of the rock), and the rock is represented by different boundary conditions. The model in Figure 2.2(a) represents the socketed portion of the shaft with an enlarged beam section with much larger area and moment of inertia than the rest of the beam. The model in Figure 2.2(b) assumes the beam is completely restrained (fixed) in displacements and rotations at some points along the socketed section, and the model in Figure 2.2(c) uses a series of pins that prevent displacement in the horizontal direction at localized points to represent the restraint imposed by the socketed section.

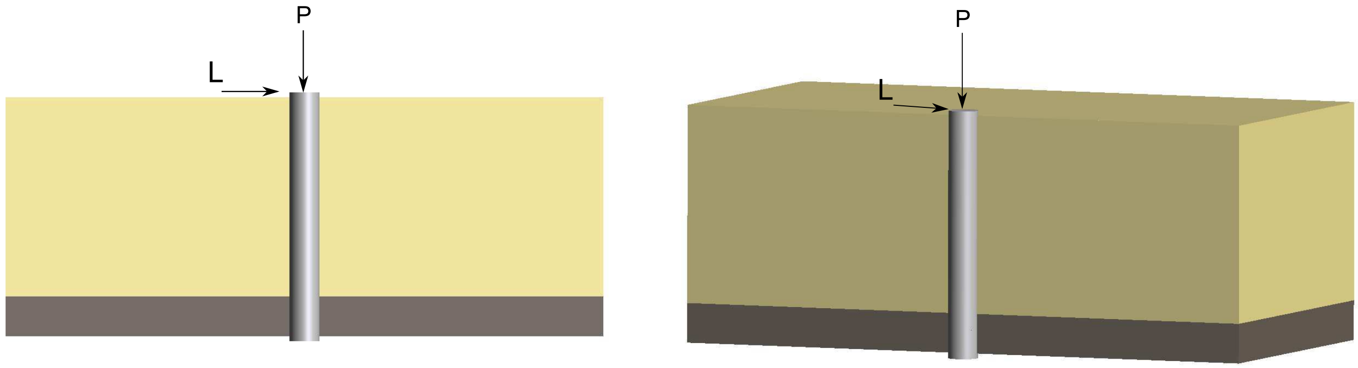

Figure 2.1 Schematic drawing of rock-socketed shaft under lateral load.

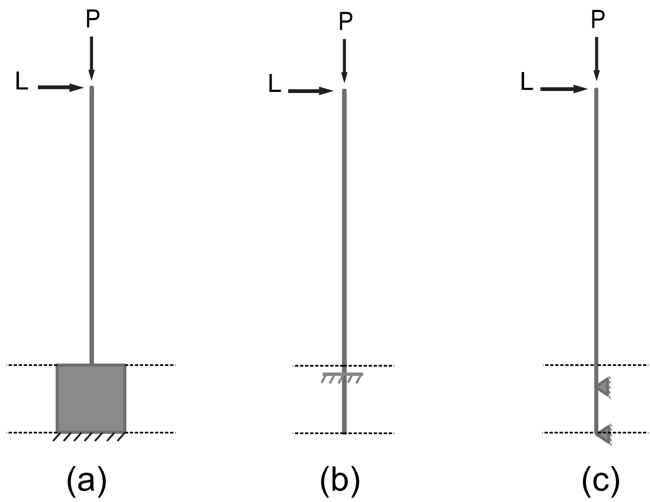

Figure 2.2 Simple models.

Figures 2.3 and 2.4 show more advanced models. Here, the drilled shaft is again represented by beam elements, and the rock is represented by either nonlinear p-y springs (shown in Figure 2.3) or 3D solid elements (shown in Figure 2.4). When representing the rock using 3D solid elements, it is important to properly represent the pile–rock interface, including the development of frictional forces along the interface surface and the possibility of gap formation. This requires special contact formulations (in this case between beam and solid elements). Finally, since in this case the soil portion is not modeled, the resulting overburden stress must be replaced by distributed loads at the top of the rock socket (representing the self-weight of the soil). Although the models that include 3D FEM elements are computationally more expensive than those shown in Figure 2.2, they can provide more accurate results.

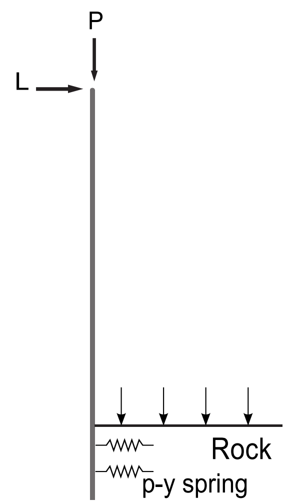

Figure 2.3 Simple beam model(using p-y springs to represent rock).

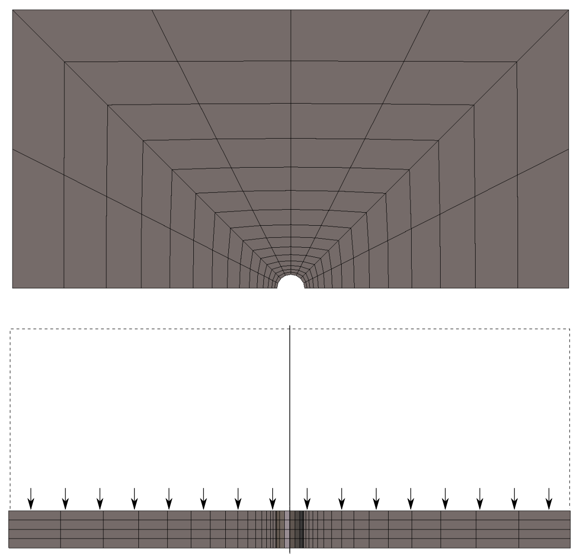

Figure 2.4 Simple beam model(using 3D solid elements to represent rock).

As mentioned before, beam elements are a natural choice to represent slender structural elements (e.g., piles or drilled shafts). However, it is also possible to represent the shaft using solid elements. Figure 2.5 shows a model where both the drilled shaft and the rock are modeled using 3D brick elements. These models are computationally more expensive and require many more elements to properly capture the response of the structural system, particularly in the case when representing the nonlinear response of reinforce concrete (i.e., nonlinear response of steel and concrete). These models also require special contact formulations to capture the response at the shaft–rock interface (in this case using solid-to-solid contact elements).

Finally, when the stiffness and strength of the soil above the rock are relevant, e.g., when the relative stiffness and strength of the soil and the rock are of the same order, it is necessary to include the soil in the model representation. Figure 2.6 shows one such model where the soil is represented by nonlinear p-y springs (i.e., BNWF). Figures 2.7 and 2.8 show two cases where the shaft is represented by beam and solid elements, respectively, and the soil is represented by 3D solid elements. These models are computationally more expensive.

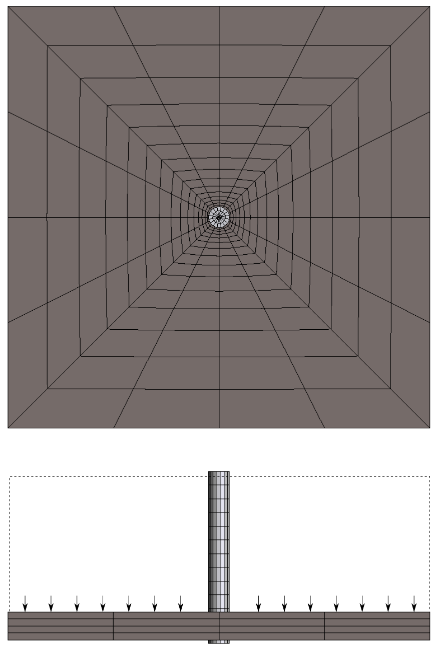

Figure 2.5 3D simple model using solid elements to model beam.

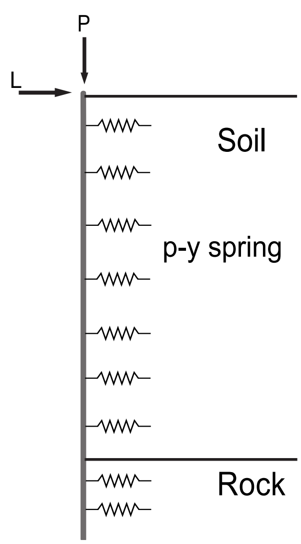

Figure 2.6 Beam elements representing the shaft and p-y springs representing the soil and rock (BNWF).

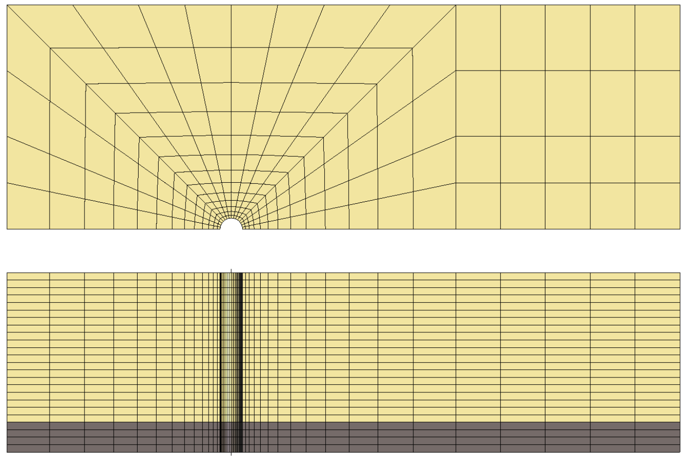

Figure 2.7 Beam elements representing the shaft and solid elements for the soil and rock.

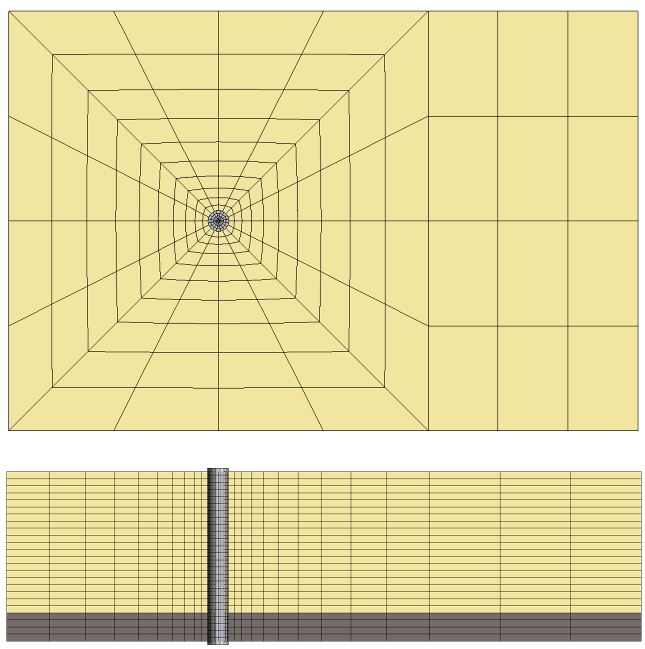

Figure 2.8 3D solid model representing the drilled shaft, the soil and the rock.

All these models have strengths and weaknesses. An evaluatoin of the merits of each modeling strategy in the light of shear and bending demands estimated by each model is presented below. First, a typical geometry, rock and soil conditions, shaft characteristics, and rock-socket depths are presented.

2.3 MODEL GEOMETRY AND MATERIAL PROPERTIES

The basic geometry chosen to analyzed this problem includes a 1.5-m drilled shaft embedded in a 10-m soil profile underlain by rock. Different socket depths (ranging from 0.5 to 2.0 m) are considered to evaluate the socket response. The properties of the rock material are based on each of five parameter sets shown in Table 2.1 that represent a wide variety of rock properties. These parameters are based on assumed rock mass rating (RMR) values and the work of Bieniawski (1989). Elastic modulus values for the rock mass, E_m, were computed from the assumed RMR values using the relation proposed by Serafim and Pereira (1983) where

$$E_m = 10^{\left(\frac{\text{RMR}-10}{40}\right)} \tag{2.1}$$

Geologic Strength Indices (GSI) are determined from the RMR values as

$$\text{GSI} = \begin{cases} \text{RMR} - 5 & \text{for RMR} \geq 23 \\ 9 \ln Q' + 44 & \text{for RMR} < 23 \end{cases} \tag{2.2}$$

and

$$Q' = \left(\frac{\text{RQD}}{J_n}\right)\left(\frac{J_r}{J_a}\right) \tag{2.3}$$

and the assumed values of $J_n = 4$, $J_r = 3$, and $J_a = 1$ represent the hypothetical number, roughness, and fill conditions, respectively, of the joints in the model class V rock mass. The m_i terms in Table 2.1 were estimated based on rock class from the table provided in Hoek et al. (1995). These rock properties can be used as a proxy to determine constitutive parameters for the constitutive model used to represent the rock and soil. In this study, a simple Drucker-Prager (DP) and J2 models were used to capture the rock response. Table 2.2 shows the resulting DP model parameters for a rock type I. Two approaches were used to model the drilled shaft: elastic and fiber section. Table 2.3 shows the material properties for the drilled shaft using an elastic approach. These material properties represent typical properties for reinforced concrete. A fiber section was used to incorporate the nonlinear cross-sectional behavior of the drilled shaft. The fiber section model was discretized into subregions, which were assigned uniaxial constitutive models to represent the corresponding concrete and steel portions. A 1.5-m diameter section with 32-mm longitudinal reinforcement and 18-mm spiral ties, with equivalent elastic properties to the elastic section, adapted from McGann (2013) (Fig. 2.10) is used to represent typical behavior of plastic sections. The material properties for this fiber section are shown in Table 2.4. The uniaxial constitutive model assumed for the reinforcing steel was a bilinear plasticity model. The parameters defining the constitutive response of this model were the steel yield stress, σ_y, elastic modulus, E_s, and strain hardening ratio, b. The compressive behavior of the concrete constitutive model was based on the work of Kent and Park (1971). The tensile behavior for the concrete constitutive model was simplified, with a limited linear elastic capacity followed by linear softening. Figure 2.9 shows the moment-curvature response of a single drilled shaft.

Table 2.1 Basic properties assumed for rock materials in numerical models.

	Class Number				
	I	II	III	IV	V
RMR	90	70	50	30	10
q_u (MPa)	250	175	75	35	5
RQD (%)	95	80	60	35	15
E_m (GPa)	100	32	10	3.2	1
GSI	85	65	45	25	24
m_i	23	12	10	7	5

Table 2.2 Drucker-Prager assumed for materials in numerical models.

	K(MPa)	G(MPa)	$\sigma_Y(KPa)$	ρ	Unit Weight(kN/m^3)	Poisson's Ratio
Rock	67000	40000	12720	0.681	22.0	0.25
Soil	220	95	100	0.362	17.0	0.3

Table 2.3 Beam properties assumed for elastic section in numerical models.

	K(MPa)	G(MPa)	Radius(m)	I(m^4)	Poisson Ratio
Beam	17750	8192.3	0.75	0.249	0.3

Table 2.4 Concrete and steel material properties in drilled shaft fiber section model.

Concrete Properties						Steel Properties		
$f'_c(kPa)$	ϵ_c	$f'_{cu}(kPa)$	ϵ_{cu}	$f_t(kPa)$	$E_t(MPa)$	$\sigma_y(MPa)$	$E_s(GPa)$	b
24525	0.003	4905	0.0368	3070	-2039	412	200	0.001

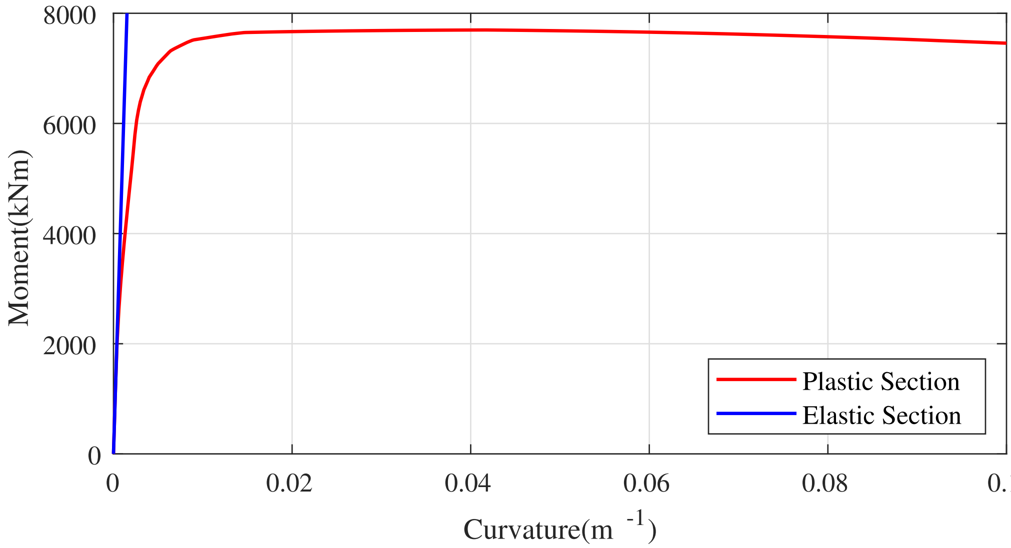

Figure 2.9 Model moment-curvature response for single drilled shaft using different sections.

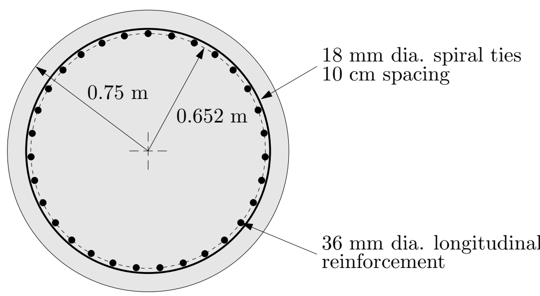

Figure 2.10 Details of the model drilled shaft cross-section using fiber section(after McGann (2013)).

2.4 LOADING CONDITIONS

In this study, all models were subjected to axial and lateral loads. The axial loads represented self-weight and possible superstructure demands. This study considered vertical loads values ranging from 0 MN to 56.6 MN. The lateral demand was applied in the form of horizontal displacements enforced at the top of the shaft. In all cases a monotonic horizontal displacement time history spanning from 0.0 m to 0.5 m was used.

2.5 COMPUTATIONAL TOOL

2.5.1 OpenSees Finite Element Analysis Platform

The opensource finite element framework OpenSees (`http://opensees.berkeley.edu`) was used in this research for all simulations. OpenSees was developed at PEER for use in structural and geotechnical simulations in one, two, and three dimensions. OpenSees's programming framework uses object-oriented programming in C++. The software architecture was created in a manner such that there is separation of the materials and elements, thus, new materials or elements can be added without modification to existing material and element classes. Several finite elements and constitutive models are available in OpenSees that are particularly suited for this research project. They include:

- advanced fiber beam elements that capture the linear and nonlinear response of structural elements (shafts, columns, beams)
- conventional and efficient brick elements (e.g. Stabilized Single Point Brick- SSPBrick) that capture the response of the rock and soil domains
- solid-to-solid 3D contact elements that capture the shaft-to-rock interface response when the shaft and soil are modeled using solid elements. These elements allow for gap formation and the development of frictional forces
- beam-to-solid 3D contact elements that capture the shaft-to-rock interface response when the shaft is represented by beam elements and the rock by solid elements; this element also allows for gap formation and the development of frictional forces
- beam-end contact elements that capture the shaft-to-rock interface response at the bottom of the shaft when the shaft is represented by beam elements and the rock by solid elements
- uniaxial p-y, t-z, and q-z springs based on API criteria
- uniaxial nonlinear materials to capture the nonlinear response of steel and concrete (including confined and unconfined concrete)
- 3D pressure-dependent and pressure-independent constitutive models that capture the behavior of soil (including sands and clays)
- Drucker-Prager and J2 plasticity constitutive models to capture the behavior of the rock
- A general array of possible boundary conditions that allow for independent constraints (loads or displacements) of any type and in any direction

More information of OpenSees's modeling capabilities, element and material constitutive models characteristics, and user manual (including useful examples) can be found at (`http://opensees.berkeley.edu/wiki/`).

2.5.2 Pre– and Post–Processing of Simulated Data

The commercial program GiD (`http://gid.cimne.upc.es/`) is used during this research as a graphical pre- and post-processor for OpenSees. All of the input information for the problem, including everything from mesh generation to material and element assignments, is performed using this tool. This information is then transferred to an input file and run in OpenSees. After reformatting, the OpenSees recorder data can be interpreted by GiD, allowing for the program to function as a visual post-processor for OpenSees, which while perfectly functional as a FE solver, has only limited visual capabilities. The ability of GiD to function in this capacity greatly simplifies the creation of the input files and visualization of the results.

2.6 MODEL EVALUATION

This section presents numerical results obtained using the different modeling strategies mentioned in section 2.3 for the drilled shaft and loading condition indicated in section 2.4. The motivation of these analyses is to evaluate and compare each modeling strategy to identify their strengths and weaknesses. An ancillary objective is to identify possible resisting mechanisms appropriate for an accurate evaluation of shear demands in rock-socketed drilled shafts.

2.6.1 Simple Beam Models

This set of simple models is intended to provide a preliminary framework for the development of shear demands in rock-socketed shafts. These models are not expected to provide a complete and accurate representation of the problem; however, they may serve to shed some light on fundamental phenomena inherent to the problem. In all cases, it is assumed that the effect of the soil is negligible compared to that of the rock.

Beam with Different Cross-Sectional Properties

The first model strategy attempts to capture the shaft response using an enlarged cross-sectional area to represent the rock-socket section of the shaft, with larger area and moment of inertia near this section. Figures 2.11 and 2.12 show results for two different cross-sectional properties. Note that the larger the cross section, the better the predicted deformation (deformed shape). Independent of the size of the cross section, the shear demand stays constant and the bending moment increases with beam length. This model strategy produces correct deformations but fails to capture the shear and bending moment demands in the socketed portion.

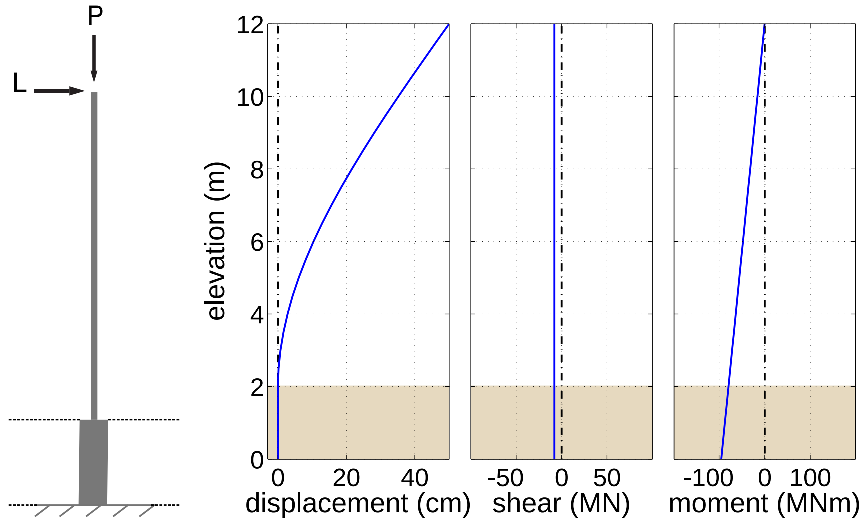

Figure 2.11 Displacement, shear, and bending moment in shaft with section radius ratio = 10 (freehead).

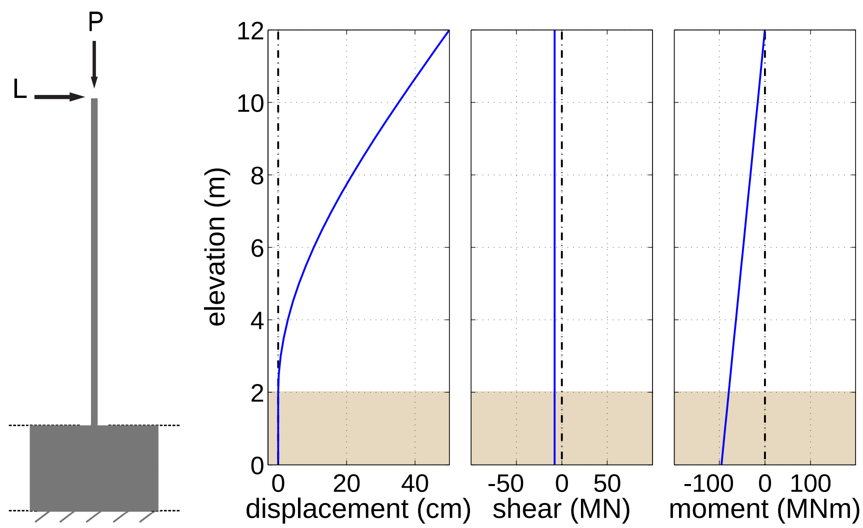

Figure 2.12 Displacement, shear, and bending moment in shaft with section radius ratio = 100 (freehead).

Beam with Fixed Support

The second model strategy uses fixities to represent the rock–socket constraint. The use of total or partial fixities to represent the socketed portion of the shaft is common in geotechnical practice and can help identify the shear and bending demands above the fixity point but fail to indicate how the resisting shear force and bending moment are generated (or resisted) in the socketed portion of the shaft. Figures 2.13 and 2.14 show results for two fixity locations: (a) at the bottom of the shaft;

and (b) near the top of the socketed section. The first case produces incorrect results in terms of displacements, shear, and bending demands above the fixity point. The second case produces realistic displacements, and accurate shear forces and bending moment above the fixity point, but does not provide any information on how these demands are resisted (i.e., the computational tool only provides reaction forces at the fixity point). Although very simple and considering its limitations, the use of fix supports is commonly used in structural design to represent pile foundations (rock socketed or not), with an appropriate fixity depth being key.

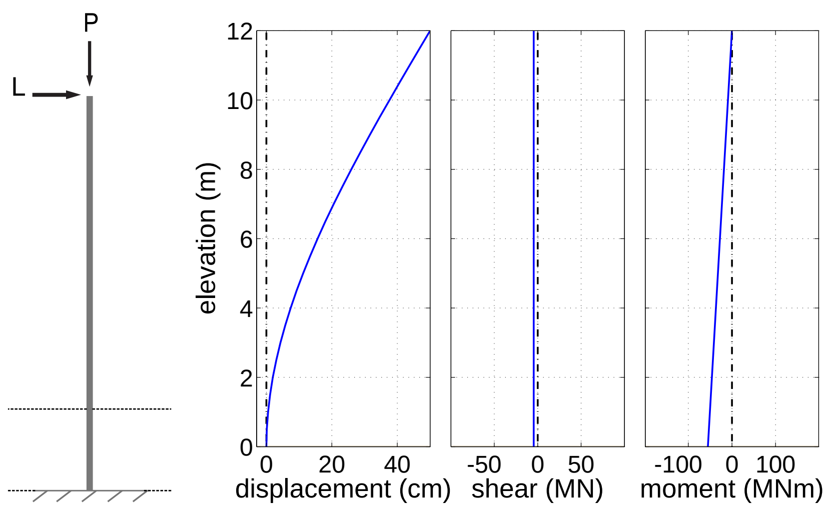

Figure 2.13 Shear and bending moment in shaft with fixed support at the bottom of rock layer (freehead).

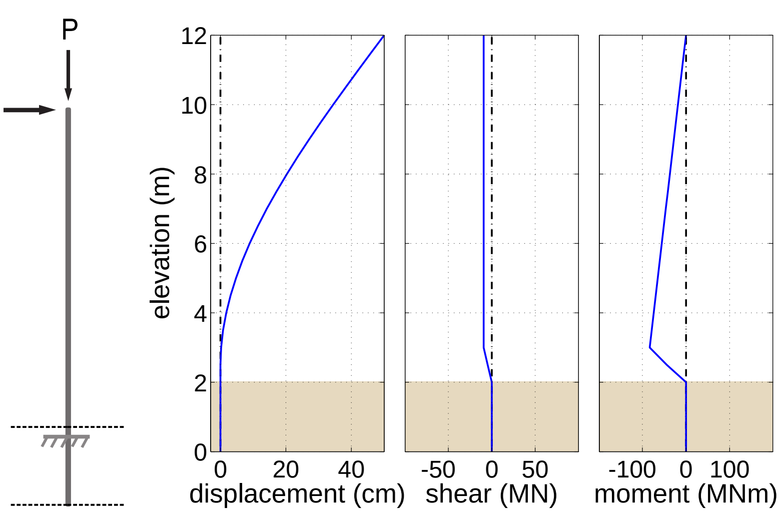

Figure 2.14 Shear and bending moment in shaft with fixed support at 2 m from bottom (freehead).

Beam with Pinned Supports

The use of pinned supports to model the rock-socketed portion of the shaft render the first model capable of generating a resisting mechanism for balancing the bending demands that develop at the top of the socketed portion. The reactions at the pins (shear forces) generate a bending moment opposite in direction to the one at the top of the socketed portion of the shaft. The resisting moment in this model is based solely on shear forces. Figures 2.15, 2.16, and 2.17 show results for models with pinned supports placed at different spacings: as the spacing is reduced, the required shear force needed to balance the bending moment at the top of the socketed section increases. This model presumes the rock is infinitely strong and does not deform. Although very simple, this model provides some insight and possible problems that may arise for those models that use pins or localized springs to represent the rock-socketed condition. This model implies that the stronger the rock and the smaller the socketed depth the larger will be the shear demand. Table 2.5 shows a summary of the results for cases 1 to 7 described above in terms of shear force at the top of the shaft, maximum shear force, and shear force ratio.

Table 2.5 Shear force summary for simple beam model cases.

	Shear Force at Top of Shaft (MN)	Maximum Shear Force (MN)	Shear Force Ratio
Case 1	7.94	7.94	1.00
Case 2	7.94	7.94	1.00
Case 3	4.59	4.59	1.00
Case 4	9.26	9.26	1.00
Case 5	6.62	33.08	5.00
Case 6	7.30	91.26	12.50
Case 7	7.61	192.97	25.35

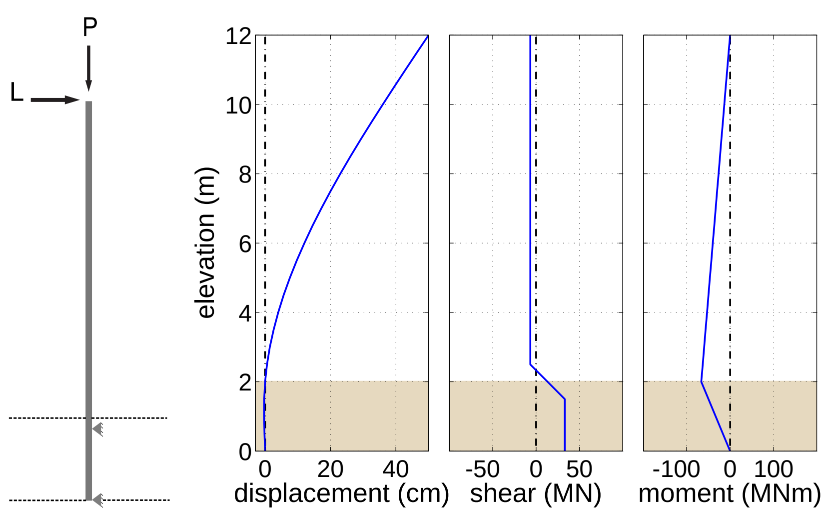

Figure 2.15 Shear and bending moment in shaft with two pined supports (freehead).

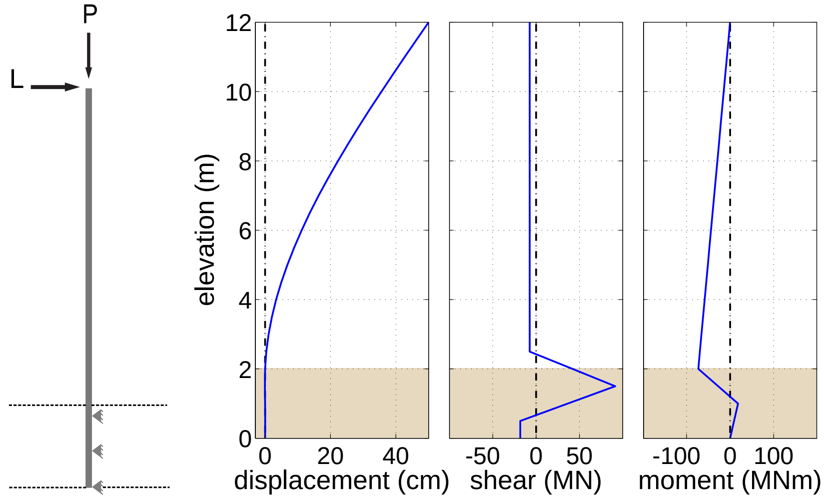

Figure 2.16 **Shear and bending moment in shaft with three pined supports (freehead).**

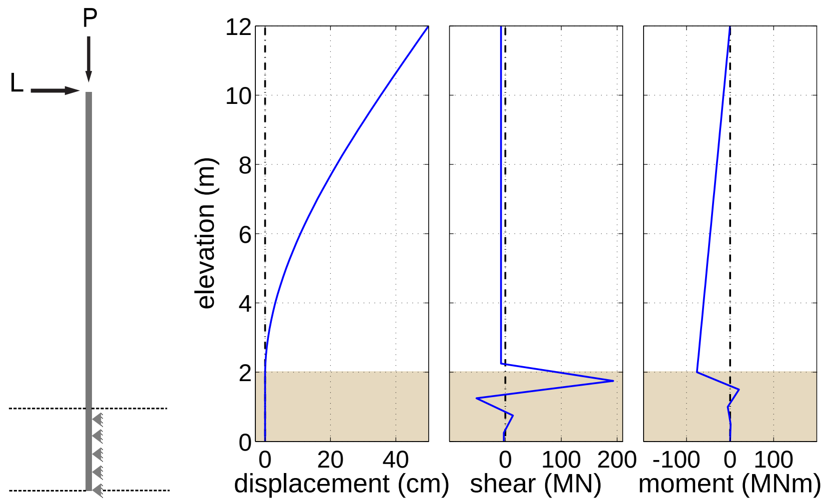

Figure 2.17 **Shear and bending moment in shaft with five pined supports (freehead).**

2.6.2 BNWF p-y Analysis

A natural extension to the last model is to replace the pins by springs. These springs can be linear or nonlinear. Springs that characterize the lateral response between piles and soils are usually referred as p-y springs. p-y springs are commonly used in geotechnical engineering and foundation design, and have been researched extensively through physical and numerical tests. Over the last three decades many analytical and empirical p-y spring formulations have been proposed, several of which are widely accepted and used in design. Although p-y springs where originally developed for piles, they are also used in connection with drilled shafts. In general, p-y springs are defined in terms of an initial stiffness (k) and an ultimate capacity (p_{ult}). Models for different soils (clays and sands) and rocks have been proposed for monotonic and cyclic loads. Although these springs are uni-axial in nature, they are intended to capture the 3D interaction effects between the foundation (pile or drilled shaft) and the surrounding soil/rock, including the formation of soil wedges and relative soil movement around the pile and possible gapping. Their use in connection with 2D plane strain FEM analysis is limited since they represent a 3D phenomena. Their use in 3D FEM analyses is also limited since they are applied in a single direction. A thorough description of p-y curves is beyond the scope of this study. For more information on p-y curves for soils the interested reader is referred to the work by Reese and Van Impe (2001) and to the works by Gabr et al. (2002) and Liang et al. (2009) for p-y curves for rocks.

It is very common to use p-y springs in practice, and extensive research has been done to define p-y springs for rocks. Therefore, a complete parametric study using recently proposed p-y curves for rocks, including different rock types and socket depths, is presented in Chapter 3. This section is limited to showing the effect of using p-y springs for rocks and soils in the response of rock socketed drilled shafts (in terms of shear and bending moment demands) and evaluate its benefits compared to the other modeling techniques presented in this chapter. Consider the same drilled shaft analyzed in the previous section and shown in Figure 2.6, where the soil and rock are replaced by p-y springs. Figure 2.19 shows results for the case where the effect of the soil is assumed negligible (no soil p-y springs) and the rock is very strong (using p-y spring properties for rock Type I). Similar to the pinned model case, the results show the development of a large shear demand near the soil/rock interface (larger than the applied lateral force). As was the case for the previous models, this modeling strategy assumes that the resisting mechanism is based solely on shear forces (and resulting bending moment) and neglects the contribution of vertical loads and friction. Similarly, Figure 2.20 shows results for the case where the soil is included in the analysis (in terms of p-y springs for a soft soil). As expected, the shear and bending demands are slightly smaller than for the other case (since resistance develops along the portion of the shaft embedded in soil) but the differences are negligible. Maximum shear forces and shear stress ratios for the last two cases are presented in Table 2.6 showing these differences. Obviously, as the stiffness and strength of the soil increases relative to the rock, the shear demand at the soil–rock interface decreases. Because the springs deform, the shear demands are smaller than those obtained using pins (independent of spring spacing since the p-y material properties are defined per unit length).

Table 2.6 Shear force summary for p-y curve cases.

	Shear Force at Top of Shaft (MN)	Maximum Shear Force (MN)	Shear Force Ratio
Case 1	7.25	69.23	9.55
Case 2	9.70	56.15	5.79

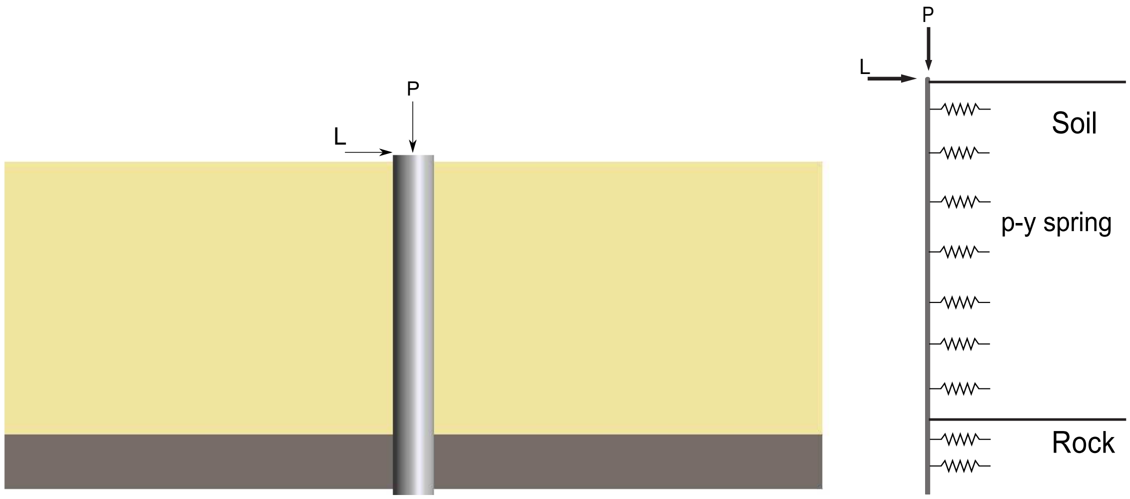

Figure 2.18 Schematic drawing of rock-socketed shaft under lateral load p-y model.

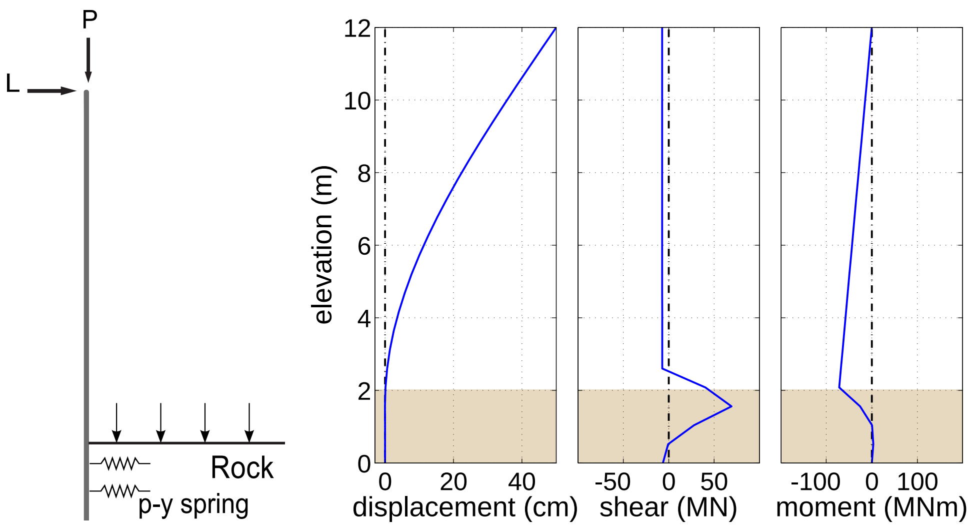

Figure 2.19 Shear and bending moment in shaft using API p-y curves (freehead, rock only).

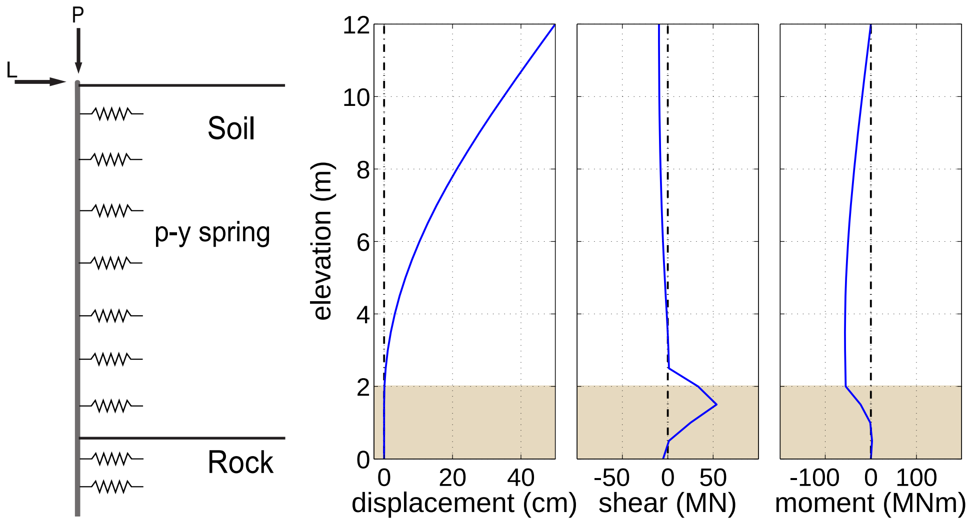

Figure 2.20 Shear and bending moment in shaft using API p-y curves (freehead).

2.6.3 3D FEM Analysis Using Beam and Solid Elements

A more fundamental treatment of the problem requires a 3D finite element analysis, including a better representation of the socket geometry, rock response, and shaft–rock interface behavior. For this purpose, beam elements and/or solid elements can be used to represent the shaft, and advanced constitutive models can be used to represent the rock and the soil.

3D Analysis using a Beam Element to Represent the Shaft

Figure 2.21 shows a model where the shaft is represented by beam elements, the rock by 3D brick elements, the shaft–rock interface by beam-to-solid contact elements, and the soil effect is assumed negligible. The beam element representing the shaft bottom is restrained in the vertical direction (although free in all other directions where the rotation may be free or fixed), with a 0.5-m lateral displacementapplied at the top of the shaft.

Figure 2.22 shows results for a 2.0-m-deep rock socket using 0.5-m elements; Figure 2.23 shows results for the same case using a refined mesh with 0.25-m elements. Both cases assume no frictional resistance develops at the rock–shaft interface. The figures and the results in Table 2.7(a) and (b) show shear demands slightly smaller than those obtained using p-y springs, both in terms of shear force distribution and maximum shear force. Figure 2.24 and 2.25 depict results for the same case using a plastic-fiber section instead of an elastic section. The "plastic hinge," where curvature exceeds the curvature corresponding to the peak moment shown in Figure 2.9, is marked in red. In this particular case, the plastic hinge developed at the soil–rock interface, and the maximum shear force (shown as case (c) in Table 2.7) was significantly reduced.

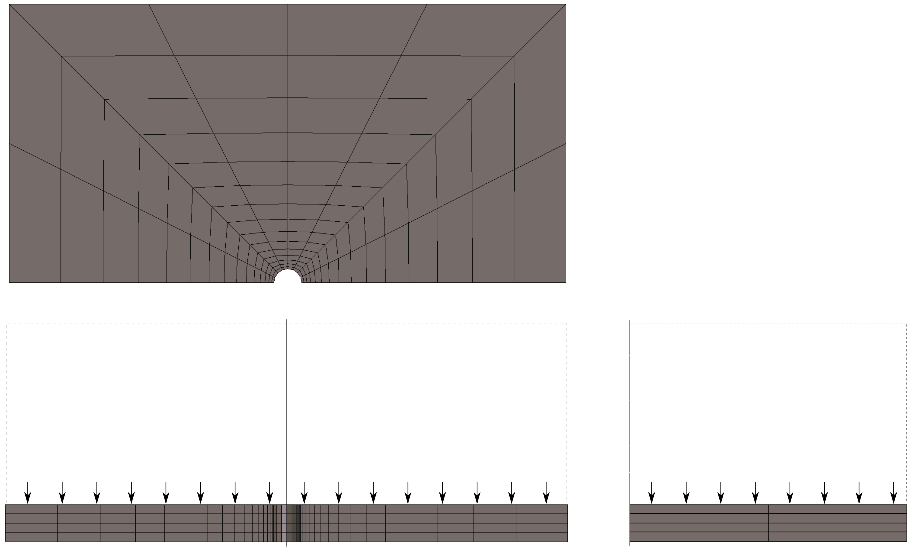

Figure 2.21 Overview of 3D FEM mesh for 2-m rock profile.

Table 2.7 Shear force summary for 3D cases (shaft and rock).

	Shear Force at Top of Shaft (MN)	Maximum Shear Force (MN)	Shear Force Ratio
(a)	6.71	47.81	7.12
(b)	6.66	60.00	9.01
(c)	0.73	8.16	11.1
(d)	6.71	48.83	7.27
(e)	6.71	47.81	7.12
(f)	6.97	55.28	7.93

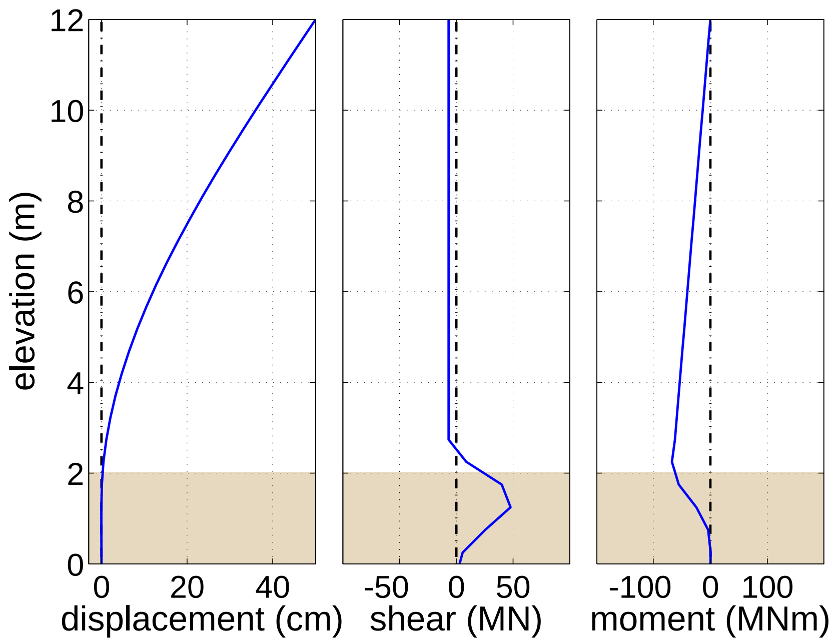

Figure 2.22 Shear and bending moment in shaft with rock layer only (Case a: freehead, element size = 0.5).

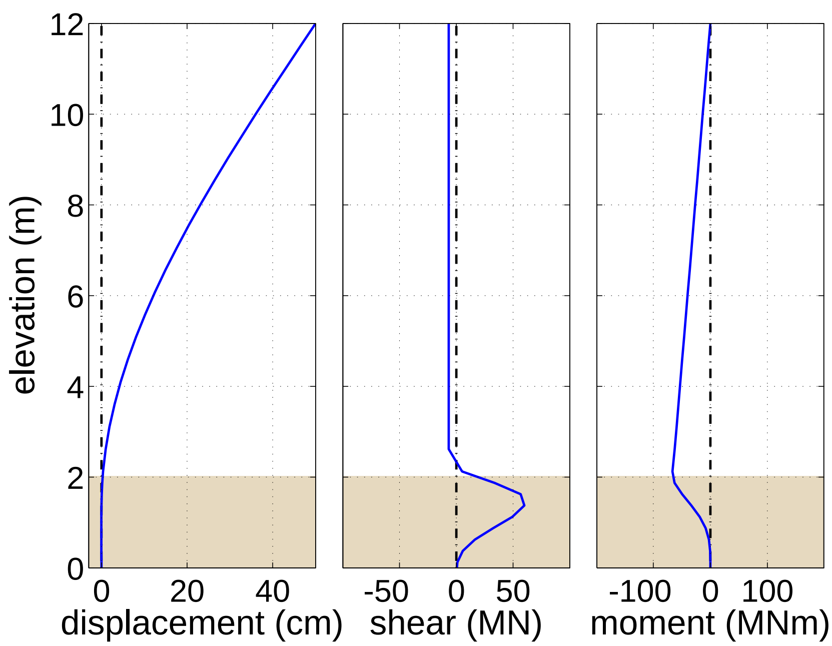

Figure 2.23 Shear and bending moment in shaft with rock layer only (Case b: freehead, element size = 0.25).

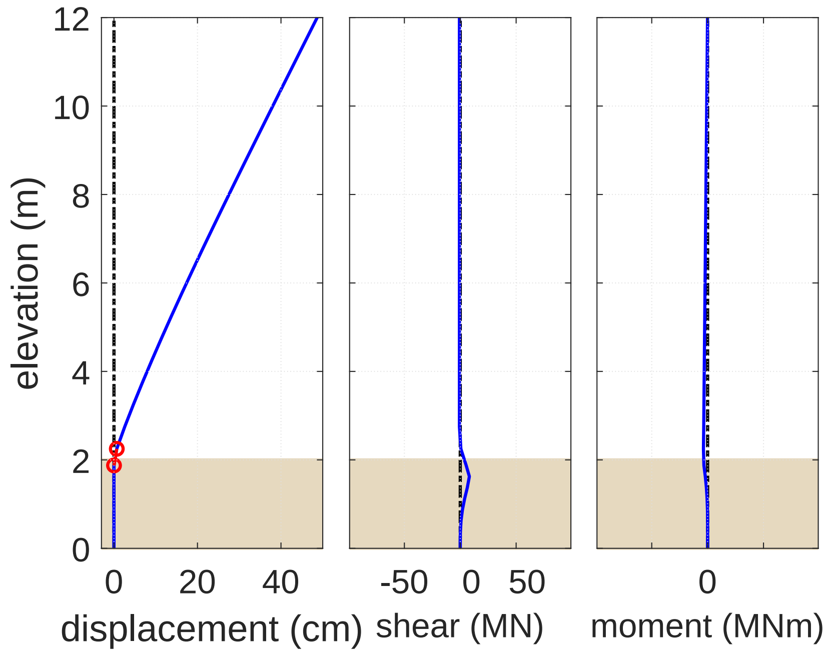

Figure 2.24 Shear and bending moment in shaft with rock layer only (Case c: freehead, using plastic-fiber section).

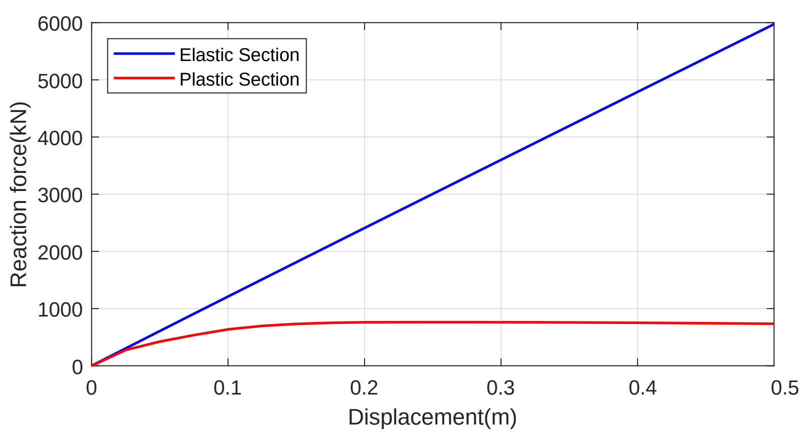

Figure 2.25 Comparison of reaction force at top of the shaft between elastic section and fiber section.

Figure 2.26 shows results for a case where the bottom of the beam is fixed in displacement (for all directions) and rotation.In this case, a fraction of the bending moment is transmitted to the bottom (that is fixed), reducing the shear forces required to equilibrate the system. Figures 2.27 and 2.28 show results for a case where frictional resistance is accounted for. The frictional resistance was modeled using a Coulomb-type contact interface model that allows for elastic slip (sticking) and plastic slip (sliding). Control of the interface frictional behavior required definition of an interface stiffness, (G_0), and an interface strength, μ. Two extreme cases are considered here: one with small interface stiffness (large sticking) and one with a very large stiffness (negligible sticking, i.e., extensive sliding). For this particular case (i.e., 2.0-m-deep socket), a small interface stiffness G_o produces very similar results to those obtained assuming a frictionless case. The case with large interface stiffness, G_o, produces larger shear demands comparable to those produced using p-y springs. Table 2.7(e) and (f) shows maximum shear forces and shear–stress ratios of these last two cases.

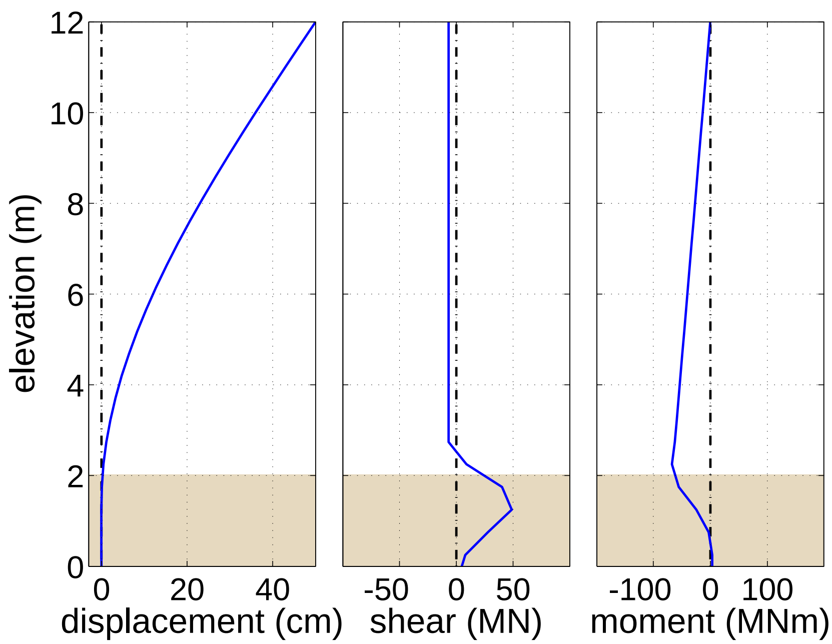

Figure 2.26 Shear and bending moment in shaft with rock layer only (Case d: freehead, fixed at bottom).

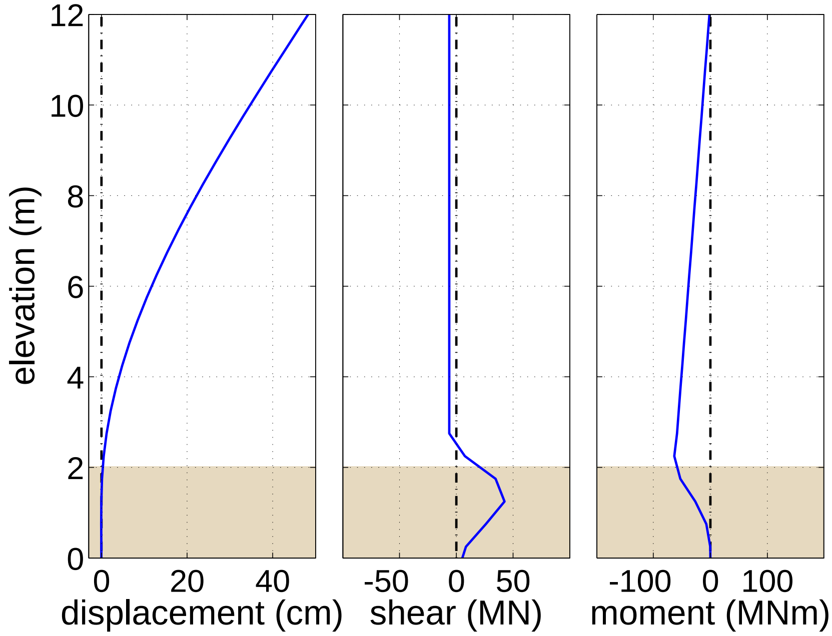

Figure 2.27 Shear and bending moment in shaft with rock layer only (Case e: freehead, considering friction: mu = 0.5, G = 1E3).

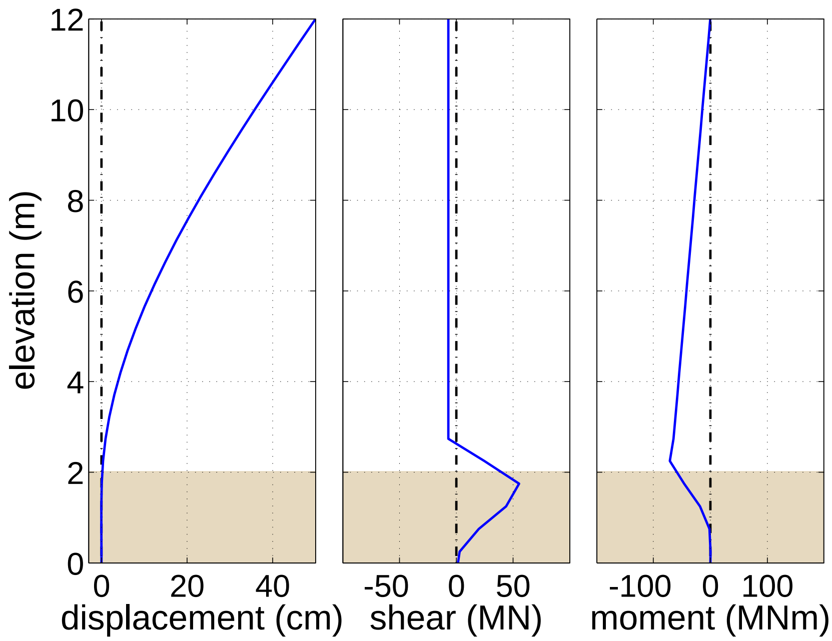

Figure 2.28 Shear and bending moment in shaft with rock layer only (Case f: freehead, considering friction: mu = 0.5, G = 1E6).

Figure 2.29 shows a mesh for a case where soil is included. For this purpose, solid elements and beam-to-solid contact elements were used to represent the soil. The results presented in Figure 2.30 show a decrease in shear demand due to the presence of the soil. These results are consistent with what was observed using p-y springs. Figure 2.31 shows results for a case where the diameter of the rock socket is slightly larger than the diameter of the shaft. Note that a slight difference in diameter results in toe rotation and a reduction in shear demand. Figure 2.32 shows results for a case where the shaft is modeled using a plastic-fiber section. Unlike the elastic section case, use of a plastic section can provide a modest amount of ductility while limiting the maximum reaction force by forming a plastic hinge; see Figure 2.33 where the plastic hinge is marked in red. The limit on the maximum moment of the shaft tends to limit the very high shear force at the rock–soil interface. Table 2.8 shows the maximum shear forces and shear stress ratios for these cases. In contrast to the case without soil, here the plastic hinge forms in a section of the pile closer to the surface.

Table 2.8 Shear force summary for 3D cases (shaft, rock, and soil).

	Shear Force at Top of Shaft (MN)	Maximum Shear Force (MN)	Shear Force Ratio
Case 1	9.39	37.58	4.00
Case 2	8.57	23.28	2.72
Case 3	2.79	4.91	1.76

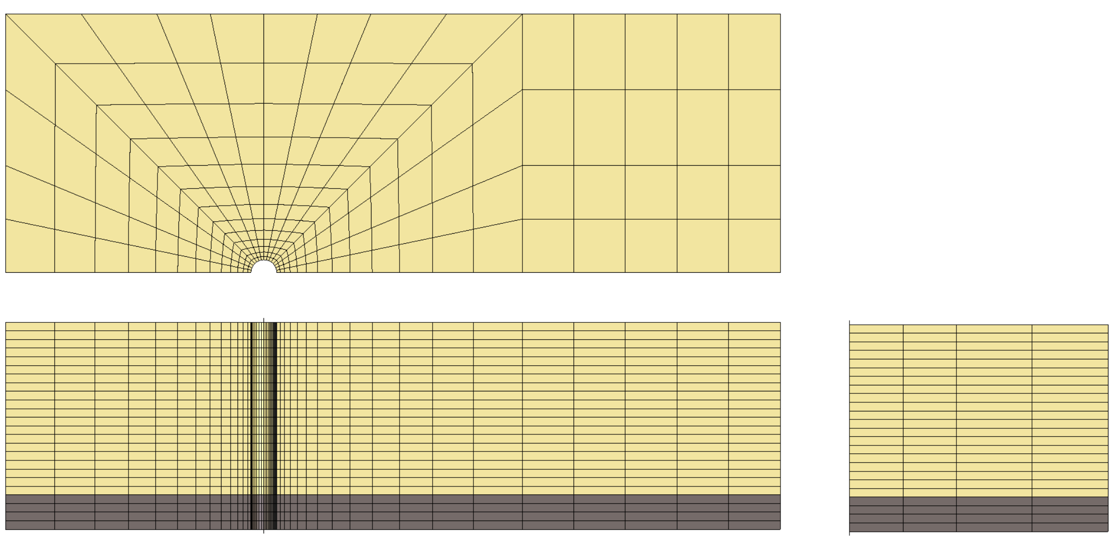

Figure 2.29 Overview of 3D FE mesh for a profile with 10 m of soil and 2 m of rock.

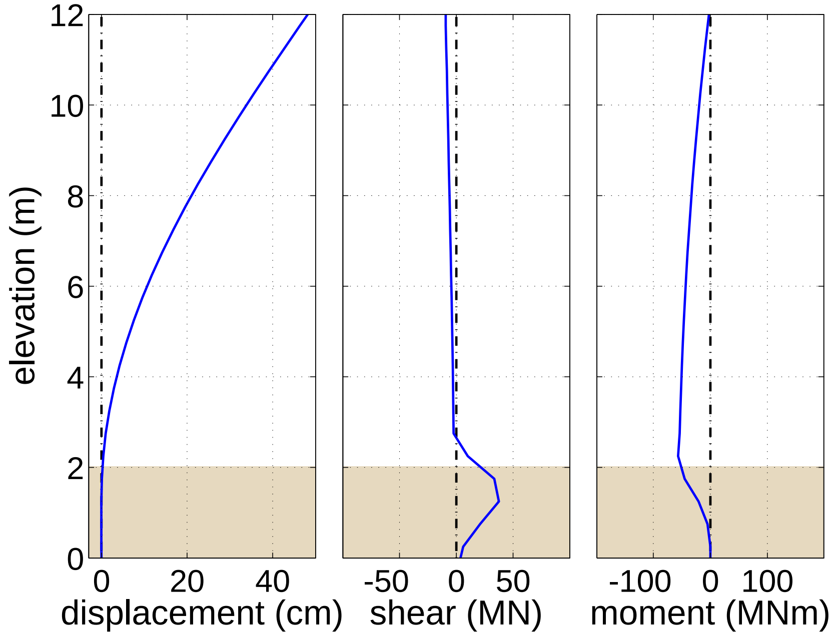

Figure 2.30 Shaft bending demands for site profile 1 with rock Class I (free head).

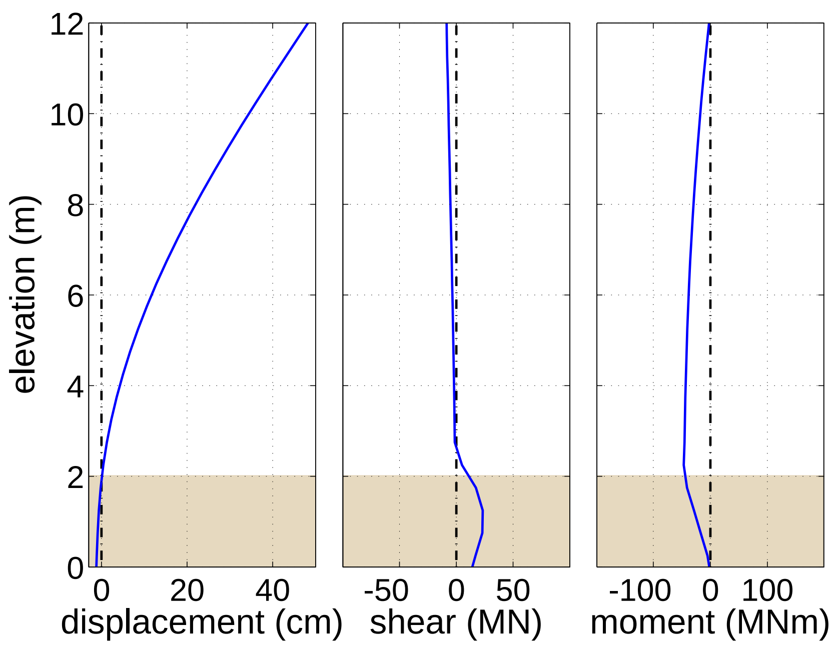

Figure 2.31 Shaft bending demands for site profile 1 with rock Class I (freehead, with 1-cm spacing between the shaft and rock layer).

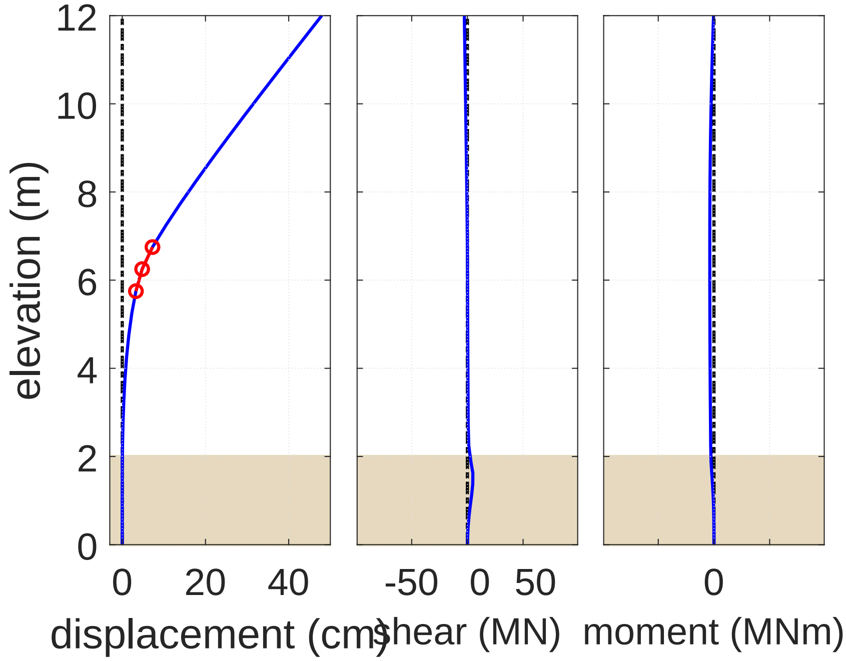

Figure 2.32 **Shaft bending demands for site profile 1 with rock Class I (freehead, using a plastic-fiber section to model the shaft).**

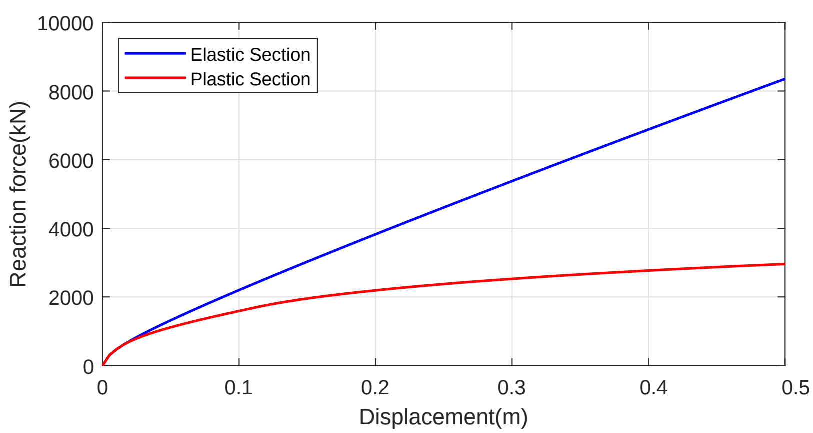

Figure 2.33 **Comparison of reaction force at top of the shaft between an elastic section and a plastic-fiber section.**

3D Analysis using Solid Elements to Represent the Shaft

As an alternative to beam elements, Figure 2.34 shows a model where both the shaft and the rock are represented using 3D brick elements, and the shaft–rock interface is represented using solid-to-solid contact elements. Although computationally more expensive, these models offer the possibility of evaluating aspects of the shaft behavior where beam theory may be insufficient; e.g., cases where plane sections do not remain plane or when a detailed response description of a particular cross section is of interest (e.g., at the bottom of the shaft).

In contrast to beam elements, this model representation does not provide direct information on shear and bending moment demands. These values must be calculated using the stress information recorded at the solid elements. To develop a shear diagram, the shaft must be subdivided into cross sections at different depths, and at each cross section the shear–stress field (τ_{xz} in this case) must be integrated over the shaft cross-sectional area. By evaluating the shear force at different locations, it is possible to recreate the shear-force diagram. In this study, fifteen sections were used along the shaft, concentrating them near the socketed portion of the shaft. Figure 2.35 shows the shear–stress contours (τ_{xz}) for one possible cross section. Figure 2.36 shows shear–stress contours at each of the fifteen locations along the shaft and the resulting shear diagram obtained by integration. Figure 2.37 shows the shear–stress diagram obtained using this method for a 0.5-m-horizontal displacement applied at the top of the shaft. The shear-force diagram is very similar to the one obtained using beam elements thus verifying its accuracy.

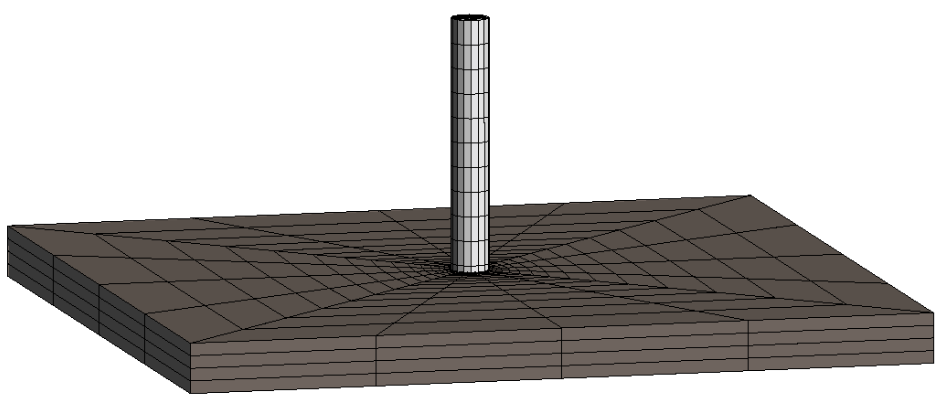

Figure 2.34 3D FEM model using solid elements for shaft and rock for 2-m rock profile.

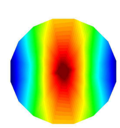

$$V_i = \int_A \tau dA$$

i

Figure 2.35 Calculation of shear force.

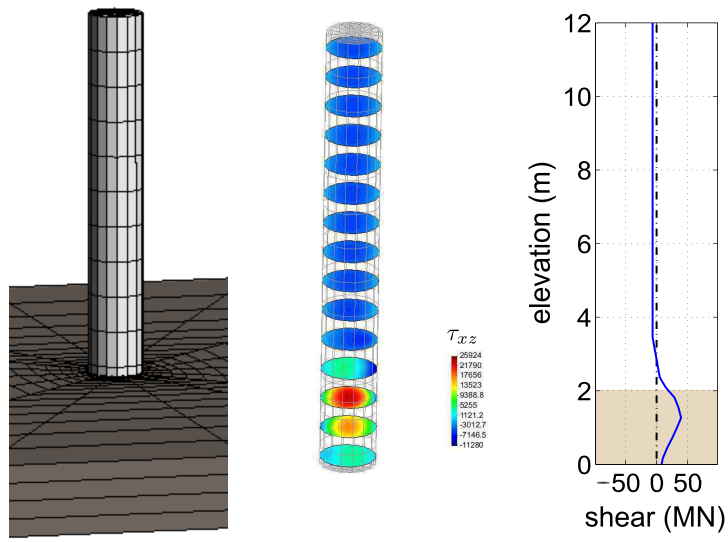

Figure 2.36 Shear–stress contours at different locations.

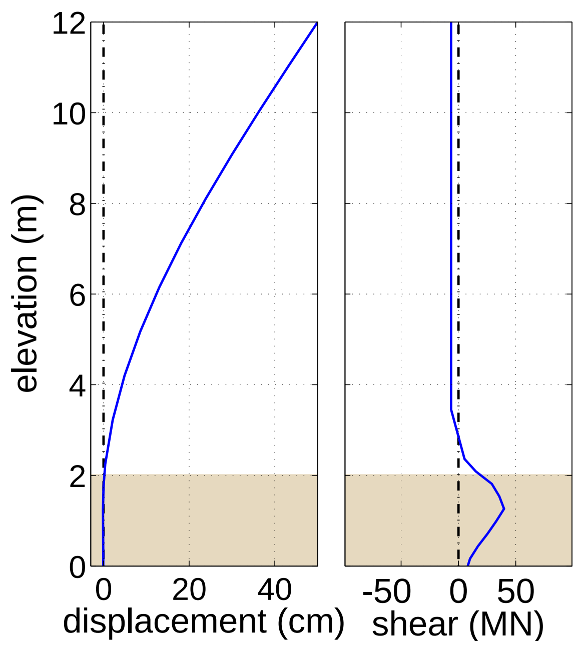

Figure 2.37 Shear demands of a shaft with rock layer only (freehead).

Figure 2.38 shows contours of contact forces at the rock–shaft interface. These forces, evaluated using contact elements, represent the forces required to prevent penetration of the shaft into the rock. The results shown in the figure correspond to a frictionless case. As the shaft deforms in the horizontal direction, it engages the rock socket, generating compressive forces at opposite points along the contact surface; these forces appear in red in the figure. Zero-force areas indicate the tendency to gap formation.

The resultant of these compressive forces (V) generate a resisting moment $M_R = V \times h_{eff}$ that opposes the demand bending moment $M_D = L \times H$. The value of V required to bring the system to equilibrium depends on the effective height h_{eff} that can be formed. Figure 2.39 shows contours of contact forces and estimated h_{eff} for different socket depths; in this case as the socket depth increases, h_{eff} increases, reaching a maximum depth equal to or larger than 2.0. At this point, a condition of *full* fixity is reached, and the shear demand remains the same.

Figure 2.40 shows shear-force diagrams for the same shaft and loading condition analyzed in the previous sections but considering different types of rock (ranging from Type I to Type V - see Table 2.9 for rock material properties). The results show that shear demands decrease as the rock quality decreases. Table 2.10 shows maximum shear forces and shear-force ratios for each case. The weaker the rock, the smaller the shear demand and the larger the shaft rotation. Results for cases with friction and without friction are also shown in the figure, indicating that the effect of friction is negligible for this example. These results are consistent with results obtained using p-y springs; i.e., the p-y spring results are higher than those obtained using 3D FEM models. This is addressed in more detail in Chapter 3. Although counter intuitive, a weaker socket seems to be beneficial in terms of shear demands

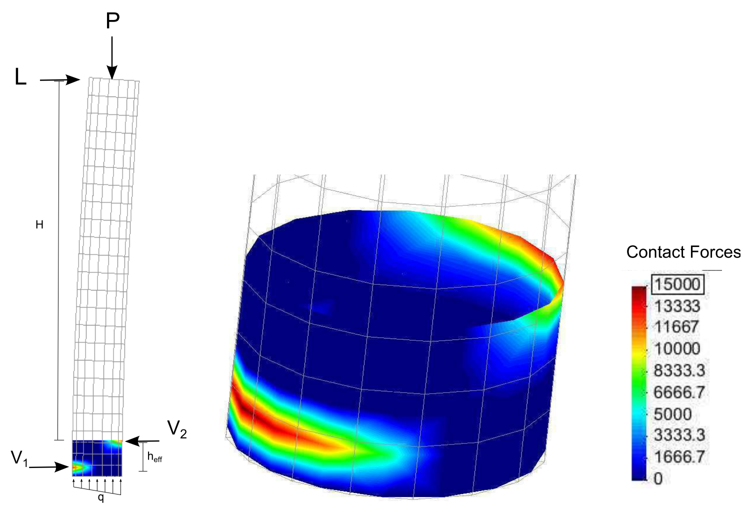

Figure 2.38 Contact force around the bottom of the shaft.

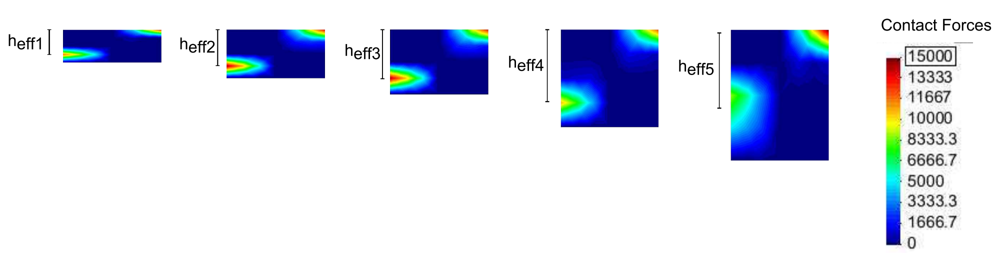

Figure 2.39 h_{eff} doesn't increase when embedment is larger than 1.5 m.

Table 2.9 Drucker-Prager properties assumed for materials in numerical models.

	Rock Types					
	I	II	III	IV	V	Soil
K(MPa)	67000	21300	6700	2130	670	220
G(MPa)	40000	12800	4000	1280	400	95
$\sigma_Y(KPa)$	12720	12720	12720	12720	12720	100
ρ	0.716	0.696	0.665	0.515	0.296	0.362

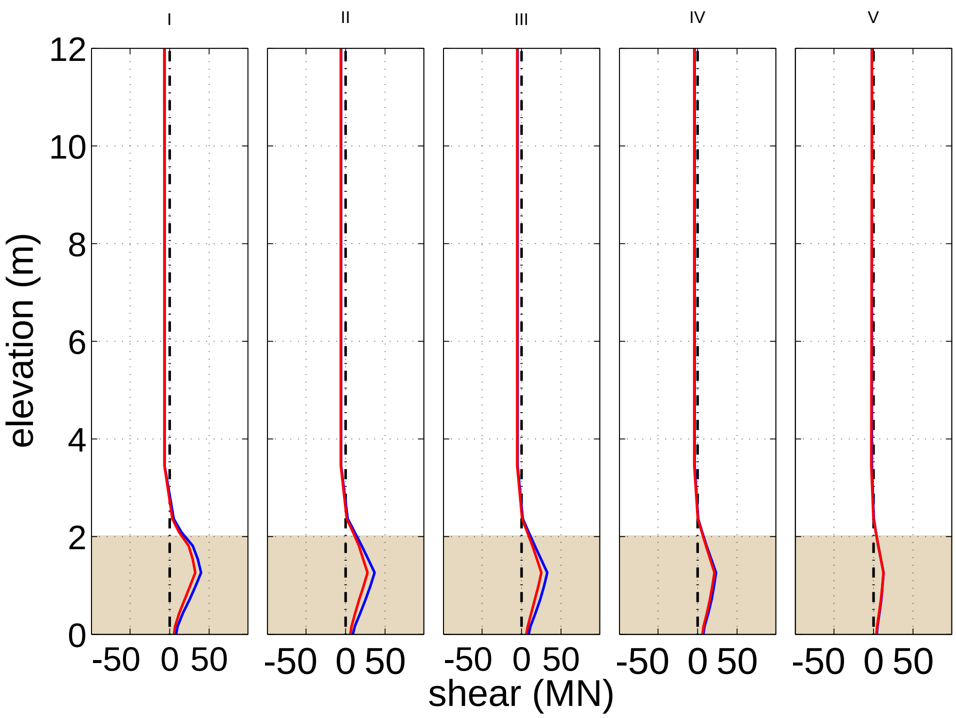

Figure 2.40 Shear demands in shaft with different rock types (freehead blue lines show the cases without friction between shaft and rock, while red lines show the cases considering friction with $\mu = 0.5$).

Table 2.10 Shear force summary for different rock types.

Rock Type	Friction Condition	Shear Force at Top of Shaft (MN)	Maximum Shear Force (MN)	Shear Force Ratio
I	No friction	6.33	39.85	6.30
	$\mu = 0.5$	6.63	32.49	4.90
II	No friction	5.62	36.88	6.56
	$\mu = 0.5$	6.08	27.80	4.57
III	No friction	5.00	32.65	6.54
	$\mu = 0.5$	5.64	25.13	4.45
IV	No friction	3.66	23.43	6.40
	$\mu = 0.5$	4.27	21.48	4.03
V	No friction	2.06	12.75	6.19
	$\mu = 0.5$	2.14	12.69	5.93

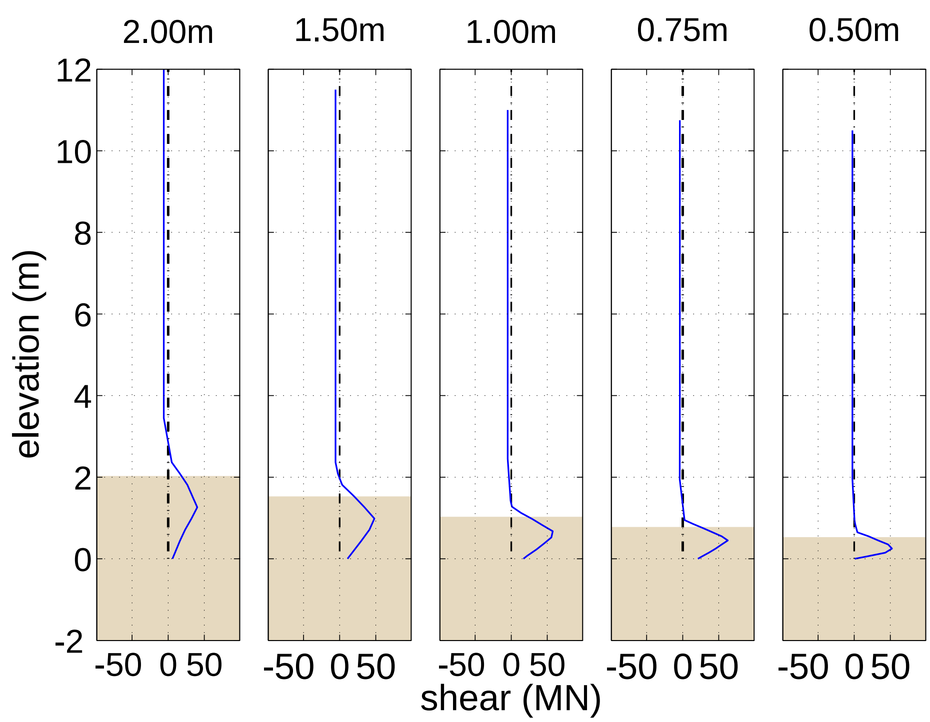

Figure 2.41 Shear demands in shaft with different socket depths.

Figure 2.41 shows results for cases with different rock-socket depths (ranging from 2.0 m to 0.5 m). All cases include a 6.0-m-thick rock layer below the shaft toe; all rock sockets have the same material properties. The results show that as the socket depth decreases, the shear demand increases. This is due to the change in effective height, h_{eff}, that decreases as the shaft socket depth decreases (requiring larger shear forces to generate enough resisting moment to equilibrate the system). This tendency changes when uplift occurs. This is clear in the 0.5-m case where the shear demand is smaller than that for a 0.75-m case. The presence of the layer of rock below the shaft toe and corresponding toe contact surface are very important in the observed response since the rock stiffness and strength and ability to uplift control the amount of rotation at the toe influences the amount of shear required to equilibrate the system, i.e., larger rotations means less shear demand. An advanced model that accounts for the rock stiffness and strength at the shaft toe is presented in Chapter 4. In general, the results obtained using 3D FEM models imply shear demands that are smaller than those obtained using p-y springs. Although the differences are not large, they are noticeable. These discrepancies may be due to: (a) geometric and material modeling differences between p-y and 3D FEM models; (b) the effect of friction along the socket shaft; and/or (c) limitations of beam formulations (used in p-y models and beam-solid models).

In terms of geometric and material modeling differences, this study relied on findings from the recent work by McGann et al. (2012), which shows that it is possible to reproduce drilled-shaft load-deformation experimental curves and p-y curves using 3D-FEM models together with advanced constitutive models (e.g., 3D Drucker-Prager model) as long as representative elasto-plastic properties are used (i.e., shear and bulk modulus, cohesion, friction angle, and hardening parameters). This study followed McGann's recommendations to define the constitutive model material properties to represent the rock and soil. In terms of frictional resistance, all simulations indicate that the friction along the socket interface has a small effect on shear demands.

In an effort to explore this issue, this study considered several cases with different levels of frictional resistance along the shaft. Figure 2.43 shows shear stresses (τ_{xz}) in the direction of loading at three locations (labeled I, II, and III) for three frictional cases (i.e., $\mu = 0$, $\mu = 0.5$, and $\mu = 1.0$, with $\mu = tan(\phi_i)$, with ϕ_i = interface friction). The results show that the shear–stress distribution moves down (i.e., less shear demand) as the frictional resistance increases; however, this effect seems to be small in the overall shear force demand force unless the frictional resistance is very high (unrealistic). Finally, most beam formulations build of the assumption that plane sections remain plane. This may not be true for large cross sections confined in competent material and subjected to large lateral and axial loads. Therefore, in an effort to investigate this issue, Figure 2.43 shows the distribution of vertical displacements at two cross sections (labeled II and III in the figure) for two friction coefficients (i.e., $\mu = 0$, $\mu = 0.5$). The results clearly indicate that plane sections do not remain plane. This effect is more noticeable as friction increases and for the section more embedded in the rock socket (i.e., section III). The *warping* observed in sections II and III contribute to reducing the shear force generated in the rock socket. All these effects contribute to reduce shear demands obtained using 3D FEM simulations compared to those obtained using p-y springs validating the conclusions presented herein. Nevertheless, it appears these effects are smaller and statistically less important compared to the effect of uncertainties in rock properties and construction deviations in shear demands. These results together with the analysis presented in Chapters 3 and 4 encourage the use of p-y springs with proper definitions for the properties of the rock p-y, and proper consideration of the conditions at the shaft toe.

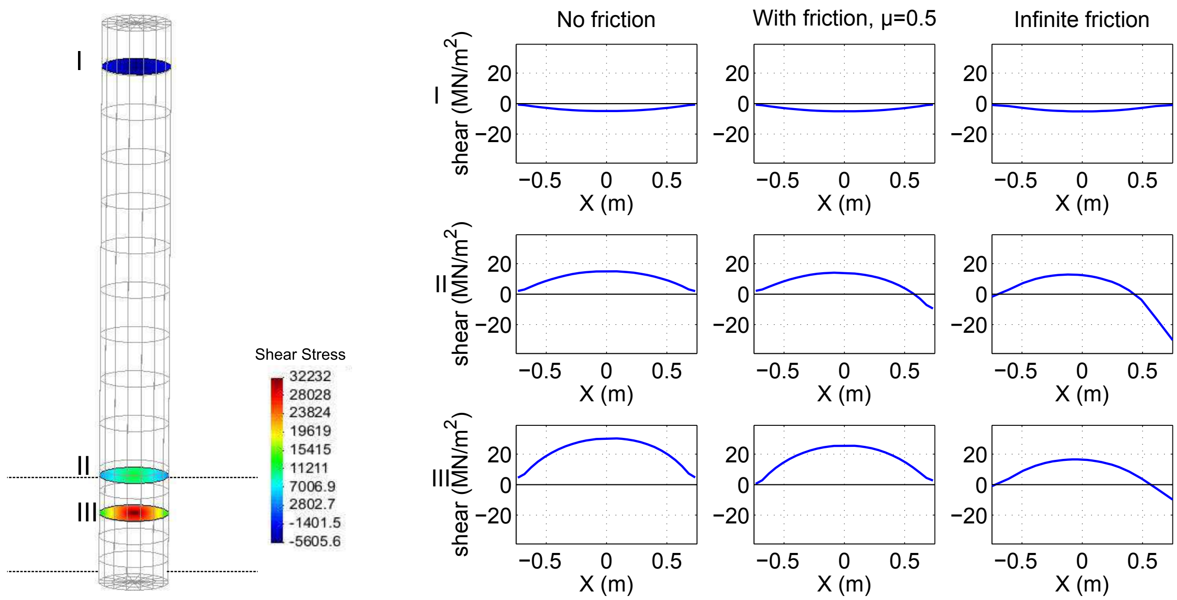

Figure 2.42 Shear–stress distributions at different locations.

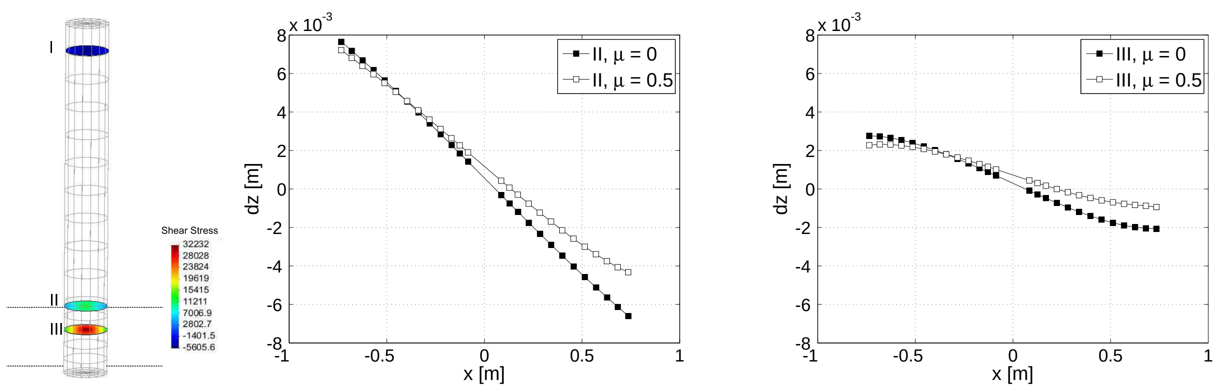

Figure 2.43 Displacements within shaft cross section showing that the plane surface does not remain plane.

Finally, the results presented so far assume that shear is the only resisting mechanism that can be generated and demonstrate that large shear demands must develop in the rock socket to resist the demanding bending moment. They also show that these shear forces may decrease if friction is considered around the socket interface or the shaft toe is allowed to rotate (e.g., in the case of a short socket or weak rock). Given these factors, an improved resisting mechanism is possible by including the contribution of the axial load P to the resisting bending moment. More precisely, as a result of the applied lateral load, the normal stress distribution at the shaft toe is not uniform, resulting in an eccentric normal load P. This is schematically shown in Figures 2.44(a) and (b). The eccentric load causes a supplemental resisting moment that reduces the required shear force that is needed to equilibrate the system.

In principle, the larger the normal load and eccentricity, the larger the resisting moment and the smaller the needed shear force. Obviously, the non-uniformity in load distribution at the shaft toe depends on many factors, including axial load magnitude, shaft diameter, socket depth, and rock properties. In an effort to evaluate this effect, the same drilled shaft example used in the previous sections was reanalyzed considering different axial loads and rock-socket depths. The axial loads range from no load ($P = 0\ MN$) to a relatively large value ($P = 56.55\ MN$) to represent the weight of a large superstructure. Two additional values were considered: ($P = 14.14\ MN$) and ($P = 28.27 MN$)). The rock-socket depths ranged from 0.5 m to 2.0 m. Figure 2.45 shows shear-force diagrams for all cases, and Table 2.11 shows the corresponding values for the shear force at the top of the shaft, maximum shear force, and shear–stress ratio. As expected, the results show that the shear demands decrease as the axial load and rock socket depth increase. Figures 2.46(a) and (b) provide additional insight on the relative importance of axial load and rock-socket depth on the reduction of shear demand. Figure 2.46(a) shows the maximum shear–stress ratios as a function of socket depth (for all axial loads), and Figure 2.46(b) shows the same information as a function of axial load (for all rock-socket depths). The results are consistent with the results presented above and reinforce the possible benefits of a model that includes this resisting mechanism.

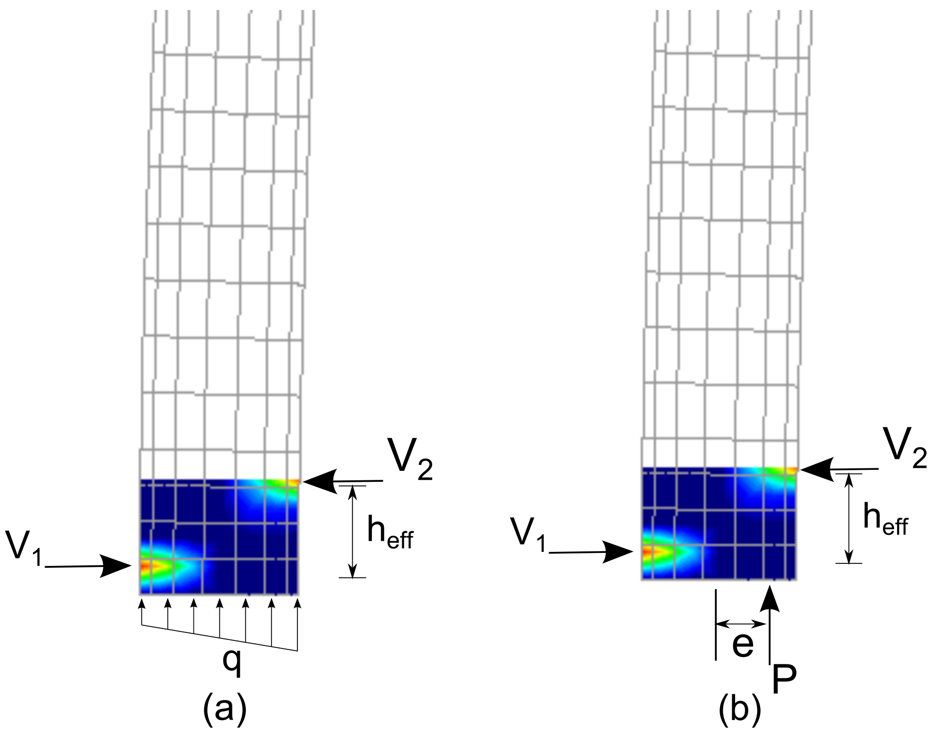

Figure 2.44 Effect of axial load on resisting bending moment

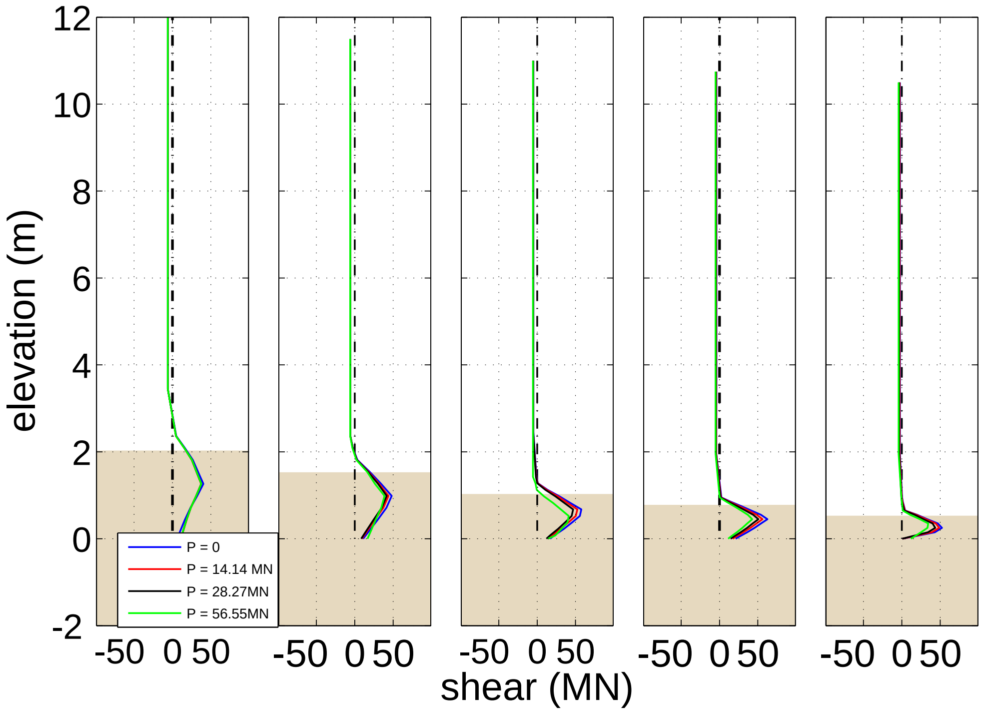

Figure 2.45 Shear demands in shaft with different axial loads.

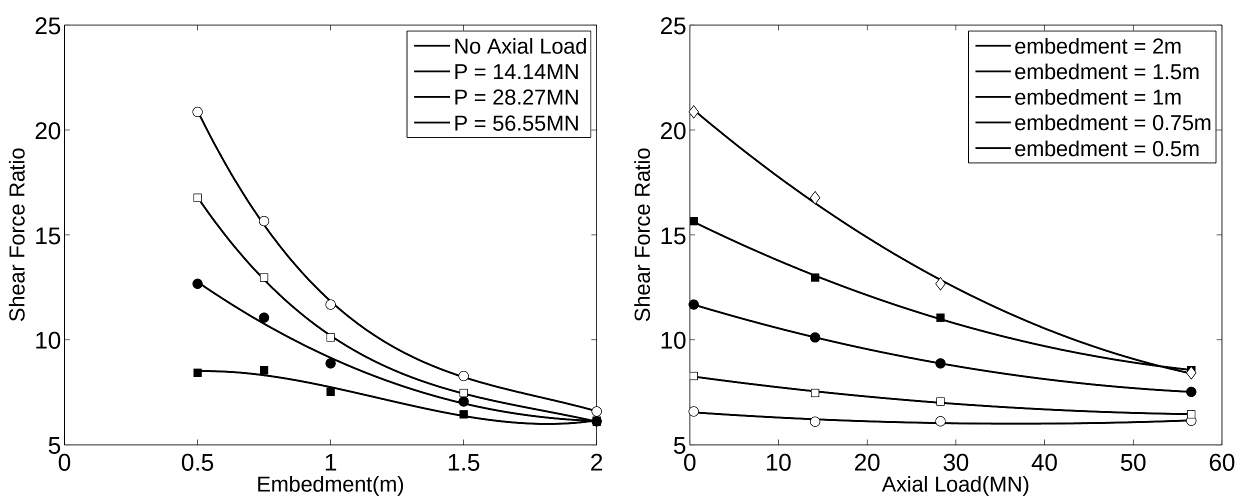

Figure 2.46 Influence of axial load and embedment on shear force ratio.

Table 2.11 Shear force summary for different axial loads.

Embedment	Axial Load (MN)	Shear Force at Top of Shaft (MN)	Maximum Shear Force(MN)	Shear Force Ratio
2.0m	P = 0	6.10	40.26	6.59
	P = 14.14 MN	6.14	37.46	6.10
	P = 28.27 MN	6.14	37.55	6.12
	P = 56.55 MN	6.14	37.75	6.15
1.5m	P = 0	5.81	48.08	8.28
	P = 14.14 MN	5.87	43.86	7.47
	P = 28.27 MN	5.90	42.18	7.06
	P = 56.55 MN	5.99	38.68	6.45
1.0m	P = 0	4.94	57.66	11.68
	P = 14.14 MN	5.19	52.50	10.12
	P = 28.27 MN	5.29	47.01	8.88
	P = 56.55 MN	5.48	41.23	7.52
0.75m	P = 0	4.00	62.66	15.66
	P = 14.14 MN	4.33	56.15	12.97
	P = 28.27 MN	4.59	50.75	11.05
	P = 56.55 MN	5.00	42.78	8.56
0.5m	P = 0	2.51	52.32	20.86
	P = 14.14 MN	2.90	48.71	16.77
	P = 28.27 MN	3.43	43.46	12.67
	P = 56.55 MN	4.27	34.39	8.43

2.7 SUMMARY

The analysis presented in the previous sections show that:

1. Although p-y based models predict larger shear demands, they are extremely simple to use.
2. The proper definition of p-y curves for rocks results in reasonable shear demands.
3. A comparison between results from p-y based models and 3D FEM models shows that 3D FEM models result in less shear force and bending moment demands in the shaft.
4. Beam elements properly capture shear demands.
5. Solid elements representing the shaft produce accurate shear demands. Although friction along the socket shaft tends to reduce shear demands, the problems examined in this study show that the effect is minimal. Plane sections do not remain plane (i.e., the results of the beam effect), but the results presented herein show that this effect is minimal.
6. Modeling the shaft using a plastic-fiber section may cause the shaft to yield after modest ductility. This limits the extension of shaft deflection and reduces shear demands at the soil–rock interface; reduction is dependent on the section properties chosen.
7. Rotation at the base of the shaft has an important effect on shear demand.
8. Eccentricity in axial loads provides a resisting bending moment that helps reduce shear demands. This effect is more significant as the axial load increases and h_{eff} decreases. It may also be beneficial for small socket depths where shaft rotation may increase.

3 Parametric Study using BNWF p-y Models and Comparison with 3D FEM Simulations

3.1 INTRODUCTION

Chapter 2 proposed different modeling strategies to address the problem of rock-socketed shafts subjected to lateral loads. The models range from simple beams to advanced 3D FEM models. The merits and limitations of each modeling strategy were analyzed using a base-case geometry and soil–rock properties. The models differ in the way they characterize the structure (drilled shaft) and the rock–soil interaction effect. The models include cases where the shaft is represented by either beam elements or solid (brick) elements and models where the interaction effect is captured using either p-y springs or solid elements (together with advanced contact elements). The results indicate lower shear demands when using 3D solid elements to represent the shaft and soil/rock than when using beam elements and p-y springs; however, the differences are modest and can be considered small when compared to aleatoric uncertainties in soil and rock properties and epistemic uncertainties in the modeling strategy. In this context, it appears that when properly selected, p-y springs are a good choice and beam elements a natural choice to represent the structural member, particularly from a computational point of view. To expand on this notion, and in an attempt to evaluate recent p-y springs for rocks, this chapter presents results from a parametric study considering a wide range of rock properties and rock-socket depths. The study includes different criteria to define the soil and rock p-y curves [i.e., Reese (1997) vs. Liang (2009)], different beam theories (i.e., Euler-Bernouli vs. Timoshenko), different interface frictional resistances, and comparisons with 3D FEM simulations. For completeness, a brief description of recent p-y criteria for rocks is presented in the next section.

3.2 DEFINITION OF P-Y CURVES FOR ROCK

3.2.1 Reese (1997)

The interim p-y curve criteria for rocks proposed by Reese (1997) are defined in terms of the shaft diameter, B, and three engineering properties of the rock mass: the uniaxial compressive strength of the intact rock, q_u, the initial rock mass elastic modulus, E_{ir}, and the rock quality index (RQD). The curves are defined in terms of three primary equations:

1. An initial linear portion for $y \leq y_A$,

$$p(y) = K_{ir} y \tag{3.1}$$

with $K_{ir} = k_{ir} E_{ir}$ where k_{ir} is a dimensionless constant given by

$$k_{ir} = \begin{cases} \left(100 + \dfrac{400 z_r}{3B}\right) & \text{for } 0 \leq z_r \leq 3B \\ 500 & \text{for } z_r > 3B \end{cases} \tag{3.2}$$

where z_r is the depth below the surface of the rock mass.

2. A nonlinear transitional portion for $y \geq y_A$ and $p \leq p_{ur}$,

$$p(y) = \frac{p_{ur}}{2} \left(\frac{y}{y_{rm}}\right)^{0.25} \tag{3.3}$$

where $y_{rm} = k_{rm} B$, with k_{rm} as a constant in the range $0.00005 \leq k_{rm} \leq 0.0005$, and p_{ur} is the rock mass ultimate resistance defined as

$$p_{ur} = \begin{cases} \alpha_r q_u B \left(1 + 1.4 \dfrac{z_r}{B}\right) & \text{for } 0 \leq z_r \leq 3B \\ 5.2 \alpha_r q_u B & \text{for } z_r > 3B \end{cases} \tag{3.4}$$

where $\alpha_r = 1.0 - 2/3 \cdot \text{RQD}$ is a strength reduction factor ($0 \leq \text{RQD} \leq 1$).

3. A limiting zero-slope portion for $p > p_{ur}$ where

$$p(y) = p_{ur} \tag{3.5}$$

The displacement, y_A, which is the transition between the linear and nonlinear portions of the curve, is obtained by the intersection of (3.1) and (3.3) and has the form

$$y_A = \left(\frac{p_{ur}}{2 K_{ir} y_{rm}^{0.25}}\right)^{1.333} \tag{3.6}$$

The Reese (1997) curves are included in the commercial software LPILE™ (2010), which according to Turner (2006) is the program most frequently used by state transportation agencies for the analysis of laterally-loaded rock-socketed shafts. Reese (1997) also proposed bi-linear curves for use with strong rock. These curves are included in LPILE™; however, their scope is limited and non-applicable in many practical scenarios. Due to the limitations of the strong-rock curves, Turner (2006) reports that some practitioners apply the weak-rock criteria for all cases. This approach is adopted here to be consistent with the state-of-practice.

3.2.2 Liang et al. (2009)

The rock p-y curves of Reese (1997) are a commonly used method for representing rock materials in a BNWF analysis; however, these curves are based on a limited number of field studies. More recent work (Gabr et al., 2002; Liang et al., 2009) has been conducted with the goal of improving the definition of p-y curves for weathered rock. Both of these studies present rock p-y curves with a hyperbolic function

$$p(y) = \frac{y}{\dfrac{1}{K_h} + \dfrac{y}{p_u}} \tag{3.7}$$

but differ somewhat in their recommended techniques for defining the initial tangent and ultimate resistance of the curves.

The ultimate lateral resistance for the Liang et al. (2009) curves is taken as the lesser of two values. The first value is computed based on a failure-wedge analysis of the rock mass, which generally governs the response near the surface of the rock mass. The ultimate resistance based on this wedge model is computed as

$$p_u = 2C_1 \cos\theta \sin\beta + C_2 \cos\beta + C_3 \sin\beta - 2C_4 \sin\theta - C_5 \tag{3.8}$$

where

$$C_1 = H \tan\beta \sec\theta \left(c' + K_0 \sigma'_{v0} \tan\phi' + 0.5 H K_0 \gamma' \tan\phi'\right) \tag{3.9}$$

$$C_2 = \frac{D \tan\beta(\sigma'_{v0} + H\gamma') + H \tan^2\beta \tan\theta(2\sigma'_{v0} + H\gamma') + c'(D + 2J \tan\beta \tan\theta) + 2C_1 \cos\beta \cos\theta}{\sin\beta - \tan\phi' \cos\beta} \tag{3.10}$$

$$C_3 = C_2 \tan\phi' + c'(D \sec\beta + 2H \tan\beta \sec\beta \tan\theta) \tag{3.11}$$

$$C_4 = K_0 H \tan\beta \sec\theta(\sigma'_{v0} + 0.5\gamma' H) \tag{3.12}$$

$$C_5 = \gamma' K_a (H - z_0) D \tag{3.13}$$

with H as the depth into the rock mass, σ'_{v0} as the vertical effective stress at the top of the rock mass, γ' as the effective unit weight of the rock mass, ϕ' as the effective friction angle of the rock mass, c' as the effective cohesion of the rock mass, and D as the shaft diameter; thus

$$K_a = \tan^2(\pi/4 - \phi'/2) \tag{3.14}$$

$$K_0 = 1 - \sin\phi' \tag{3.15}$$

$$z_0 = \frac{2c'}{\gamma' \sqrt{K_a}} - \frac{\sigma'_{v0}}{\gamma'} \tag{3.16}$$

$$\beta = \pi/4 + \phi'/2 \tag{3.17}$$

$$\theta = \phi'/2 \tag{3.18}$$

In computation of these terms, if $C_5 < 0$, it is set at zero in Equaton (3.8).

The second ultimate resistance value is based on the assumptions that the wedge-type failure will not occur at greater depths within the rock mass, and that the initial failure mode for the rock at these depths will be tensile in nature. The ultimate resistance at great depth is computed as

$$p_u = \left(\frac{\pi}{4} p_L + \frac{2}{3} \tau_{\text{max}} - p_a \right) D \tag{3.19}$$

where p_L is the compressive strength of the rock mass, τ_{max} is the maximum horizontal side shear resistance, and $p_a \geq 0$ is the active horizontal earth pressure given by

$$p_a = K_a \sigma'_v - 2c' \sqrt{K_a} \tag{3.20}$$

with σ'_v as the vertical effective stress at the depth under consideration.

3.3 INITIAL ASSESSMENT OF THE PROBLEM

Analogous to what was done in Chapter 2, a beam using a nonlinear BNWF model of a single rock-socketed shaft subjected to lateral loading has been developed and analyzed in this section. The model is similar to previous examples and considers four 12-m-deep site profiles, each with a homogeneous layer of cohesionless soil with unit weight $\gamma = 17$ kN/m^3 and friction angle $\phi = 33°$ above a layer of rock. The configurations of the sites vary only with respect to the thickness of the soil and rock layers; the shaft is embedded through the entire 12-m profile in all cases. Four site profiles are considered:

- 10 m of soil with 2 m of rock
- 8 m of soil with 4 m of rock
- 6 m of soil with 6 m of rock
- 4 m of soil with 8 m of rock

The soil and rock materials are incorporated into the BNWF model using p-y curves. The weak rock curves of Reese (1997) are used for the rock portion of the profile, with ultimate resistance and stiffness values computed for the five considered rock classifications in Table 2.1. Two techniques were used to define the p-y curves for the cohesionless soil:

- Curves based on the API (2007) recommended values for ultimate lateral resistance and initial stiffness
- Curves based on the Brinch Hansen (1961) definition for ultimate lateral resistance and the API initial stiffness value modified for overburden stress after Boulanger et al. (2003)

As before, a 12-m-long, 1.5-m-diameter drilled shaft was embedded in the model soil profile. Linear elastic behavior was assumed for the shaft. The model parameters for this shaft are the gross section area, $A = 1.767$ m^2, the gross second area moment, $I = 0.249$ m^4, an elastic modulus, $E = 21.3$ GPa, and a shear modulus of $G = 8.52$ GPa. These parameters are based on a template nonlinear shaft cross section; however, linear elastic response has been assumed in order to assess strength-independent demands. Two boundary conditions were considered at the top of the shaft: (a) a fixed-rotation condition emulating the presence of a shaft cap or other superstructure; and (b) A free-rotation condition that assumes no influence from superstructure elements.

An axial load $P = 4120$ kN was applied to the shaft to simulate structural loads applied by superstructure elements. Lateral loads were applied to the shaft–soil system by gradually imposing a 0.5-m displacement to the top of the shaft. Figures 3.1 through 3.8 show the shaft displacement, shear force, and bending moment demands for the considered BNWF pushover analyses. As shown, there are only minor differences between the results for the two sets of cohesionless soil p-y curves, with the most significant differences occurring for the weakest (Class V) rock designation. For all cases, as the quality of the rock increases, the contrast between the upper and lower layer shear force demands also increases. The shaft head boundary condition changes the magnitude of the shear force and bending moment demands in the shaft, with the free-head condition inducing lower demands for an equal amount of lateral head displacement.

The contrast between the maximum shear force demands in the two layers is evaluated as a ratio of the maximum shear force in the rock layer to the maximum shear force above the rock layer. The shear force ratios for each of the considered BNWF analyses are shown in Table 3.1, which demonstrates that the shear force contrast between the two layers is much greater for the free-rotation boundary condition. The contrasts for the modified soil p-y curve parameters are generally greater than or equal to the corresponding API soil p-y curve cases, although the differences are only significant for the free-head cases.

The results of Table 3.1 and Figures 3.1 through 3.8 generally show that as the thickness of the rock layer is increased in comparison to the thickness of the soil layer, the ratio of the maximum shear force demands in each layer tends to decrease. This can be attributed to the increased force required at the shaft head in order to produce 0.5 m of lateral displacement as the rock becomes closer to the ground surface and begins to control the response of the soil–rock system.

The difference between the shear force ratios for the two sets of soil p-y curves reflects the differences in the soil strength and stiffness portrayed by each approach. The modified set of parameters specifies lower ultimate resistance and initial stiffness values for a given depth; therefore, there is a larger contrast between the soil and rock strength and stiffness for these cases. Despite the observed differences, the choice of soil p-y curves does not appear to significantly alter the magnification of shear force observed in the rock layer for a given case. The differences in the shear force ratios for the two shaft head boundary conditions demonstrate that the shaft kinematics significantly alter the effects of the rock layer on the system, providing further evidence of the importance of shaft kinematics in defining the demands in the soil–foundation system during lateral loading (see McGann et al., 2011).

A comparison of Tables 3.1 and 3.2 shows that while the trends noted in the previous section with respect to the shaft kinematics are present in the Liang et al. curve results, the shear force ratios are much lower. Though the shear force magnification effect is lessened when using the Liang et al. (2009) rock p-y curves, it does not completely vanish for the stronger rock classifications. It also appears from the results of Figures 3.9 through 3.12 that the Liang et al. (2009) approach may be underpredicting the strength and stiffness of the weakest rock classifications as the shaft essentially rotates rigidly in these cases; however, further analysis is required with alternative shaft designs in order to determine if this is a flaw in the p-y curves or a valid result for the ratio of shaft bending stiffness to rock strength in these cases.

Table 3.1 Shear force ratios for BNWF analyses with Reese (1997) rock p-y curves.

Site Profile	Soil p-y Curves	Shaft Head Condition	Rock Class I	II	III	IV	V
1	API	fixed	3.26	3.12	2.77	2.38	0.73
		free	5.63	5.58	5.06	3.93	2.16
	Modified	fixed	3.31	3.33	2.91	2.51	0.77
		free	6.42	6.33	5.64	4.45	2.40
2	API	fixed	3.04	2.94	2.53	2.19	1.24
		free	6.60	6.32	5.42	4.72	2.80
	Modified	fixed	3.09	3.00	2.58	2.25	1.30
		free	6.87	6.58	5.71	4.95	3.01
3	API	fixed	2.18	2.13	1.90	1.71	1.35
		free	5.28	5.11	4.35	4.04	2.79
	Modified	fixed	2.20	2.14	1.91	1.72	1.21
		free	5.36	5.19	4.44	4.13	2.89
4	API	fixed	1.38	1.33	1.24	1.18	0.98
		free	3.29	3.28	2.93	2.82	2.23
	Modified	fixed	1.38	1.34	1.25	1.18	0.95
		free	3.31	3.30	2.95	2.84	2.27

Table 3.2 Shear force ratios for BNWF analyses with Liang et al. (2009) rock p-y curves.

Site Profile	Soil p-y Curves	Shaft Head Condition	Rock Class I	II	III	IV	V
1	API	fixed	2.36	1.76	0.81	0.42	0.17
		free	3.60	2.96	2.29	1.59	1.22
	Modified	fixed	2.51	1.86	0.87	0.42	0.16
		free	4.01	3.47	2.55	1.74	1.24
2	API	fixed	1.96	1.50	1.06	0.66	0.22
		free	4.00	3.10	2.43	2.07	1.29
	Modified	fixed	2.00	1.53	1.10	0.70	0.22
		free	4.23	3.30	2.59	2.28	1.44
3	API	fixed	1.51	1.10	0.91	0.70	0.28
		free	3.69	2.76	2.18	1.98	1.48
	Modified	fixed	1.52	1.12	0.93	0.72	0.29
		free	3.76	2.83	2.26	2.10	1.64
4	API	fixed	0.94	0.74	0.64	0.60	0.29
		free	2.51	2.02	1.69	1.58	1.48
	Modified	fixed	0.94	0.75	0.65	0.61	0.30
		free	2.53	2.04	1.72	1.62	1.57

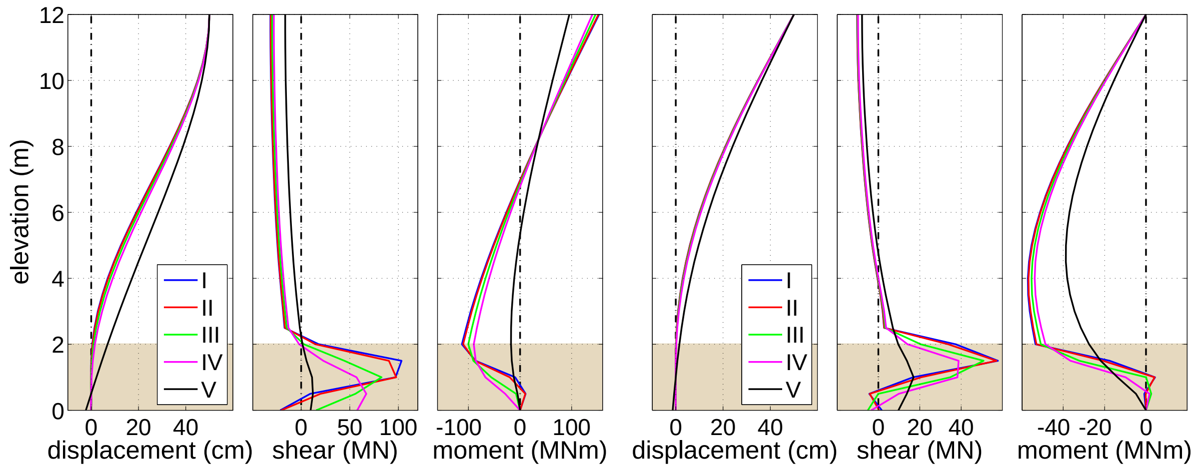

Figure 3.1 Shaft bending demands for site profile 1 using API soil p-y curves with Reese rock curves for five rock classifications (I-V).

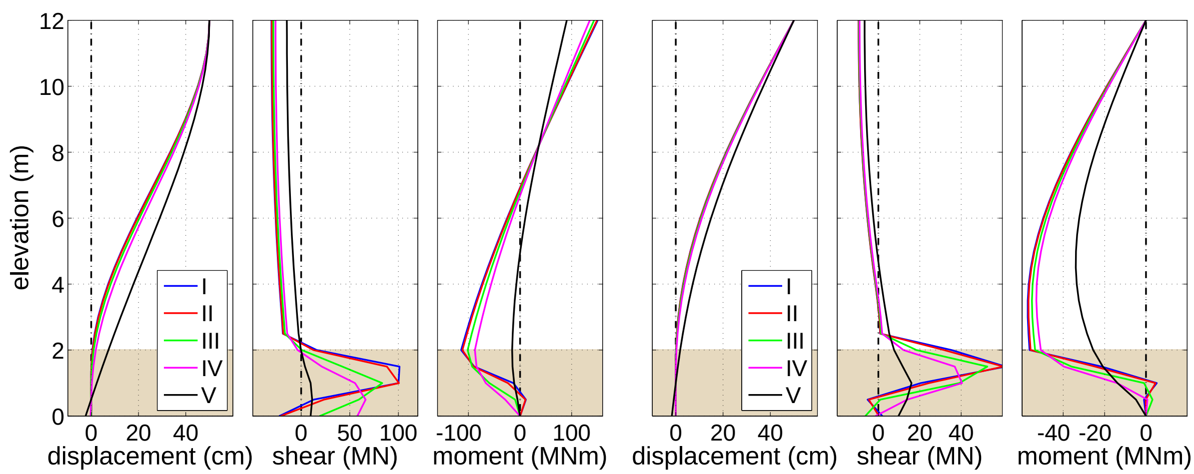

Figure 3.2 Shaft bending demands for site profile 1 using modified soil p-y curves with Reese rock curves for five rock classifications (I-V).

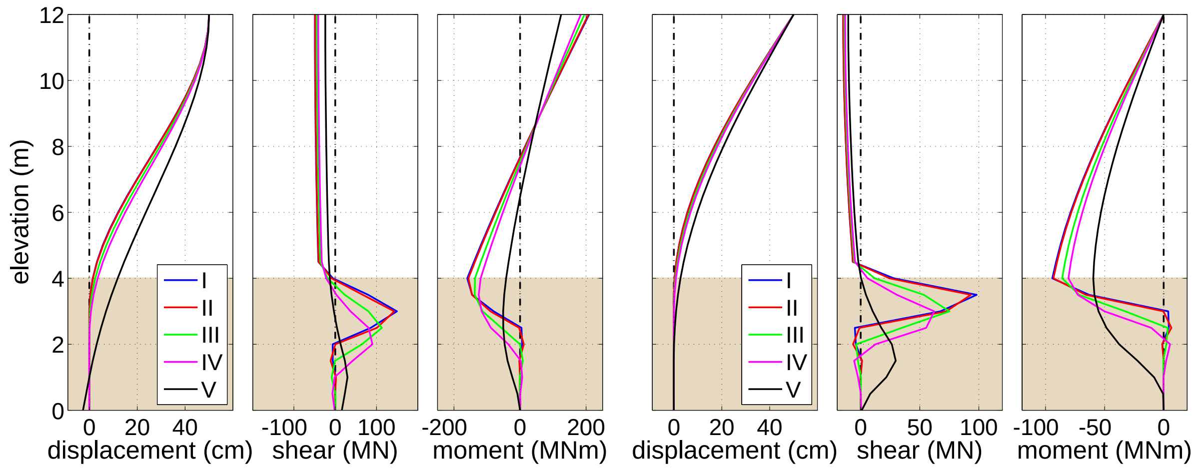

Figure 3.3 Shaft bending demands for site profile 2 using API soil p-y curves with Reese rock curves for five rock classifications (I-V).

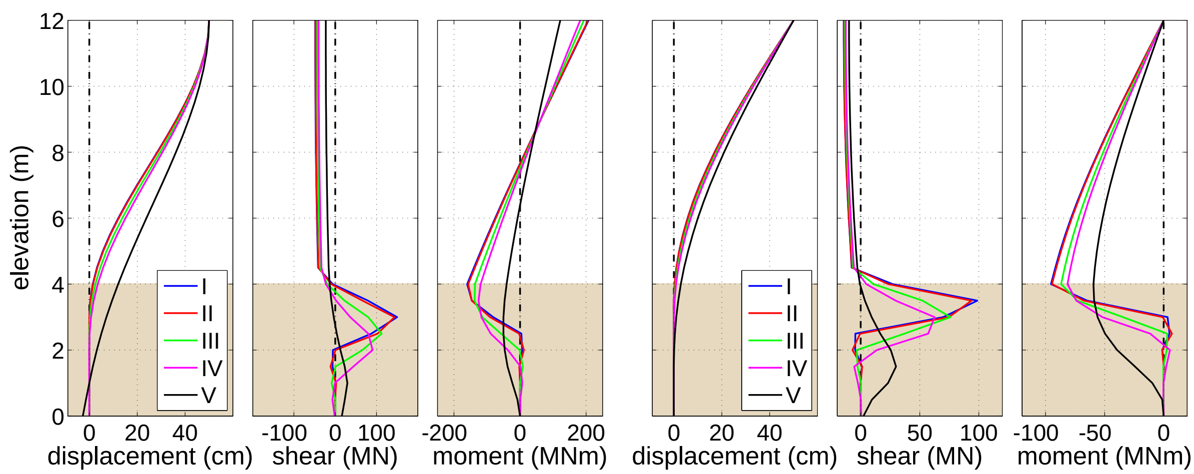

Figure 3.4 Shaft bending demands for site profile 2 using modified soil p-y curves with Reese rock curves for five rock classifications (I-V).

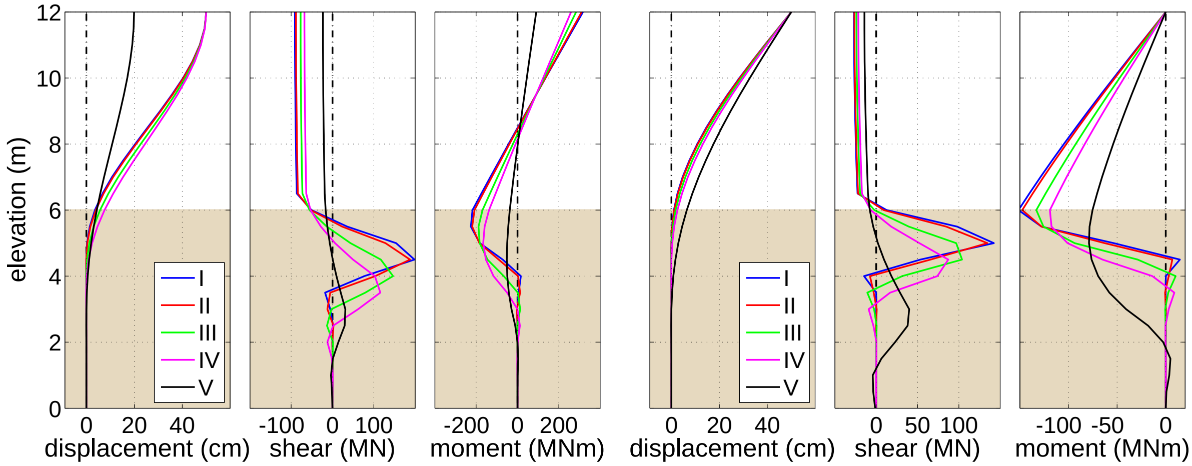

Figure 3.5 **Shaft bending demands for site profile 3 using API soil p-y curves with Reese rock curves for five rock classifications (I-V).**

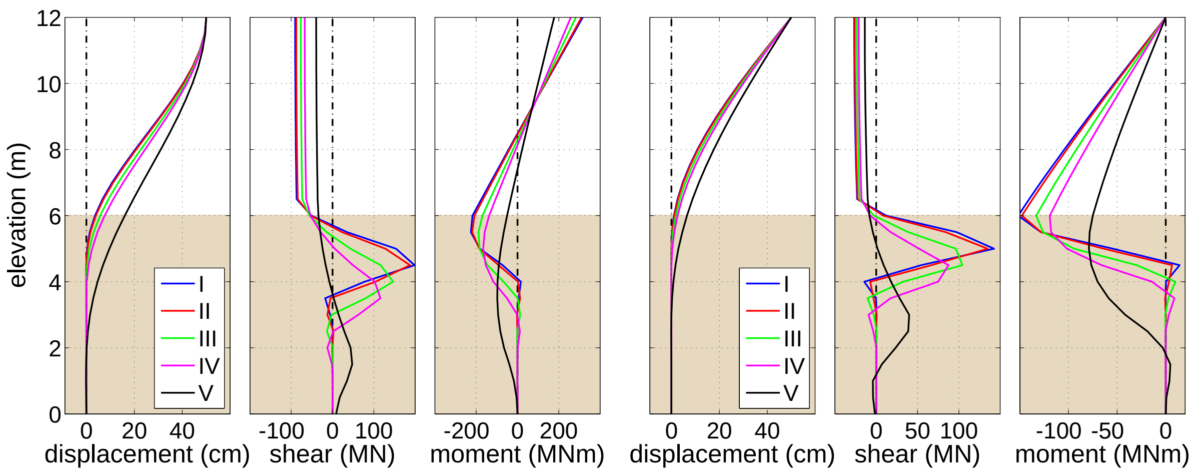

Figure 3.6 **Shaft bending demands for site profile 3 using modified soil p-y curves with Reese rock curves for five rock classifications (I-V).**

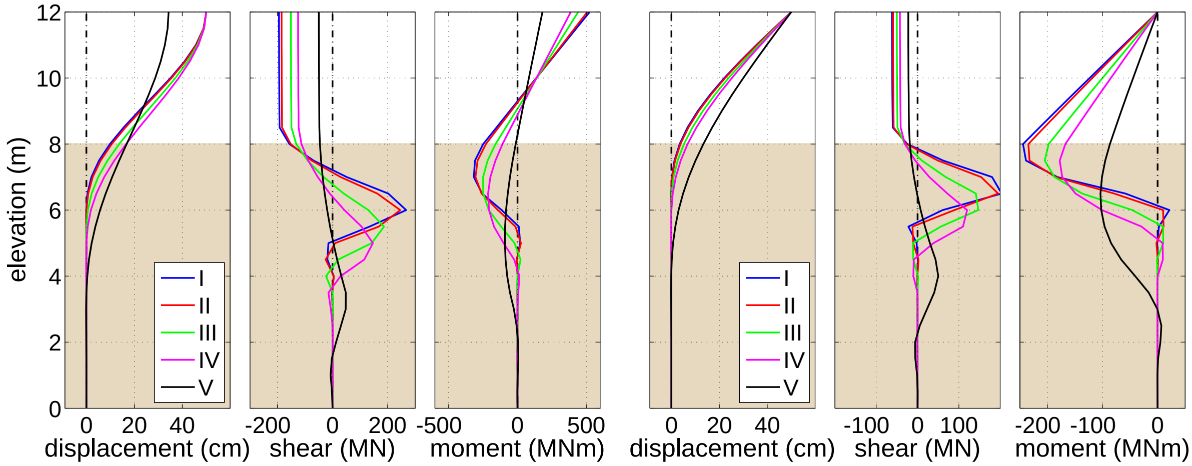

Figure 3.7 Shaft bending demands for site profile 4 using API soil p-y curves with Reese rock curves for five rock classifications (I-V).

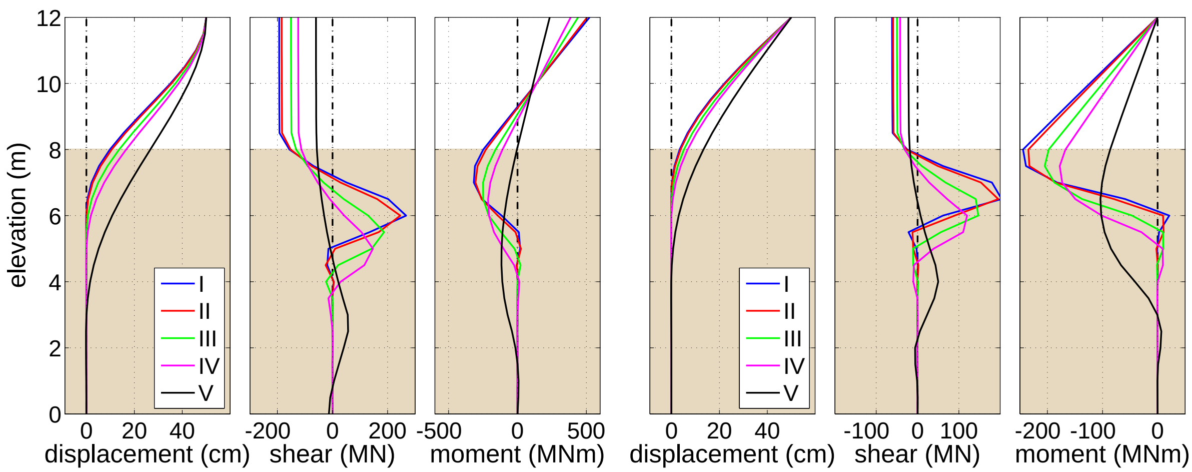

Figure 3.8 Shaft bending demands for site profile 4 using modified soil p-y curves with Reese rock curves for five rock classifications (I-V).

3.4 EFFECTS OF ROCK P-Y CURVE DEFINITION

This section uses the Liang et al. (2009) approach to develop rock p-y curves that are then applied to the BNWF model to assess the effects of varying the rock p-y curve definition method on the rock-socketed shaft problem. Figures 3.9 through 3.12 show the shaft displacement, shear force, and bending moment demands for each site profile using the Liang et al. (2009) rock p-y curves in the BNWF pushover model; Table 3.2 provides the corresponding shear force ratios for each considered case. For a given rock mass, the method proposed by Liang et al. (2009) generally produces p-y curves that have lower ultimate resistances and initial stiffness values than curves developed using the Reese (1997) approach. As a result, the maximum shear forces and bending moments in Figures 3.9 through 3.12 are generally less for identical lateral loadings and site conditions.

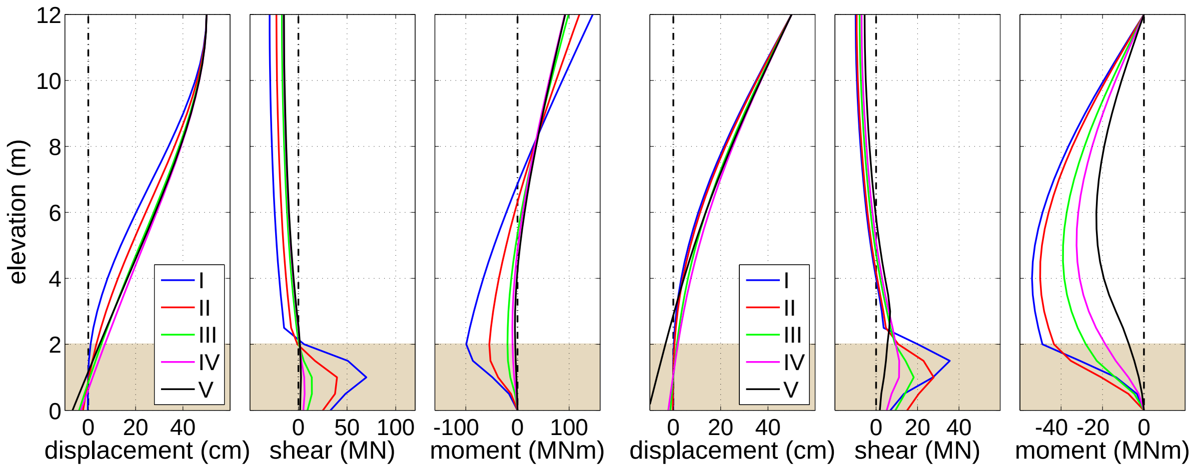

Figure 3.9 Shaft bending demands for site profile 1 using API soil p-y curves with Liang et al. rock curves for five rock classifications (I-V).

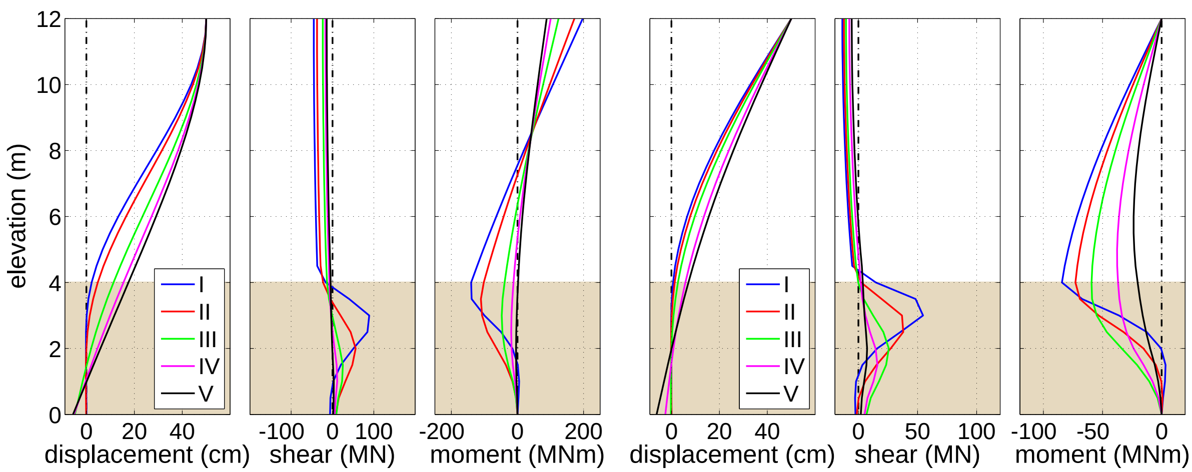

Figure 3.10 Shaft bending demands for site profile 2 using API soil p-y curves with Liang et al. rock curves for five rock classifications (I-V).

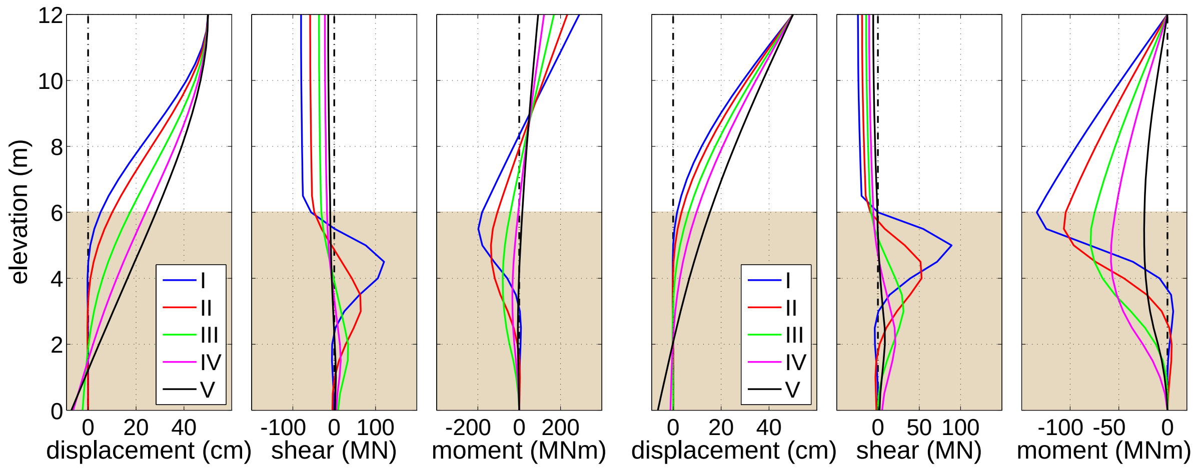

Figure 3.11 **Shaft bending demands for site profile 3 using API soil p-y curves with Liang et al. rock curves for five rock classifications (I-V).**

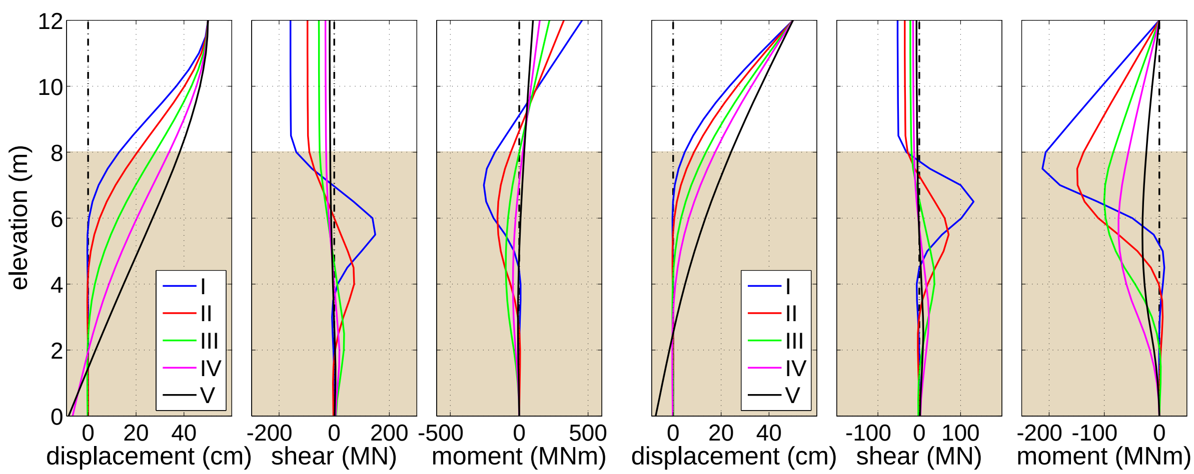

Figure 3.12 **Shaft bending demands for site profile 4 using API soil p-y curves with Liang et al. rock curves for five rock classifications (I-V).**

3.5 EFFECTS OF BEAM ELEMENT FORMULATION

Per Turner (2006), at least one state transportation agency has expressed concern that the magnification in shear force observed in the rock layer in BNWF analyses of rock-socketed shafts may be due to the Euler-Bernoulli beam theory assumptions commonly used in this type of analysis. To assess this concern, a series of analyses were conducted using beam elements with a Timoshenko (shear-deformable) formulation. These analyses use the same site profiles, shaft dimensions, and soil–rock properties discussed previously. The Timoshenko beam elements were assigned shear correction factors of 0.89 based on the circular cross section of the shaft and the work of Dong et al. (2010).

Figures 3.13 through 3.16 show the shaft displacement, shear force, and bending moment demands resulting from the BNWF analyses with the Timoshenko beam element formulation. A comparison with the corresponding results for the Euler-Bernouli beam elements (Figures 3.1, 3.3, 3.5, and 3.7) shows that the maximum shear force in the rock layer is reduced for the shear-deformable beam cases. This reduction appears to be most significant for the stronger rock classifications and for site profiles 1 and 2, where the thickness of the rock-socket is smaller in comparison to the shaft diameter.

Because the shear force at the ground surface is relatively the same for the two types of beam formulation, the reductions in maximum shear force observed in the rock layer for the Timoshenko beam cases leads to a lower shear force ratios. Table 3.3 shows the shear force ratios returned by the Timoshenko beam cases for all of the considered configurations and p-y curve definitions in the previous sections. Comparison with the corresponding results in Tables 3.1 and 3.2 demonstrates the reductions in shear force magnification brought about by the use of a shear-deformable element formulation in the shaft.

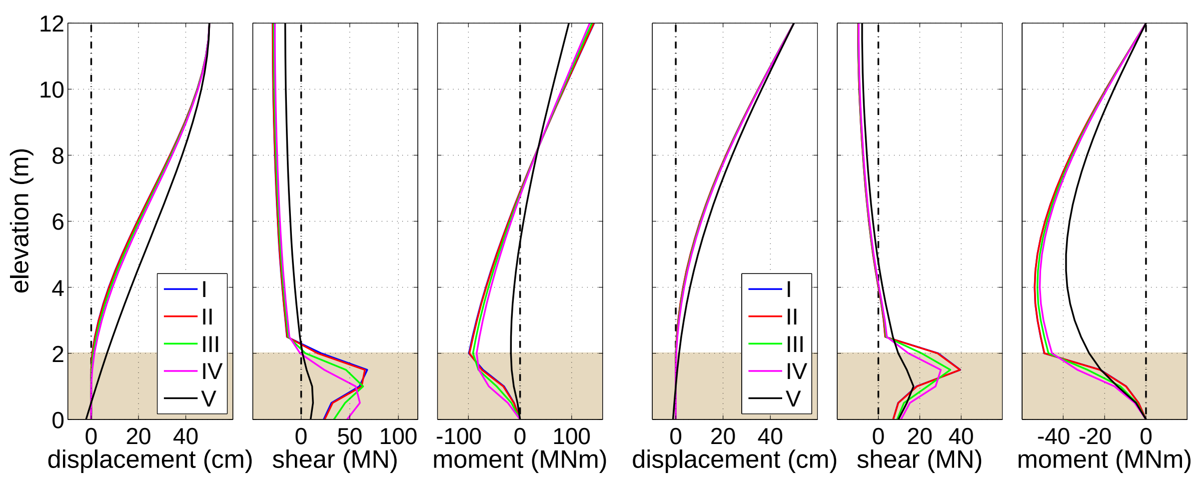

Figure 3.13 Shaft bending demands for site profile 1 using API soil p-y curves, Reese rock curves, and Timoshenko beam elements for five rock classifications (I-V).

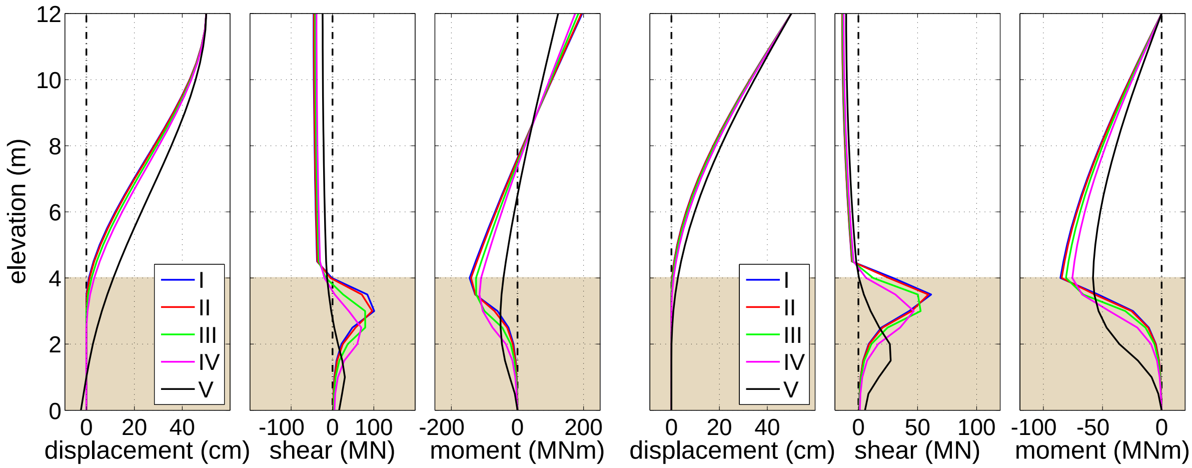

Figure 3.14 **Shaft bending demands for site profile 2 using API soil p-y curves, Reese rock curves, and Timoshenko beam elements for five rock classifications (I-V).**

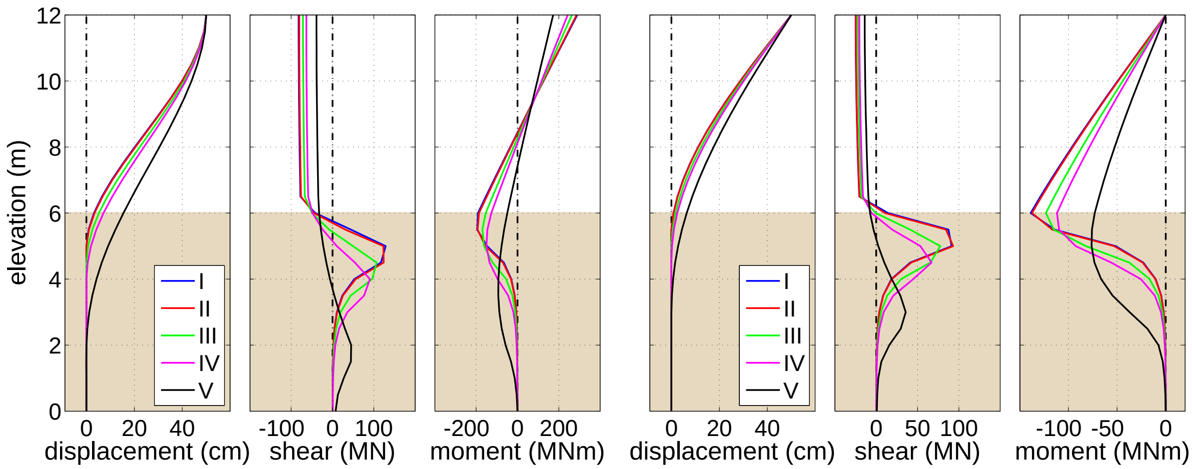

Figure 3.15 **Shaft bending demands for site profile 3 using API soil p-y curves, Reese rock curves, and Timoshenko beam elements for five rock classifications (I-V).**

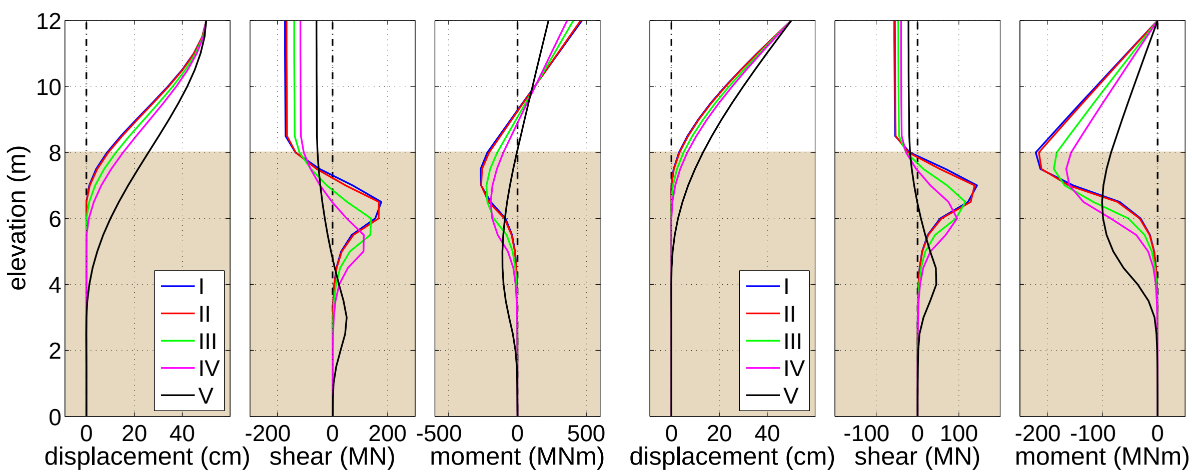

Figure 3.16 **Shaft bending demands for site profile 4 using API soil p-y curves, Reese rock curves, and Timoshenko beam elements for five rock classifications (I-V).**

Table 3.3 Shear force ratios for BNWF analyses with Timoshenko beam element formulation.

Site Profile	Rock p-y Curves	Soil p-y Curves	Shaft Head Condition	Rock Class I	II	III	IV	V
1	Reese	API	fixed	2.31	2.24	2.26	2.23	0.74
			free	4.01	4.00	3.59	3.16	2.15
		Modified	fixed	2.42	2.35	2.40	2.44	0.77
			free	4.57	4.56	3.98	3.51	2.40
	Liang	API	fixed	2.14	1.77	0.82	0.42	0.18
			free	3.21	2.80	2.28	1.59	1.22
		Modified	fixed	2.29	1.87	0.87	0.43	0.16
			free	3.63	3.30	2.55	1.74	1.24
2	Reese	API	fixed	2.21	2.15	1.89	1.80	1.25
			free	4.46	4.32	3.98	3.72	2.63
		Modified	fixed	2.25	2.19	1.95	1.85	1.31
			free	4.65	4.51	4.23	3.92	2.85
	Liang	API	fixed	1.80	1.42	1.07	0.67	0.22
			free	3.35	2.88	2.38	2.07	1.29
		Modified	fixed	1.84	1.46	1.12	0.70	0.22
			free	3.55	3.01	2.55	2.28	1.44
3	Reese	API	fixed	1.57	1.54	1.50	1.43	1.17
			free	3.67	3.78	3.49	3.29	2.57
		Modified	fixed	1.58	1.55	1.51	1.45	1.19
			free	3.74	3.85	3.55	3.36	2.68
	Liang	API	fixed	1.38	1.06	0.92	0.71	0.28
			free	3.29	2.60	2.06	1.95	1.48
		Modified	fixed	1.39	1.07	0.94	0.73	0.29
			free	3.35	2.66	2.15	2.08	1.64
4	Reese	API	fixed	1.03	1.01	1.01	0.98	0.88
			free	2.57	2.53	2.49	2.39	2.08
		Modified	fixed	1.03	1.01	1.01	0.98	0.90
			free	2.58	2.54	2.51	2.41	2.12
	Liang	API	fixed	0.84	0.71	0.64	0.60	0.30
			free	2.25	1.89	1.61	1.55	1.48
		Modified	fixed	0.85	0.71	0.65	0.61	0.31
			free	2.27	1.90	1.63	1.60	1.57

3.6 3D FINITE ELEMENT MODEL

In an attempt to validate the results from the BNWF models, 3D FEM models were created for the same single rock-socketed shaft system described in the BNWF analysis sections. The mesh for the 10-m soil, 2-m rock profile is shown in Figure 3.17, with colors designating the soil and rock layers. This mesh is typical of those used for all soil–rock configurations. The 3D models used force-based beam-column elements to represent the shaft, stabilized single-point integration continuum elements to represent the soil and rock, and the beam-solid contact element of Petek (2006) to represent the soil–shaft interface.

The cohesionless soil layer was modeled using a nested yield surface constitutive model with strength based on the initial state of stress in the elements, and the friction angle, $\phi = 31°$, assumed for the layer. The elastic properties for this layer, bulk modulus, $\kappa = 220$ MPa, and shear modulus, $G = 95$ MPa, were assigned based on correlations with the soil-friction angle. Two approaches were used to model the constitutive response of the rock layer:

- a $J2$ plasticity model with strength assigned in a similar manner to that used for the Reese (1997) rock p-y curves
- a Drucker-Prager plasticity model with strength assigned in a manner similar to the p-y curves of Liang et al. (2009).

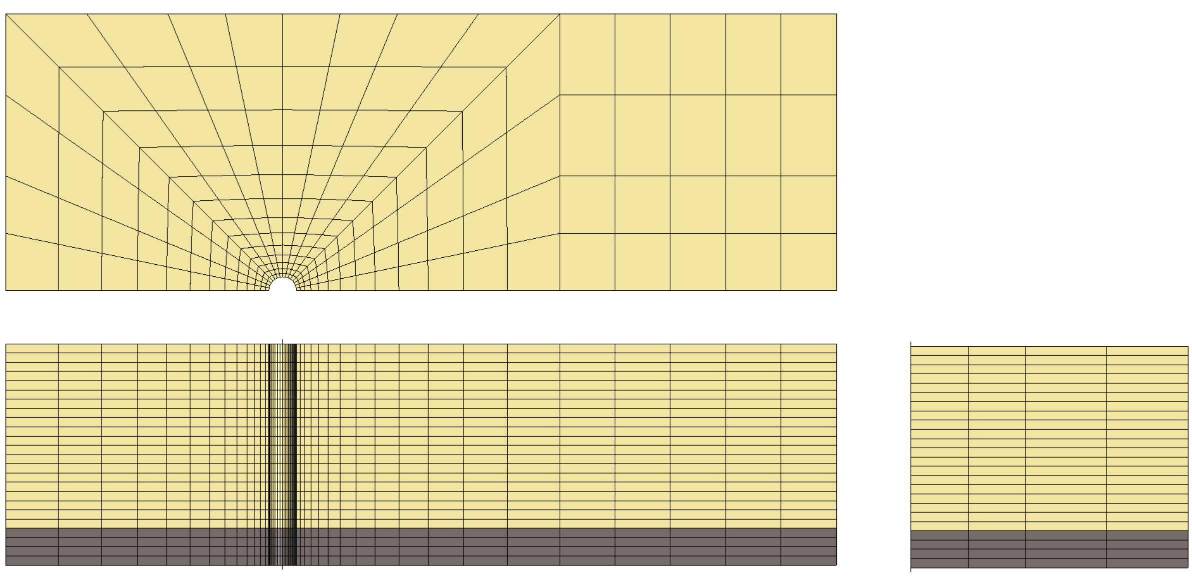

Figure 3.17 Overview of 3D FE mesh for 10 m soil, 2 m rock, profile. Meshes for other profiles (not shown) are similar.

The elastic parameters for each case are based on the rock mass elastic moduli reported in Table 2.1 and an assumed Poisson's ratio of $\nu = 0.25$. The yield strength of the $J2$ model is based on the maximum shear stress corresponding to the reduced rock compressive strengths of Table 2.1, i.e.,

$$\sigma_Y = 0.5\alpha_r q_u \tag{3.21}$$

where α_r is the strength reduction parameter of Equation (3.4) that accounts for the effect of rock quality index on the strength of the rock mass. The strength parameters for the Drucker-Prager model are assigned as the effective friction angle and cohesion computed from the Hoek-Brown strength criterion (Hoek et al., 2002) (with the vertical effective stress taken as the vertical stress at the interface between the soil and rock layers), and the previously reported Hoek-Brown constants used to define the Liang et al. (2009) rock p-y curves in the BNWF analysis.

The shaft was modeled in the same manner used in the Euler beam BNWF analyses; linear elastic behavior is designated with the section and material properties previously reported. The models were analyzed for both the fixed- and free-head boundary conditions considered previously; in both cases, the shaft head was displaced laterally by 0.5 m in a pseudo-dynamic (no inertial forces) pushover analysis.

3.7 COMPARISON OF 3D FE ANALYSIS AND BNWF ANALYSES

The 3D pushover analyses were compared to the BNWF results in terms of the shear force ratios for the maximum shear demands in the two layers, and graphically in terms of the shaft displacement, shear force, and bending moment profiles for each set of cases. Table 3.4 provides the 3D FE analysis shear force ratios for each combination of site profile, rock constitutive model, and rock classification. As shown, the ratios for the 3D cases with the Drucker-Prager modeling approach are generally less than those for the BNWF analyses with the Reese rock p-y curves, and greater than those for the BNWF results using the Liang et al. rock p-y curves. This trend also holds for most of the site profile 1 and 2 results returned using the $J2$ rock model; however, the 3D results for the thicker rock layer cases displayed lower ratios than both sets of rock p-y curves.

Shear force ratios are a useful indicator of the relative shear force demands in each layer for a given case; however, they do not provide a useful comparison of the relative bending demands between the various analysis approaches. Figures 3.18 through 3.37 show the shaft displacement, shear force, and bending moment demands resulting from each of the two 3D model cases (3D-J2 for the $J2$ rock model, and 3D-DP for the Drucker-Prager rock model) as well as the BNWF cases with the API soil p-y curves and both the Reese and Liang et al. rock p-y curves. Figures 3.18 through 3.22 provide this comparison for the site profile 1 configurations, with Figures 3.23 through 3.27 for site profile 2, Figures 3.28 through 3.32 for site profile 3, and Figures 3.33 through 3.37 for site profile 4.

The form of the shear force and bending moment diagrams are generally similar across all of the considered cases, though the local maxima occur in different places for each analysis type. The magnitude of the maximum shear forces in the 3D cases generally falls in between the values for the Reese and Liang et al. curves, and the maxima for the Drucker-Prager results are generally greater than those for the $J2$ rock cases. The $J2$ rock model appears to under-represent the strength of the strongest rock classes, while over-representing the strength of the weaker rock classes. The Drucker-Prager rock model appears to correct the problem with over-representation of the weaker rock strength, while perhaps over-representing the strength of rock class I. Overall, the results presented here demonstrate that the shear force magnification deemed problematic for rock-socketed shaft design depends on the kinematics of the shaft (free- or fixed-head) and the technique used to model the rock mass. Although all of the cases display the magnification response, the level of magnification clearly depends more on the type of rock model used (Reese vs. Liang et al., $J2$ vs. Drucker-Prager) than on the type of analysis conducted (BNWF vs. 3D).

Table 3.4 Shear force ratios for 3D FEA with two rock constitutive models.

Site Profile	Rock Model	Shaft Head Condition	Rock Class I	II	III	IV	V
1	$J2$ Plasticity	fixed	2.41	2.07	1.85	1.33	0.41
		free	3.98	3.56	3.03	2.51	1.31
	Drucker-Prager	fixed	2.44	1.99	1.58	0.92	0.22
		free	3.83	3.22	2.57	1.76	0.90
2	$J2$ Plasticity	fixed	1.98	1.76	1.37	1.18	0.58
		free	4.37	3.69	2.90	2.23	1.67
	Drucker-Prager	fixed	2.23	1.60	1.10	0.82	0.34
		free	4.27	3.28	2.29	1.73	1.15
3	$J2$ Plasticity	fixed	1.35	1.21	1.10	0.82	0.54
		free	3.62	3.07	2.52	2.02	1.46
	Drucker-Prager	fixed	1.74	1.21	0.83	0.51	0.34
		free	3.79	2.90	2.08	1.39	1.08
4	$J2$ Plasticity	fixed	0.72	0.72	0.65	0.55	0.41
		free	2.24	2.12	1.81	1.52	1.06
	Drucker-Prager	fixed	1.12	0.75	0.50	0.30	0.27
		free	2.70	2.05	1.51	1.04	0.78

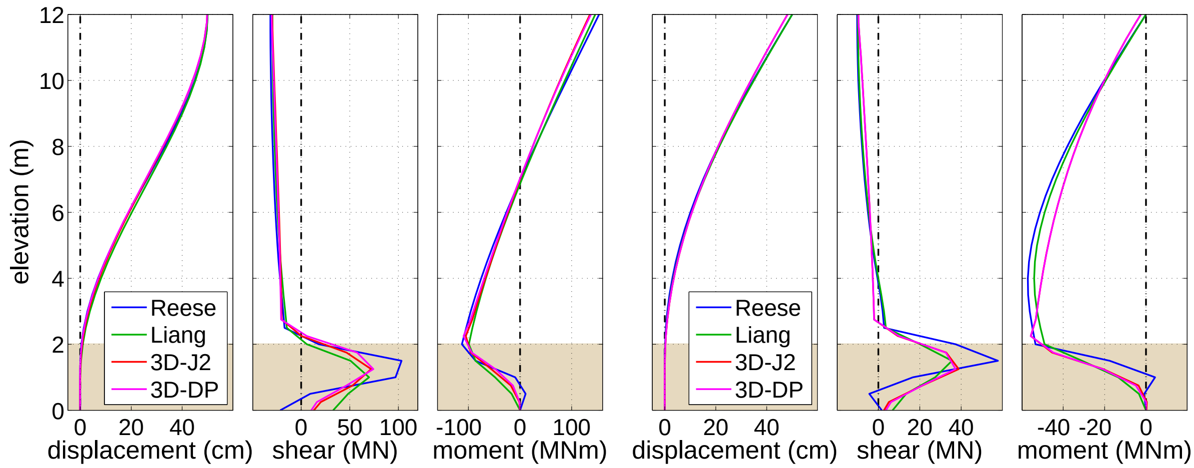

Figure 3.18 Comparison of shaft bending demands for site profile 1 with rock class I.

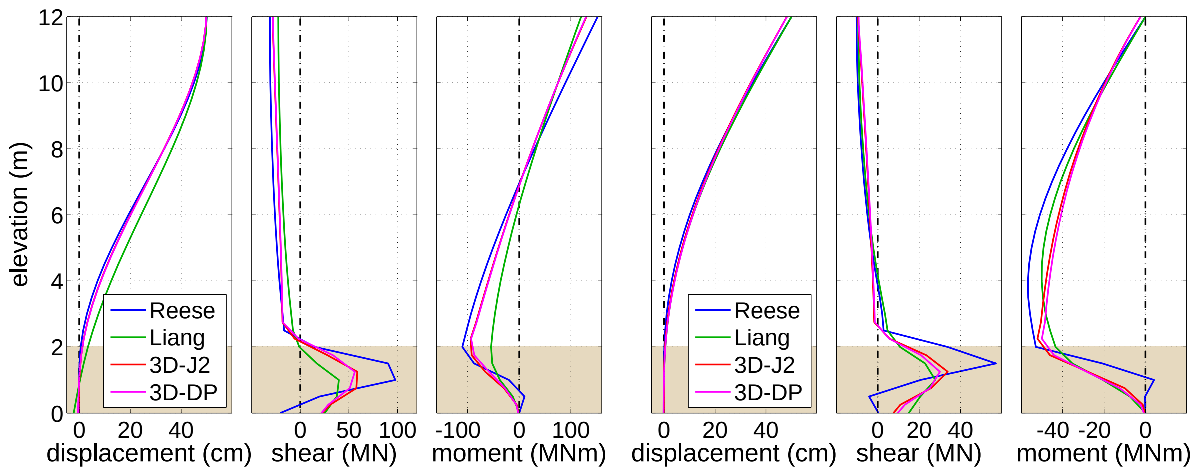

Figure 3.19 Comparison of shaft bending demands for site profile 1 with rock class II.

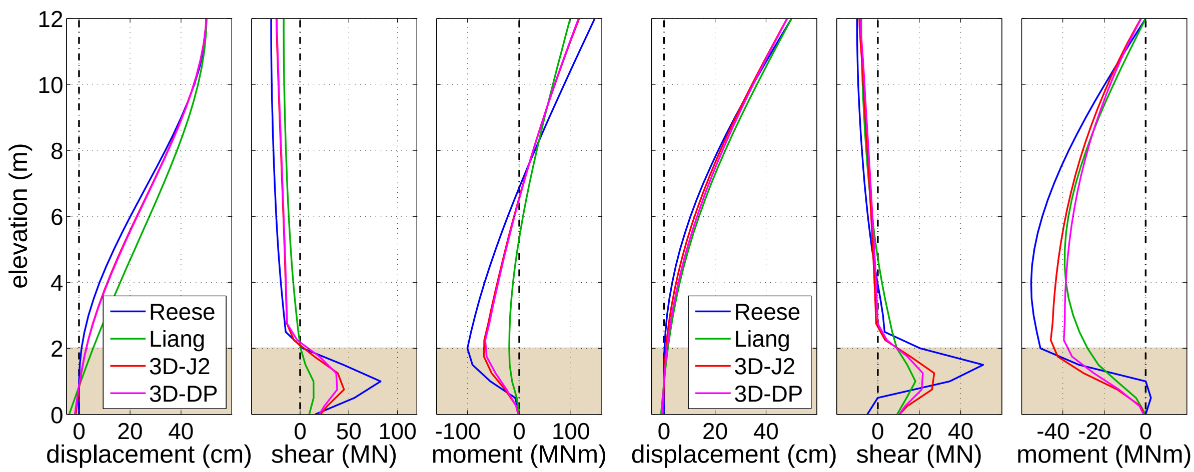

Figure 3.20 Comparison of shaft bending demands for site profile 1 with rock class III.

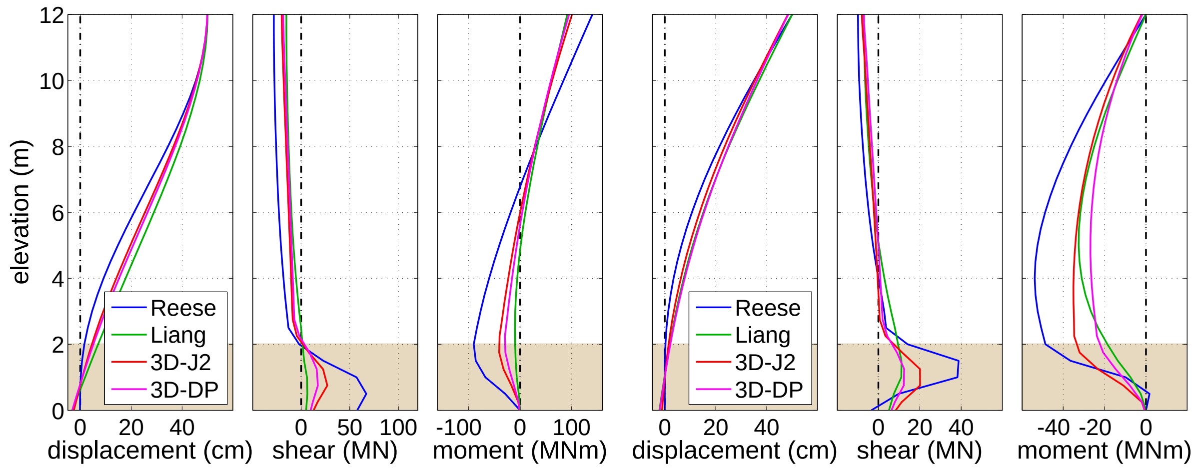

Figure 3.21 Comparison of shaft bending demands for site profile 1 with rock class IV.

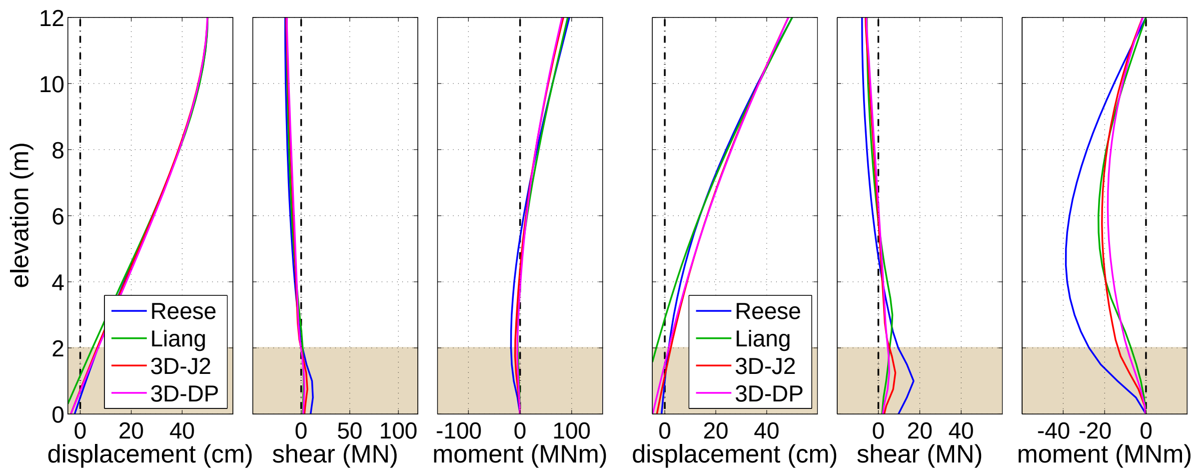

Figure 3.22 Comparison of shaft bending demands for site profile 1 with rock class V.

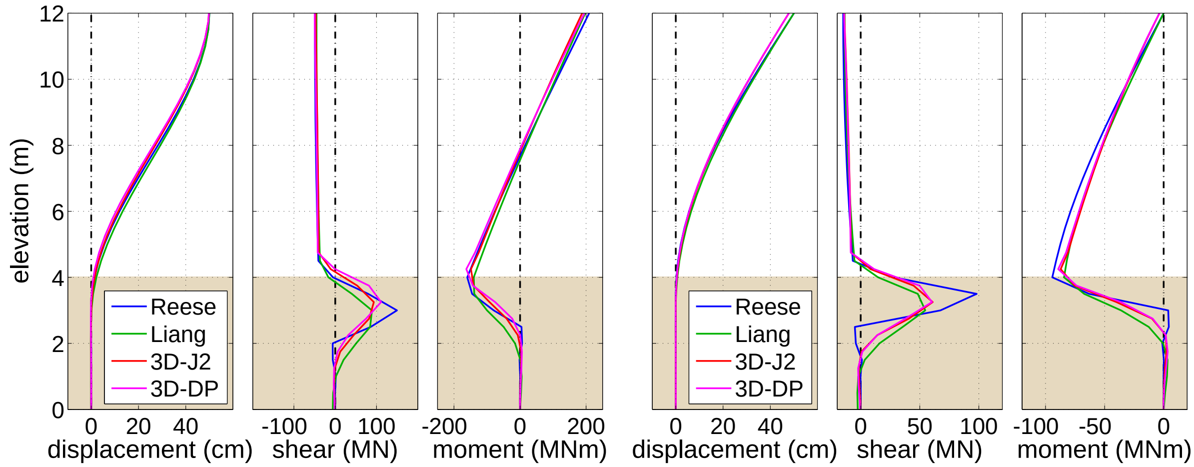

Figure 3.23 Comparison of shaft bending demands for site profile 2 with rock class I.

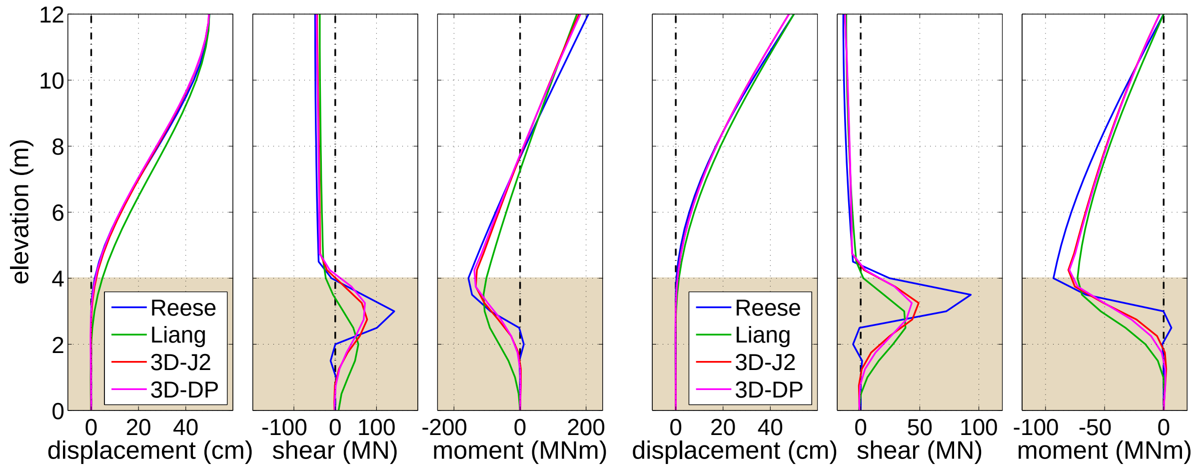

Figure 3.24 Comparison of shaft bending demands for site profile 2 with rock class II.

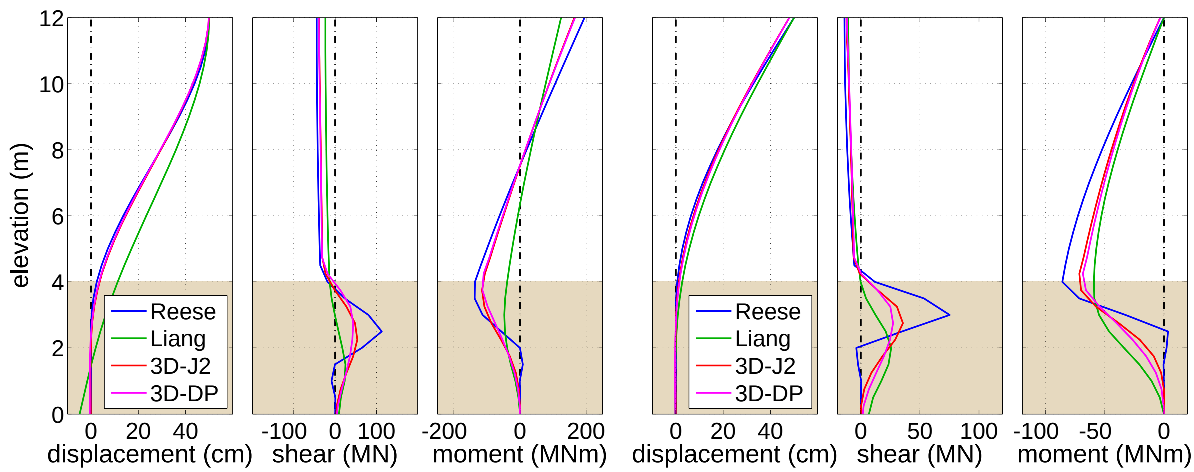

Figure 3.25 Comparison of shaft bending demands for site profile 2 with rock class III.

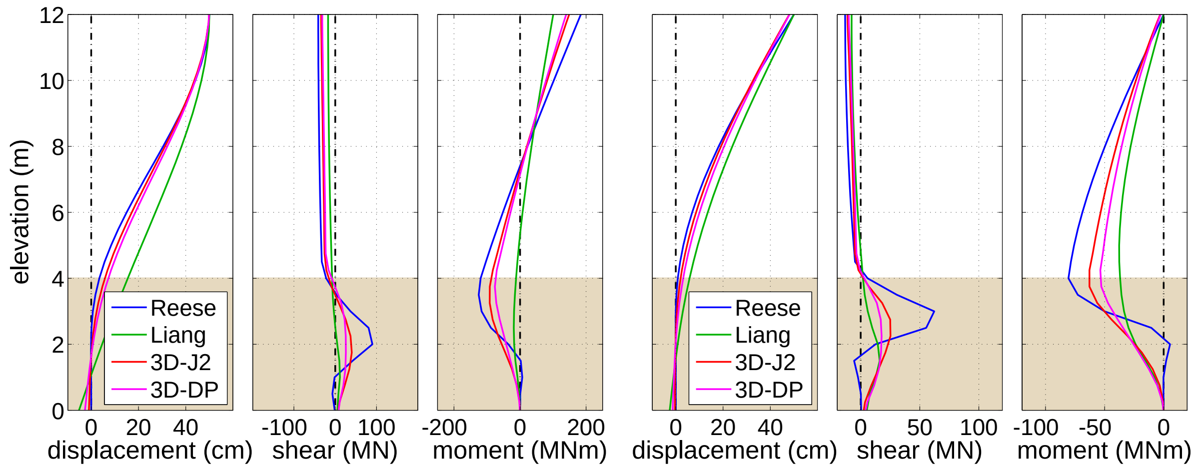

Figure 3.26 Comparison of shaft bending demands for site profile 2 with rock class IV.

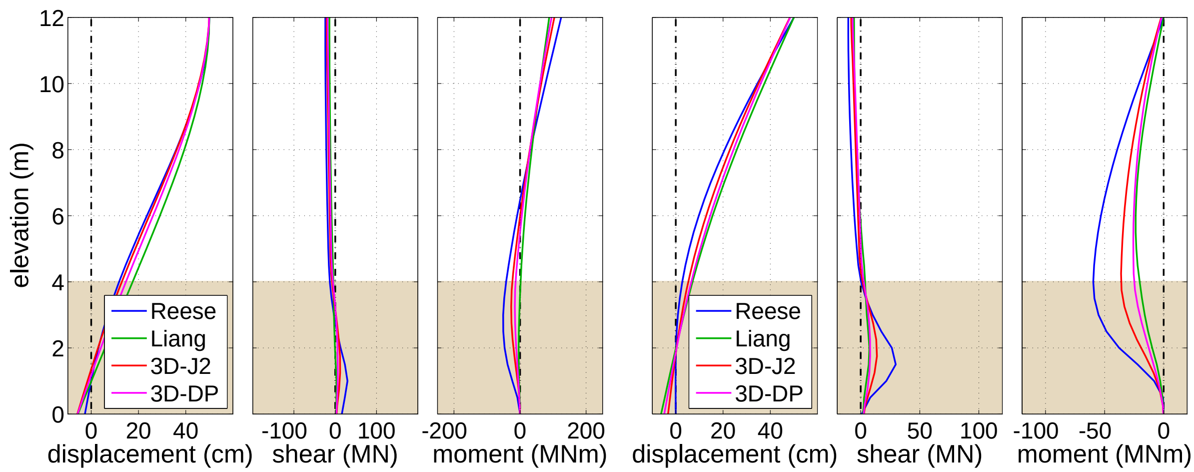

Figure 3.27 Comparison of shaft bending demands for site profile 2 with rock class V.

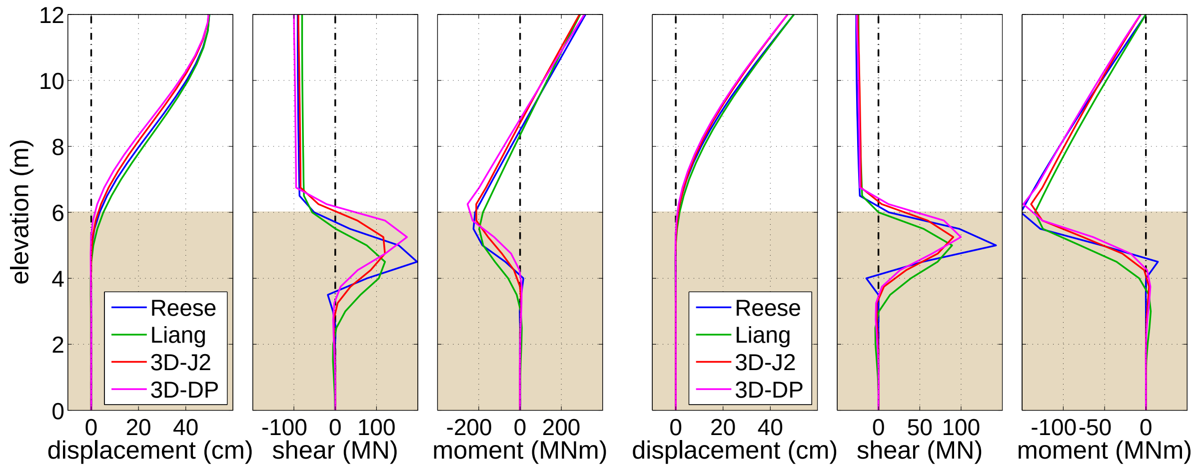

Figure 3.28 Comparison of shaft bending demands for site profile 3 with rock class I.

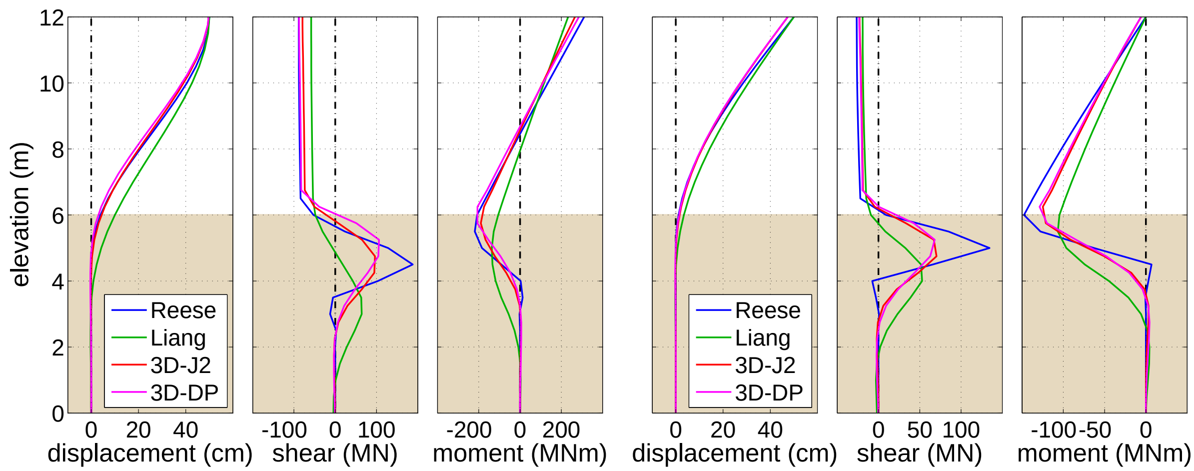

Figure 3.29 Comparison of shaft bending demands for site profile 3 with rock class II.

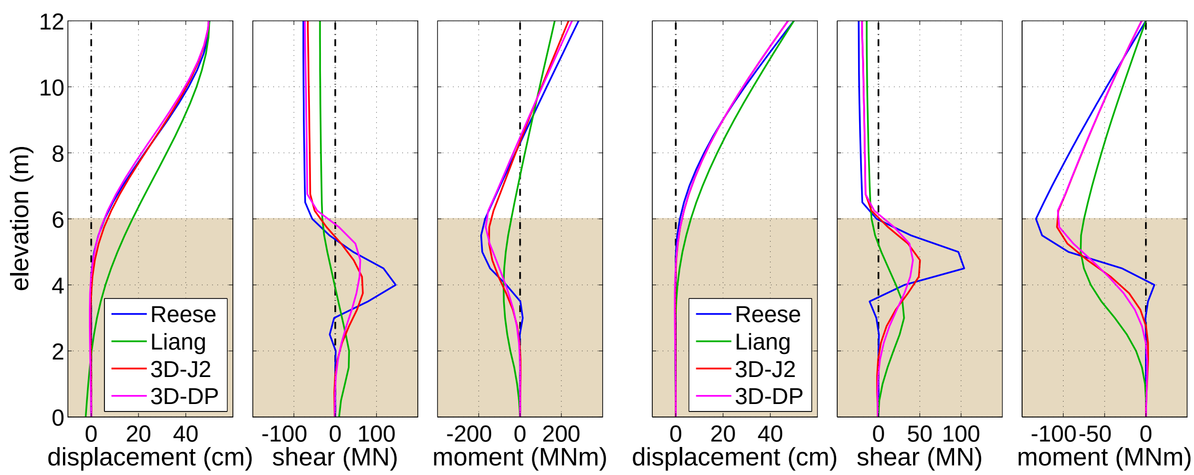

Figure 3.30 Comparison of shaft bending demands for site profile 3 with rock class III.

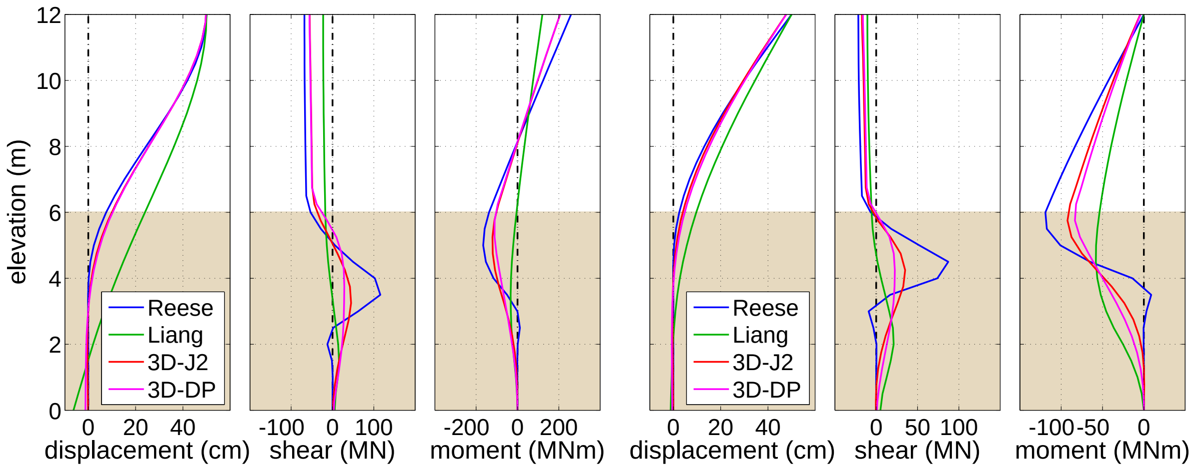

Figure 3.31 Comparison of shaft bending demands for site profile 3 with rock class IV.

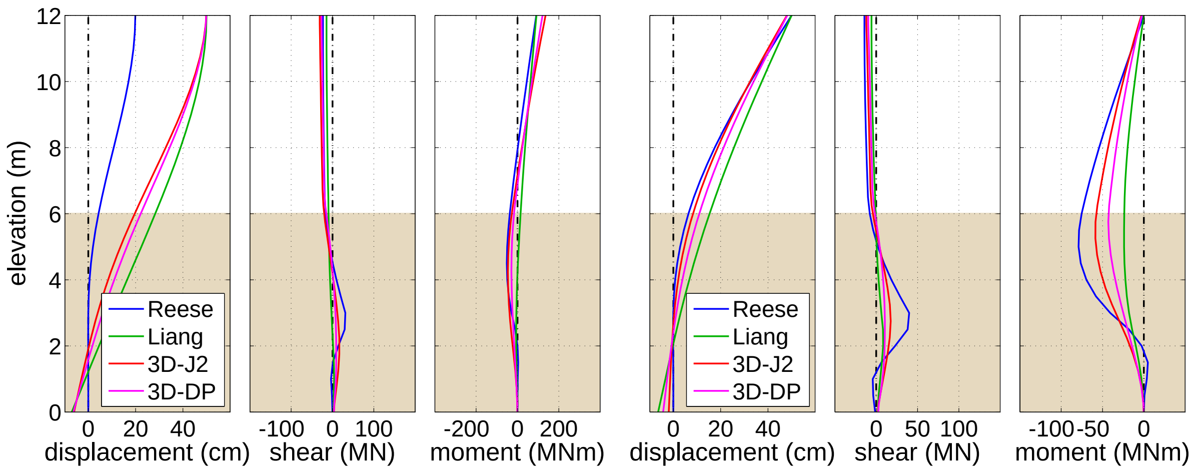

Figure 3.32 Comparison of shaft bending demands for site profile 3 with rock class V.

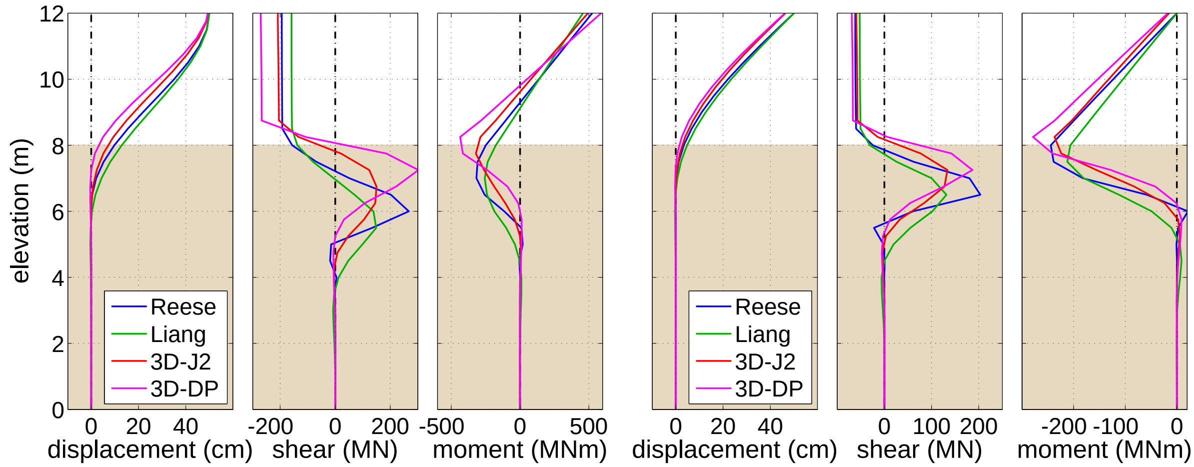

Figure 3.33 Comparison of shaft bending demands for site profile 4 with rock class I.

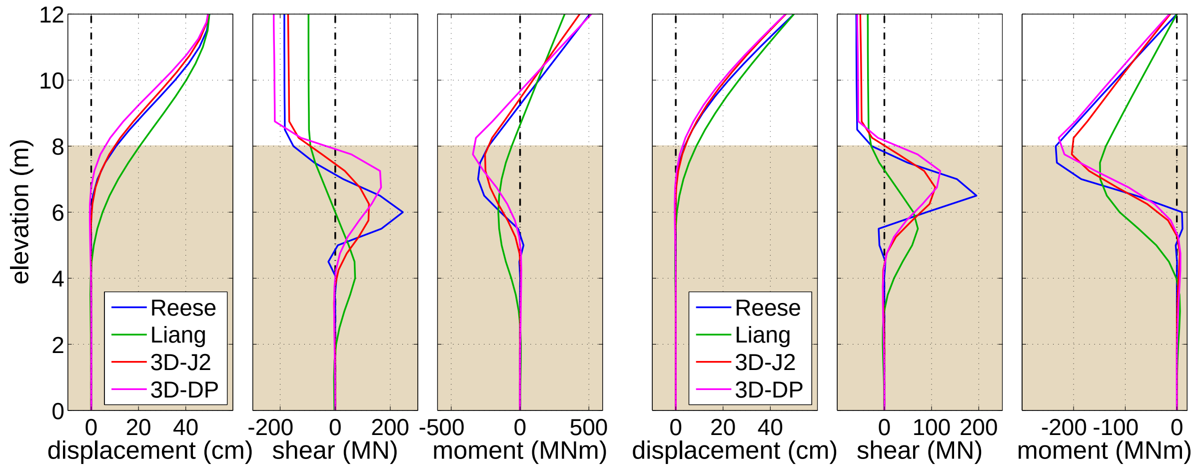

Figure 3.34 Comparison of shaft bending demands for site profile 4 with rock class II.

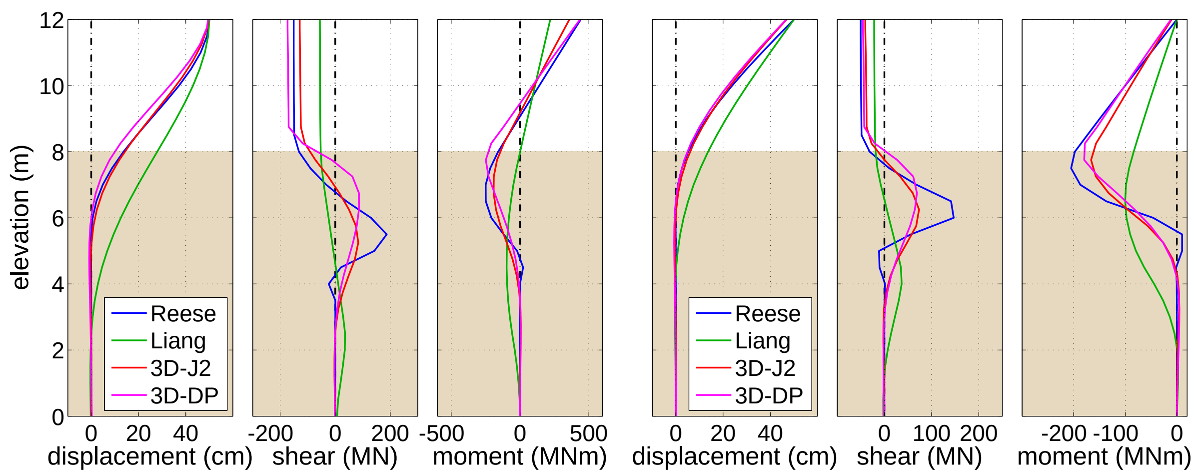

Figure 3.35 Comparison of shaft bending demands for site profile 4 with rock class III.

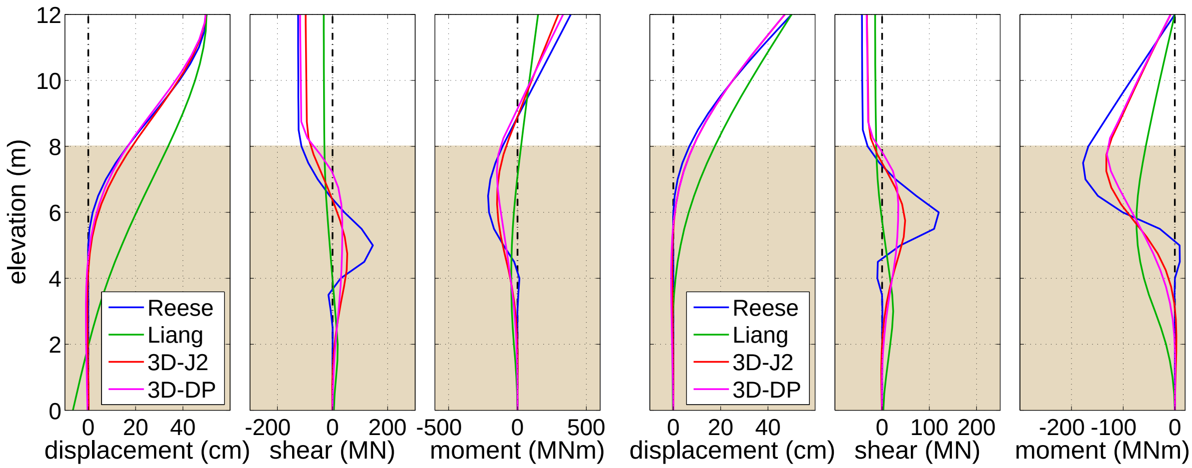

Figure 3.36 Comparison of shaft bending demands for site profile 4 with rock class IV.

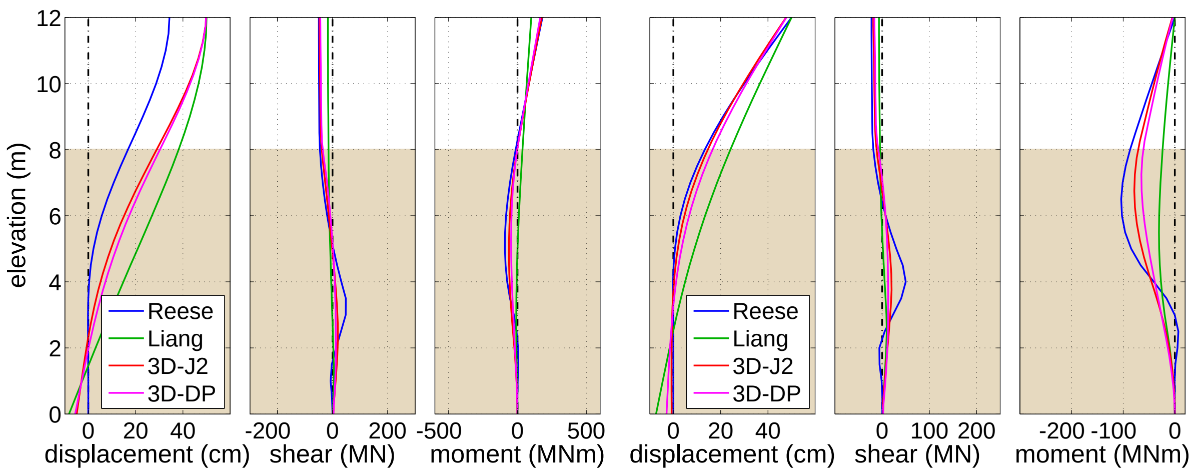

Figure 3.37 Comparison of shaft bending demands for site profile 4 with rock class V.

3.8 SUMMARY

1. There are only minor differences between the results for the two sets of cohesionless soil p-y curves. For all cases, as the quality of the rock increases, the contrast between the upper and lower layer shear-force demands also increases. The shaft head boundary condition changes the magnitude of the shear force and bending moment demands in the shaft, with the free-head condition inducing lower demands for an equal amount of lateral head displacement.

2. As the thickness of the rock layer increases in comparison to the thickness of the soil layer, the ratio of the maximum shear-force demands in each layer tends to decrease.

3. The shear force ratio are much lower when using the Liang et al. (2009) approach to develop rock p-y curves.

4. A comparison of results from BNWF analyses with the Timoshenko beam element formulation to the corresponding results for the Euler-Bernouli beam elements show that the maximum shear force in the rock layer is reduced for the shear-deformable beam cases.

5. The ratios for the 3D cases with Drucker-Prager modeling approach are generally less than those for the BNWF analyses with the Reese rock p-y curves, and greater than those for the BNWF results using the Liang et al. (2009) rock p-y curves, and the maxima for the Drucker-Prager results are generally greater than those for the $J2$ rock cases. The level of magnification depends more on the type of rock model used (Reese vs. Liang et al., $J2$ vs. Drucker-Prager) than on the type of analysis conducted (BNWF vs. 3D).

4 End-Shaft Finite Element Formulation

4.1 INTRODUCTION

This chapter introduces a simple uplift, single-node FE formulation that can be used together with BNWF p-y springs to better describe the interaction between the toe of the shaft and the underlain rock.

4.2 PROBLEM STATEMENT

A schematic of the problem is shown in Figure 4.1, where δ and θ are the vertical displacement and rotation of the shaft end when subjected to lateral load, and R is the radius of the shaft.

From geometry, the vertical displacement of a point within shaft toe can be calculated as,

$$u(\xi) = \theta \cdot \xi = \theta(x + c) \tag{4.1}$$

in which $c = \delta/\theta$ and downward is positive. Written in polar coordinates,

$$x = r\,cos\phi; \quad y = r\,sin\phi \tag{4.2}$$

$$u(r, \phi) = \theta(c + r\,cos\phi) \tag{4.3}$$

If below each point we assume the existence of a spring with stiffness (subgrade reaction modulus) k, the normal stress σ can be expressed as a fuction of u as,

$$\sigma = ku = k\theta(c + r\,cos\phi) \tag{4.4}$$

Using this framework, the stress resultants (i.e., P and M) can be calculated by integration over the contact area, $\bar{A}$ for which $u \geq 0$ ($\bar{A} \leq A$, where A is the shaft cross-sectional area),

$$P = \int_{\bar{A}} \sigma dA \tag{4.5}$$

$$M_y = \int_{\bar{A}} \sigma x dA \tag{4.6}$$

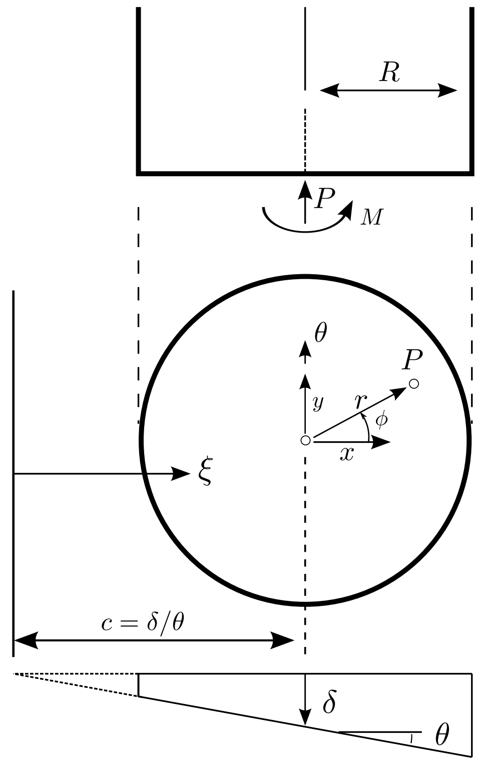

Figure 4.1 Schematic drawing for general cases.

4.3 ELEMENT FORMULATION FOR ROTATION IN ONE DIRECTION

Depending on the area in contact with the rock two cases arise: Case I, with $c \geq R$ and $\bar{A} = A$, indicating the shaft toe is in full contact with the rock; and Case II, with $c < R$, indicating the shaft is not fully in contact with rock underlain.

4.3.1 Formulation for Case I ($c \geq R$)

Written in polar coordinates

$$dA = rdrd\phi \tag{4.7}$$

Replacing in 4.5 and 4.6, the resultant forces can be calculated from integration,

$$\begin{aligned} P = \int_{\bar{A}} \sigma dA &= k\theta \int_0^R \int_0^{2\pi} (c + r\,cos\phi) rdrd\phi \\ &= k\theta[2\pi c\frac{R^2}{2} + sin\phi|_0^{2\pi} \frac{R^3}{3}] \\ &= k\pi R^2 \delta \\ &= kA\delta \end{aligned} \tag{4.8}$$

$$
\begin{aligned}
M_y = \int_{\bar{A}} \sigma x dA = k\theta \int_0^R \int_0^{2\pi} (c + r\, cos\phi) r\, cos\phi \cdot r dr d\phi \\
= k\theta [\frac{R^3}{3} c\, sin\phi \Big|_0^{2\pi} + \frac{R^4}{4}(\pi + \frac{1}{4} sin 2\phi \Big|_0^{2\pi})] \qquad (4.9)\\
= k\frac{\pi R^4}{4}\theta \\
= kI\theta
\end{aligned}
$$

where k is the stiffness (subgrade reaction modulus) of the rock or soil, A is the cross-sectional area of shaft, and I is the area moment of inertia of the shaft. Representative values of k can be obtained from the numerical simulations presented in section 4.5.

4.3.2 Formulation for Case II ($c < R$)

For Case II, only part of the shaft toe is in contact with rock (part of circle on the right side of line 1-2 shown in Figure 4.2); therefore $\bar{A} < A$. From geometry we have

$$\phi_1 = -\phi_2 = -\bar{\phi} \qquad (4.10)$$

$$\frac{c}{R} = cos(\pi - \bar{\phi}) = -cos\bar{\phi} \qquad (4.11)$$

$$\bar{\phi} = arccos(-\frac{c}{R}) \qquad (4.12)$$

$$b(\xi) = 2Rsin(\bar{\phi})(1 - \frac{\xi}{c}) \qquad (4.13)$$

where ξ is a natural coordinate measured from line 1-2 as indicated in Figure 4.2

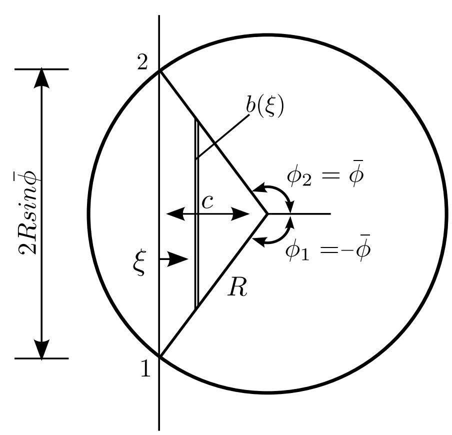

Figure 4.2 Cross section of the base of shaft for case II; $c < R$.

Under these conditions, Equation 4.5 becomes

$$\begin{aligned} P &= 2\int_0^R\int_0^{\bar{\phi}} k\theta(c+r\,cos\phi)rdrd\phi + \int_0^c k\theta\xi b(\xi)d\xi \\ &= 2\bar{\phi}k\theta c\frac{R^2}{2} + 2k\theta\frac{R^3}{3}sin\bar{\phi} + 2Rsin\bar{\phi}(k\theta)(\frac{c^2}{2}-\frac{c^3}{3c}) \\ &= k\theta[R^2\bar{\phi}c + \frac{2}{3}R^3sin\bar{\phi} + \frac{1}{3}Rc^2sin\bar{\phi}] \end{aligned} \tag{4.14}$$

$$P = k[R^2\bar{\phi}\delta + \underbrace{\frac{2}{3}R^3sin\bar{\phi}\,\theta}_{\text{linear coupling}} + \underbrace{\frac{1}{3}Rsin\bar{\phi}\frac{\delta^2}{\theta}}_{\text{nonlinear coupling}}] \tag{4.15}$$

and Equatoin 4.6 becomes

$$\begin{aligned} M &= 2\int_0^R\int_0^{\bar{\phi}} k\theta(c+r\,cos\phi)r\,cos(\phi)rdrd\phi + \int_0^c (k\theta\xi)(\xi-c)(2Rsin\bar{\phi})(1-\frac{\xi}{c})d\xi \\ &= 2k\theta[c\frac{R^3}{3}sin\bar{\phi} + \frac{R^4}{4}(\frac{\bar{\phi}}{2}+\frac{1}{4}sin(2\bar{\phi})] + 2Rsin(\bar{\phi})k\theta(-\frac{c^3}{12}) \end{aligned} \tag{4.16}$$

$$M = k[\frac{2}{3}R^3sin\bar{\phi}\,\delta + \frac{R^4}{4}(\bar{\phi}+\frac{1}{2}sin(2\bar{\phi}))\theta - \frac{1}{6}sin(\bar{\phi})\frac{\delta^3}{\theta^2}] \tag{4.17}$$

From Equations 4.15 and 4.17 we see $P(\delta,\theta)$ and $M(\delta,\theta)$. By grouping P and M in a force vector $\begin{Bmatrix} P \\ M \end{Bmatrix} := \{\underline{F}\}$, the kinematic vector (or degree of freedom vector) can be formed as $\begin{Bmatrix} \delta \\ \theta \end{Bmatrix} := \{\underline{d}\}$. The sequence within these two vectors matters since $\{\underline{F}\} \cdot \{\underline{d}\}$ must result in the correct work quantity. From Equations 4.15 and 4.17 it is clear the problem $\{\underline{F}\} = f(\{\underline{d}\})$ is nonlinear. To evaluate the corresponding tangential stiffness matrix $\{\underline{K}\}$ a linearization process is required.

4.3.3 Linearization of Case I

From the definition of the differential of a function $d\{\underline{F}\} =: [K]\,d\{\underline{d}\}$ is the definition of $[\underline{\underline{K}}]$. From Equations 4.8 and 4.9 we obtain:

$$K_{11} = \frac{dP}{d\delta} = kR^2\pi \tag{4.18}$$

$$K_{22} = \frac{dM}{d\theta} = k\frac{R^4\pi}{4} \tag{4.19}$$

$$K_{12} = \frac{dP}{d\theta} = 0 \tag{4.20}$$

$$K_{21} = \frac{dM}{d\delta} = 0 \tag{4.21}$$

Therefore, the system is decoupled until partial lift-off occurs.

4.3.4 Linearization of Case II

From Equation 4.15 we get

$$\begin{aligned} dP &= k(R^2\bar{\phi} + \frac{2}{3}Rsin(\bar{\phi})\frac{\delta}{\theta})d\delta \\ &+ k(\frac{2}{3}R^3 sin\bar{\phi} - \frac{1}{3}Rsin\bar{\phi}\frac{\delta^2}{\theta^2})d\theta \\ &+ k(R^2\delta + \frac{2}{3}R^3\theta cos\bar{\phi} + \frac{1}{3}R\frac{\delta^2}{\theta}cos\bar{\phi})d\bar{\phi} \end{aligned} \tag{4.22}$$

From geometry we know $cos\bar{\phi} = -\frac{c}{R} = -\frac{\delta}{R\theta}$. Therefore, differentiation on both sides gives

$$-sin(\bar{\phi})d\bar{\phi} = -\frac{d\delta}{R\theta} + \frac{\delta d\theta}{R\theta^2} \tag{4.23}$$

Hence, $d\bar{\phi}$ can be written as:

$$d\bar{\phi} = \frac{1}{R\theta sin\bar{\phi}}d\delta - \frac{\delta}{R\theta^2 sin\bar{\phi}}d\theta \tag{4.24}$$

Back substituting Equation 4.24 into 4.22 results in

$$\begin{aligned} dP &= \underbrace{k(R^2\bar{\phi} + \frac{2}{3}R\,c\,sin\bar{\phi} + \frac{Rc}{sin\bar{\phi}} + \frac{2}{3}R^2 ctg\bar{\phi} + \frac{1}{3}c^2\,ctg\bar{\phi})}_{:=K_{11}}\,d\delta \\ &+ \underbrace{k(\frac{2}{3}R^3 sin\bar{\phi} - \frac{1}{3}Rc^2 sin\bar{\phi} - \frac{Rc^2}{sin\bar{\phi}} - \frac{2}{3}R^2\,c\,ctg\bar{\phi} - \frac{1}{3}c^3\,ctg\bar{\phi})}_{:=K_{12}}\,d\theta \end{aligned} \tag{4.25}$$

and by defining $\bar{c} := \frac{c}{R} = \frac{\delta}{R\theta}$, Equation 4.25 becomes

$$\begin{aligned} dP &= \underbrace{kR^2(\bar{\phi} + \frac{2}{3}\bar{c}\,sin\bar{\phi} + \frac{\bar{c}}{sin\bar{\phi}} + \frac{1}{3}(2+\bar{c}^2)ctg\bar{\phi})}_{K_{11}}\,d\delta \\ &+ \underbrace{kR^3(\frac{1}{3}(2-\bar{c}^2)sin\bar{\phi} - \frac{\bar{c}^2}{sin\bar{\phi}} - \frac{\bar{c}}{3}(2+\bar{c}^2)ctg\bar{\phi})}_{K_{12}}\,d\theta \end{aligned} \tag{4.26}$$

Similarly, from Equation 4.17 we get

$$
\begin{aligned}
dM &= k(\frac{2}{3}R^3 sin\bar{\phi} - \frac{1}{2}Rc^2 sin\bar{\phi})d\delta + k(\frac{R^4}{4}(\bar{\phi} + \frac{1}{2}sin(2\bar{\phi})) + \frac{1}{3}Rc^3 sin\bar{\phi})d\theta \\
&\quad + k(\frac{2}{3}R^3\delta\, cos\bar{\phi} + \frac{R^4\theta}{4}(1 + cos(2\bar{\phi})) - \frac{1}{6}Rc^2\delta cos\bar{\phi})d\bar{\phi} \\
&= \underbrace{kR^3(\frac{1}{6}(4 - 3\bar{c}^2)sin\bar{\phi} + \frac{2}{3}\bar{c}ctg\bar{\phi} + \frac{1}{4}\frac{1 + cos(2\bar{\phi})}{sin\bar{\phi}} - \frac{1}{6}\bar{c}^3 ctg\bar{\phi})}_{:= K_{21}}\, d\delta \\
&\quad + \underbrace{kR^4(\frac{1}{4}(\bar{\phi} + \frac{1}{2}sin(2\bar{\phi})) + \frac{1}{3}\bar{c}^3 sin\bar{\phi} - \frac{2}{3}\bar{c}^2 ctg\bar{\phi} - \frac{\bar{c}}{4}\frac{1 + cos(2\bar{\phi})}{sin\bar{\phi}} + \frac{1}{6}\bar{c}^4 ctg\bar{\phi})}_{:= K_{22}}\, d\theta
\end{aligned}
\tag{4.27}
$$

$$
\begin{aligned}
dM = &\underbrace{kR^3[\frac{1}{6}(4 - 3\bar{c}^2)sin\bar{\phi} + \frac{1}{4}\frac{1 + cos(2\bar{\phi})}{sin\bar{\phi}} + \frac{\bar{c}}{6}(4 - \bar{c}^2)ctg\bar{\phi}]}_{K_{21}}\, d\delta \\
&+ \underbrace{kR^4[\frac{1}{4}(\bar{\phi} + \frac{1}{2}sin2\bar{\phi}) + \frac{1}{3}\bar{c}^3 sin\bar{\phi} - \frac{\bar{c}}{4}\frac{1 + cos(2\bar{\phi})}{sin\bar{\phi}} - \frac{\bar{c}^2}{6}(4 - \bar{c}^2)ctg\bar{\phi}]}_{K_{22}}\, d\theta
\end{aligned}
\tag{4.28}
$$

In these equations, $\bar{c}$ is unitless, and $\bar{\phi} = cos^{-1}(-\bar{c}) \quad (for\ \ \bar{c} \leq 1)$. Letting $\widetilde{K}_{ij} := \frac{K_{ij}}{kR^{(i+j)}}$, then $\widetilde{K}_{ij}$ are independent of both the material properties and the size of the shaft (i.e., R). The variation of $\widetilde{K}_{ij}$ with $\bar{c}$ is shown in Figure 4.3. Note that when $\bar{c} \geq 1$, the shaft is fully in contact with underlain rock, and the rock has full stiffness (maximum values of $\widetilde{K}_{11}$ and $\widetilde{K}_{22}$) to resist rotation of the shaft toe. In this case, the problem falls in Case I. As the shaft is being pushed further, it will try to uplift, and a gap will form between its toe and rock ($\bar{c} < 1$), and will becomes a Case II problem. $\widetilde{K}_{11}$ and $\widetilde{K}_{22}$ will decrease while $\widetilde{K}_{12}$ and $\widetilde{K}_{21}$ increase. When $\bar{c} = -1$, the shaft toe is fully detached from rock and the rock provides no resistance to rotation.

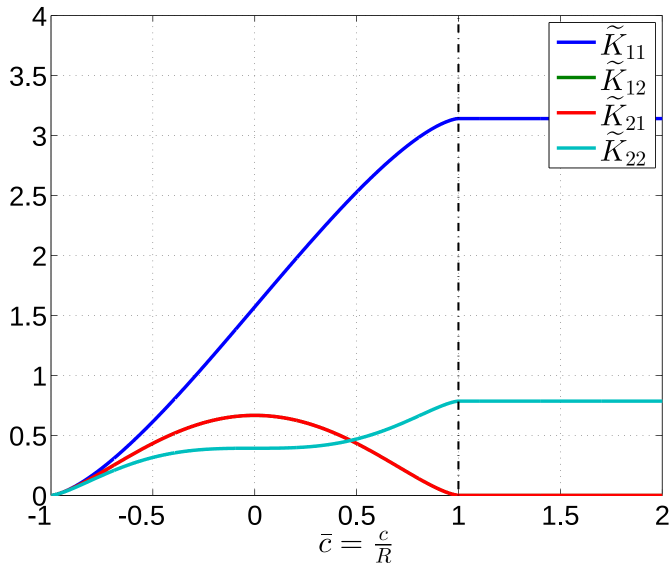

Figure 4.3 Evolution of stiffness with $\bar{c}$

4.4 3D PROBLEM

To extend the formulation to a full 3D case with rotations and displacements in any direction, the following projection operator is defined:

$$\underline{\widetilde{\theta}} = \theta_x \underline{e}_x + \theta_y \underline{e}_y = \underline{\underline{\mathbb{P}}}_z \underline{\theta} \qquad w/\underline{\underline{\mathbb{P}}}_z := \underline{\underline{\mathbf{1}}} - \underline{e}_z \otimes \underline{e}_z \tag{4.29}$$

where $\underline{\widetilde{\theta}}$ is the rotation vector defined with respect to the axis x and y that describe a plane with normal n (i.e., normal to the shaft cross section).

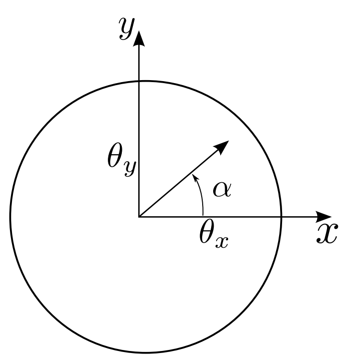

Figure 4.4 Schematic drawing for 3D Case.

From this definition the magnitude θ of the rotation vector is,

$$\theta = |\underline{\widetilde{\theta}}| = \sqrt{\theta_x^2 + \theta_y^2} \tag{4.30}$$

and the displacement δ is

$$\delta = \underline{u} \cdot \underline{n} \tag{4.31}$$

in which $\underline{u} \in \mathbb{R}^3, \underline{n} \in \mathbb{S}^2$ are perpendicular to the base. Differentiating,

$$d\delta = \underline{n} \cdot d\underline{u} \tag{4.32}$$

$$d\theta = \frac{\theta_x}{\theta} d\theta_x + \frac{\theta_y}{\theta} d\theta_y = cos\alpha\, d\theta_x + sin\alpha\, d\theta_y \tag{4.33}$$

$$d\underline{M} = dM_x \underline{e}_x + dM_y \underline{e}_y = dM\, cos\alpha\, \underline{e}_x + dM\, sin\alpha\, \underline{e}_y \tag{4.34}$$

$$\begin{aligned} dM_x &= dM cos\alpha \\ &= (K_{21}\, d\delta + K_{22}\, d\theta)\, cos\alpha \\ &= K_{21}\, cos\alpha\, \underline{n}\; \cdot d\underline{u} + K_{22}\, cos^2\alpha\, d\theta_x + K_{22}\, cos\alpha\, sin\alpha\, d\theta_y \end{aligned} \tag{4.35}$$

$$\begin{aligned} dM_y &= dM sin\alpha \\ &= (K_{21}\, d\delta + K_{22}\, d\theta)\, sin\alpha \\ &= K_{21}\, sin\alpha\, \underline{n} \cdot d\underline{u} + K_{22}\, sin\alpha\, cos\alpha\, d\theta_x + K_{22}\, sin^2\alpha\, d\theta_y \end{aligned} \tag{4.36}$$

$$\begin{aligned} dP &= K_{11}\, d\delta + K_{12}\, d\theta \\ &= K_{11}\, \underline{n} \cdot d\underline{u} + K_{12}\, cos\alpha\, d\theta_x + K_{12}\, sin\alpha\, d\theta_y \end{aligned} \tag{4.37}$$

$$\begin{aligned} d\underline{P} &= \underline{n}\, dP \\ &= \underbrace{K_{11}\, \underline{n} \otimes \underline{n}}_{\underline{\underline{K}}_{11}} \cdot d\underline{u} + \underbrace{(K_{12}\, cos\alpha\, \underline{n} \otimes \underline{e}_x + K_{12}\, sin\alpha\, \underline{n} \otimes \underline{e}_y)}_{\underline{\underline{K}}_{12}}\, d\underline{\theta} \end{aligned} \tag{4.38}$$

$$\begin{aligned} d\underline{M} &= dM_x\, \underline{e}_x + dM_y\, \underline{e}_y \\ &= \underbrace{(K_{21}\, cos\alpha\, \underline{e}_x \otimes \underline{n} + K_{21}\, sin\alpha\, \underline{e}_y \otimes \underline{n})}_{\underline{\underline{K}}_{21}} \cdot d\underline{u} \\ &= \underbrace{K_{22}(cos^2\alpha\, \underline{e}_x \otimes \underline{e}_x + cos\alpha\, sin\alpha\, \underline{e}_x \otimes \underline{e}_y + sin\alpha\, cos\alpha\, \underline{e}_y \otimes \underline{e}_x + sin^2\alpha\, \underline{e}_y \otimes \underline{e}_y)}_{\underline{\underline{K}}_{22}} \cdot d\theta \end{aligned} \tag{4.39}$$

$$\begin{Bmatrix} d\underline{P} \\ d\underline{M} \end{Bmatrix} = \begin{bmatrix} \underline{\underline{K}}_{11} & \underline{\underline{K}}_{12} \\ \underline{\underline{K}}_{21} & \underline{\underline{K}}_{22} \end{bmatrix} \begin{Bmatrix} d\underline{u} \\ d\underline{\theta} \end{Bmatrix} \tag{4.40}$$

where the stiffness coefficients $\underline{\underline{K}}_{ij}$ are a function of k, $\bar{\phi}$, R, $\bar{c}$, α, and the norm n. Considering all these parameters, k is the only material parameter. Evaluation of k can be done using numerical simulations.

4.5 FINDING THE RIGHT VALUE FOR *K*

The material parameter *k* represents the underlain rock's stiffness (subgrade reaction modulus) and can be obtained evaluating the deformation of a rigid plate (representing the shaft base) placed on the rock surface when subjected to an axial load P that induces vertical displacement δ (Figure 4.5), allowing for the calculaton of *k* as,

$$k = \frac{P}{a^2 \pi \delta} \tag{4.41}$$

Using material properties representing rock types I through V, it is possible to obtain appropriate stiffness values for k for each rock condition. Since the rock response is nonlinear, the resulting stiffness, k, is also nonlinear and varies with axial load; as the axial load increases, and the rock stresses reach the yield stress, the stiffness k reaches a peak value; see Figure 4.6). In this study peak, values were selected to represent k. For simplicity, in the numerical simulations presented herein instead of a rigid plate, a uniform load was applied to the rock surface. As a result, the rock deformation was not uniform, showing larger displacement near the center than around the edges (Figure 4.5), allowing for an upper bound, a lower bound, and average stiffness to be determined. The average values are used in the following models (Table 4.1).

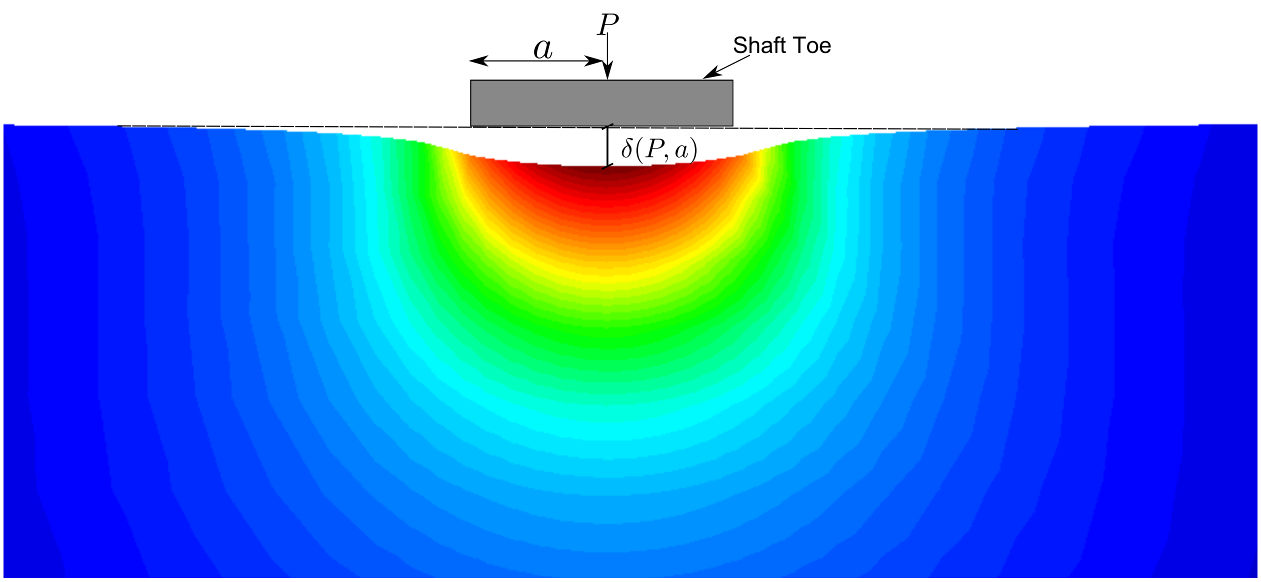

Figure 4.5 Deformation of rock under uniform load.

Table 4.1 Stiffness k used for modeling different toe conditions.

Rock Types	$k(MN/m^2/m)$
I	9.06E4
II	2.89E4
III	9.06E3
IV	2.89E3
V	9.06E2

As shown in Equations 4.18 through 4.21, the system is decoupled until partial lift-off occurs. This means the end shaft resistance element under Case I can be represented by two springs: one axial spring and one rotational spring (Figure 4.7), with stiffnesses equal to kA and kI (Table 4.1), respectively, where A is the cross-sectional area, and I is the second moment of area of shaft. Different embedment depths raging from 0.5 m to 1.5 m are considered; the results are shown in Tables 4.2 through 4.4 and Figures 4.8 through 4.10. As can be seen, rotational resistance from underlain rock may be beneficial in reducing shear demand. As the embedment increases, the benefit decreases. For the 1.5-m case, this effect is negligible because H_{eff} can only reach a certain depth, and the lateral deformation cannot be transferred to the toe as the embedment is large; see Chapter 2.

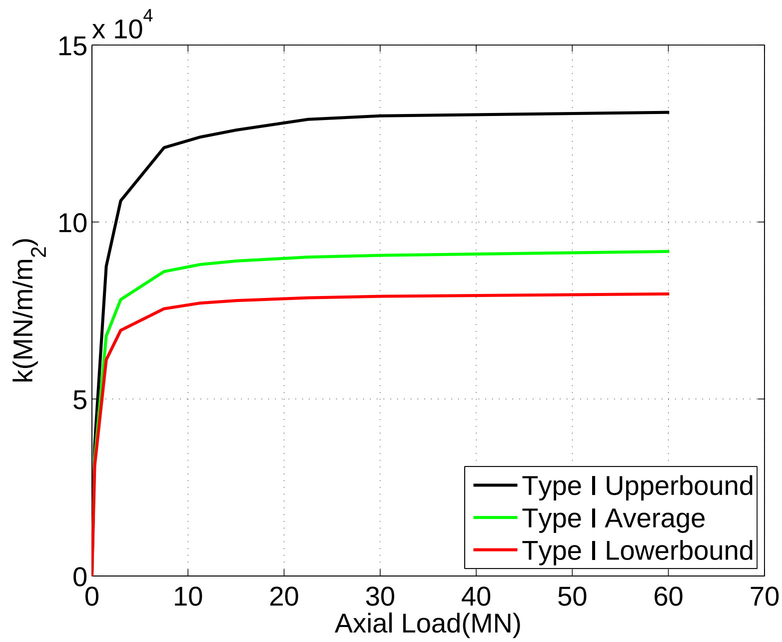

Figure 4.6 Calculated k for type I rock under different axial loads.

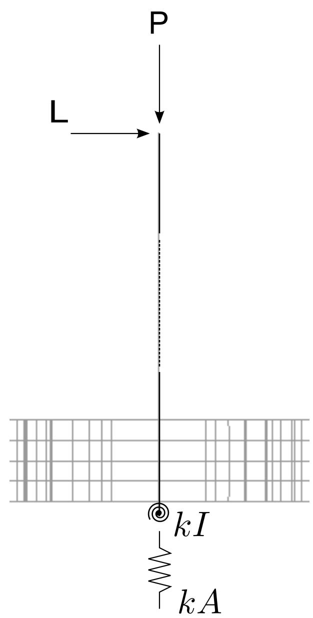

Figure 4.7 For case I, the end shaft resistance element is equivalent to two decoupled springs.

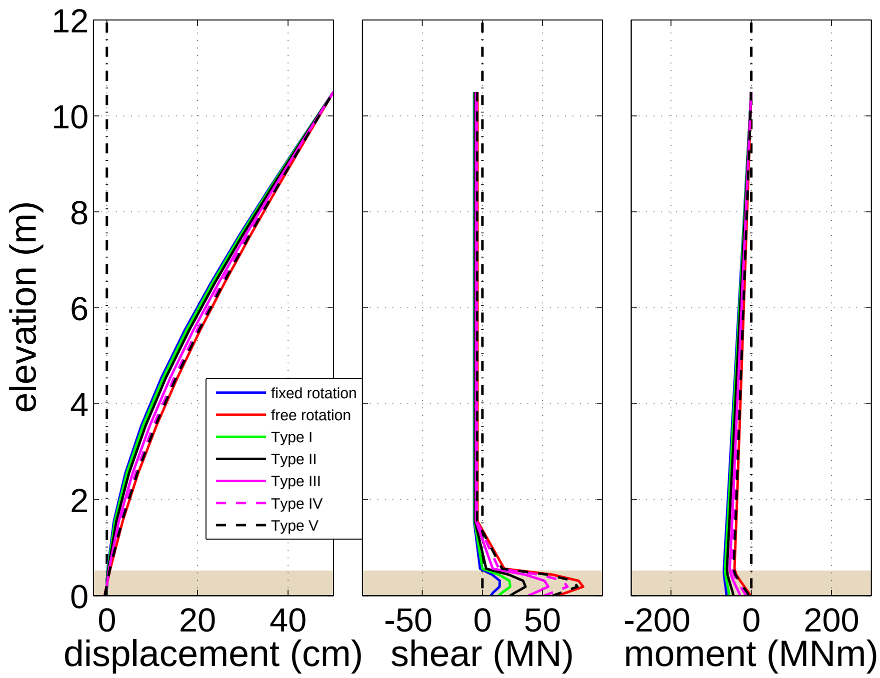

Figure 4.8 Shear demands in beam with different beam end fixities (thickness of rock = 0.5 m).

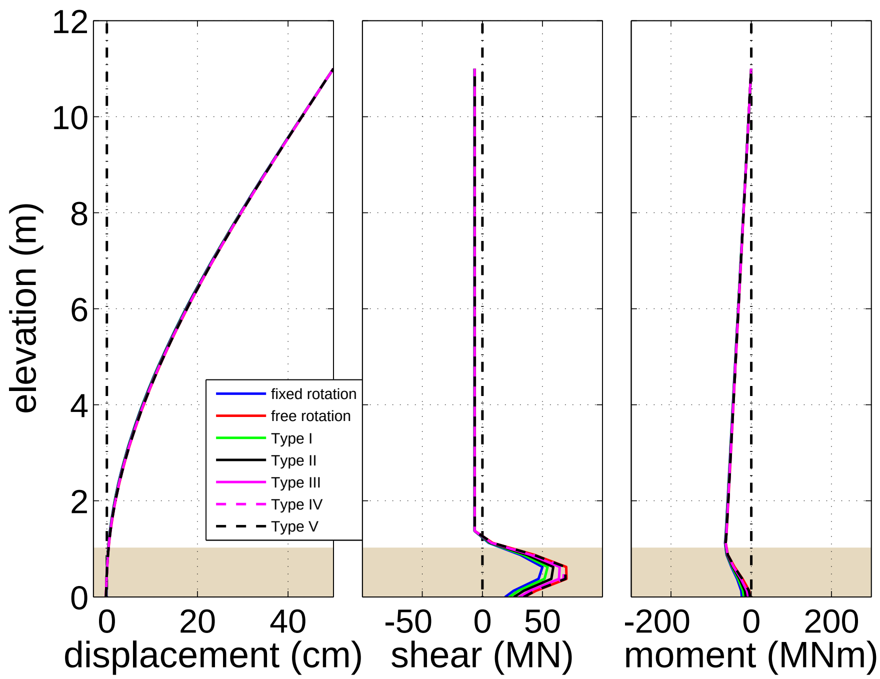

Figure 4.9 Shear demands in beam with different beam end fixities(thickness of rock = 1.0m).

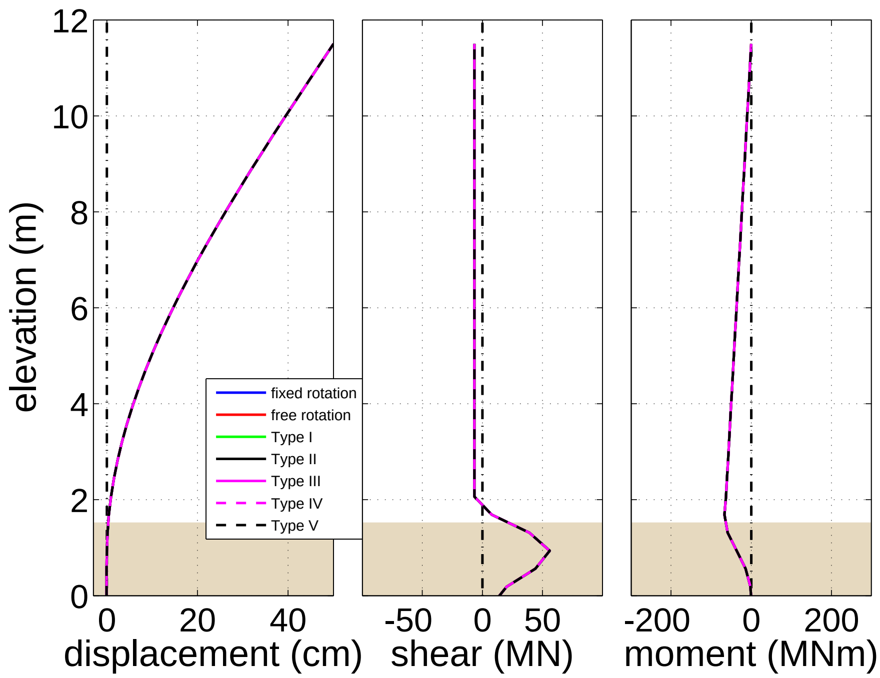

Figure 4.10 Shear demands in beam with different beam end fixities (thickness of rock = 1.5 m).

Table 4.2 Shear force summary for shaft with different types of rock beneath toe (0.5-m embedment).

	Shear Force at Top of Shaft (MN)	Maximum Shear Force (MN)	Shear Force Ratio
Fixed Rotation	6.83	15.50	2.12
Type I	6.52	23.24	3.56
Type II	6.06	35.89	5.92
Type III	5.32	54.88	10.32
Type IV	4.68	70.82	15.12
Type V	4.34	79.14	18.23
Free Rotation	4.15	83.85	20.21

Table 4.3 Shear force summary for shaft with different types of rock beneath toe (1.0-m embedment).

	Shear Force at Top of Shaft (MN)	Maximum Shear Force (MN)	Shear Force Ratio
Fixed Rotation	6.54	50.05	7.66
Type I	6.49	54.24	8.35
Type II	6.45	59.05	9.16
Type III	6.39	64.40	10.07
Type IV	6.36	67.65	10.64
Type V	6.35	69.18	10.90
Free Rotation	6.34	70.00	11.04

Table 4.4 Shear force summary for shaft with different types of rock beneath toe (1.5 -m embedment).

	Shear Force at Top of Shaft (MN)	Maximum Shear Force (MN)	Shear Force Ratio
Fixed Rotation	6.65	56.11	8.44
Type I	6.65	56.09	8.44
Type II	6.65	56.08	8.43
Type III	6.65	56.06	8.43
Type IV	6.65	56.05	8.43
Type V	6.65	56.04	8.43
Free Rotation	6.65	56.04	8.43

4.6 SUMMARY

1. The possibility of rotation depends on rock-socket depth and rock characteristics (in particular, the characteristics of the rock below the shaft toe). It is also affected by the magnitude of axial load and eccentricity.

2. The rotational stiffness is particularly beneficial when the socket depth is small; this benefit increases as the stiffness of the rock increases.

3. The stiffness k of rock can be estimated by applying vertical load onto rock. Judgment is needed in selecting the correct values.

4. The implemented one-node element has the potential to capture accurately the rotational constraint and uplift effect on shear demand.

5 Summary, Conclusions, and Recommendations for Future Work

This report presents an analytical and numerical study of drilled shafts socketed in rock and subjected to lateral loads.

5.1 SUMMARY AND CONCLUSIONS

A summary of the work and associated conclusions of this research is presented in terms of the following: comparison of different modeling strategies, parametric analysis of BNWF p-y-based models, and the end-shaft resistance model.

Modeling Rock Socketed Drilled Shafts

1. Although p-y based models predict larger shear demands, they are extremely simple to use.

2. Proper definition of p-y curves for rocks result in reasonable shear demands.

3. A comparison between results from p-y based models and 3D FE models shows the 3D FE models produced less magnitude of the shear force and bending moment demands in the shaft.

4. Beam elements properly capture shear demands.

5. Modeling the shaft with a plastic-fiber section may cause the shaft to yield after modest ductility. This limits the extent of shaft deflection at the rock interface, reducing the shear demand in the soil rock socket. The reduction depends on the section properties chosen.

6. Friction along the socket shaft tend to reduce shear demands, but as shown herein, it has little effect.

7. Solid elements representing the shaft produce accurate shear demands.

8. Plane sections do not seem to remain plane (i.e., the beam effect). This does result in smaller shear demands but based on the results presented, herein, this effect is small.

9. Rotation at the base of the shaft has an important effect on shear demand.

10. Eccentricity in axial loads provide a resisting bending moment that helps reduce the shear demands. This effect is more relevant as the axial load increases and h_{eff} increases. It may also be beneficial for small socket depths where shaft rotation may increase.

11. Possibility of rotation depends on rock-socket depth and rock characteristics and characteristics of the rock below the shaft toe. It is also affected by magnitude of axial load and eccentricity.

Parametric Study Using BNWF p-y Models and Comparison with 3D FEM Simulations

1. There are only minor differences between the results for the two sets of cohesionless soil p-y curves. For all cases, as the quality of the rock increases the contrast between the upper and lower layer shear force demands also increases. The shaft-head boundary condition changes the magnitude of the shear force and bending moment demands in the shaft, with the free-head condition inducing lower demands for an equal amount of lateral head displacement.

2. As the thickness of the rock layer is increased in comparison to the thickness of the soil layer,the ratio of the maximum shear force demands in each layer tends to decrease.

3. The shear force ratio is much lower when using the Liang et al. (2009) approach to develop rock p-y curves.

4. A comparison of results from BNWF analyses with the Timoshenko beam element formulation to the corresponding results for the Euler-Bernouli beam elements shows that the maximum shear force in the rock layer is reduced for the shear-deformable beam cases.

5. The ratios for the 3D cases with Drucker-Prager modeling approach are generally less than those for the BNWF analyses with the Reese rock p-y curves, and greater than those for the BNWF results using the Liang et al rock p-y curves, and the maxima for the Drucker-Prager results are generally greater than those for the $J2$ rock cases. The level of magnification depends more on the type of rock model used (Reese vs. Liang et al., $J2$ vs. Drucker-Prager) than on the type of analysis conducted (BNWF vs. 3D).

End Shaft Resistance Model

1. The possibility of rotation depends on rock-socket depth and rock characteristics and characteristics of the rock below the shaft toe. It is also affected by magnitude of axial load and eccentricity.

2. Rotational stiffness can be beneficial when the socket depth is small; this benefit increases as the stiffness of rock increases.

3. The stiffness k of rock can be estimated by applying vertical load onto rock. Judgment is needed to pick correct values.

4. The implemented one-node uplift element has the potential to capture the rotational constraint effect on the shear demand.

5.2 RECOMMENDATIONS FOR FUTURE WORK

1. The Drucker-Prager and $J2$ constitutive models used in the simulations are relatively simple models that do not necessarily represent true rock and soil behaviors. More advanced models are available to obtain a better representation of the rock response.

2. The implemented one-node uplift element need to be further developed to account for more complex cases, e.g., uplift induced detachment and 3D effects.

3. The evaluation of the rock stiffness k is simplified and needs further study. An experimental program to enhance the understanding of the behavior of rock at the shaft toe iis recommended.

4. This research focused on the analysis of a single shaft socketed in a soil and a rock profile in which there were only two layers and no slope wa assumed. More realistic scenarios should be studied to take advantage of the lessons learned in this project.

REFERENCES

American Petroleum Institute (API) (2007). *Recommended Practice for Planning, Designing and Constructing Fixed Offshore Platforms–Working Stress Design*. API Recommended Practice 2A-WSD (RP 2A-WSD), 21st edition. Errata and Supplement 3, October 2007.

Bieniawski, Z. T. (1989). *Engineering Rock Mass Classifications*. Balkema, Rotterdam, The Netherlands.

Boulanger, R. W., Kutter, B. L., Brandenberg, S. J., Singh, P., and Chang, D. (2003). *Pile Foundations in liquefied and laterally spreading ground during earthquakes: Centrifuge experiments and analyses*. Center for Geotechnical Modeling, University of California at Davis, Davis, CA. Rep. UCD/CGM-03/01.

Brinch Hansen, J. (1961). "The ultimate resistance of rigid piles against transversal forces." *Bulletin No. 12*, Geoteknisk Institute, Copenhagen, 5–9.

Dong, S. B., Alpdogan, C., and Taciroglu, E. (2010). "Much ado about shear correction factors in Timoshenko beam theory." *International Journal of Solids and Structures*, 47(13), 1651–1665.

Gabr, M. A., Borden, R. H., Cho, K. H., Clark, S., and Nixon, J. B. (2002). *p-y Curves for Laterally Loaded Drilled Shafts Embedded in Weathered Rock*. North Carolina State University, Raleigh. Report FHWA/NC/2002/08.

Hoek, E., Carranza-Torres, C., and Corkum, B. (2002). "Hoek-brown failure criterion – 2002 edition." *Proceedings, North American Rock Mechanics Society Meeting*, July 8-10, Toronto, ON, Canada.

Hoek, E., Kaiser, P. K., and Bawden, W. F. (1995). *Support of Underground Excavations in Hard Rock*. A.A. Balkema, Rotterdam, The Netherlands.

Kent, D. C. and Park, R. (1971). "Flexural members with confined concrete." *Journal of the Structural Mechanics Division, ASCE*, 97(ST7), 1969–1990.

Liang, R., Yang, K., and Nusairat, J. (2009). "p-y criterion for rock mass." *Journal of Geotechnical and Geoenvironmental Engineering, ASCE*, 135(1), 26–36.

LPILE™(2010). *A Program for the Analysis & Design of Piles and Drilled Shafts Under Lateral Loads*. `http://www.ensoftinc.com`. Ensoft, Inc. Engineering Software, Austin, Texas.

McGann, C. R. (2013). "Numerical evaluation of forces on piled bridge foundations in laterally spreading soil." phdthesis, Univsersity of Washington, Seattle.

McGann, C. R., Arduino, P., and Mackenzie-Helnwein, P. (2011). "Applicability of conventional p-y relations to the analysis of piles in laterally spreading soil." *Journal of Geotechnical and Geoenvironmental Engineering, ASCE*, 137(6), 557–567.

McGann, C. R., Arduino, P., and Mackenzie-Helnwein, P. (2012). “Development of simplified analysis procedure for piles in laterally spreading layered soils.” *PEER Report No. 2012/05*, Pacific Earthquake Engineering Research Center, University of California, Berkeley.

Petek, K. A. (2006). *Development and Application of Mixed Beam-Solid Models for Analysis of Soil-Pile Interaction Problems*. Ph.D. Dissertation, University of Washington.

Reese, L. C. (1997). “Analysis of laterally loaded piles in weak rock.” *Journal of Geotechnical and Geoenvironmental Engineering, ASCE*, 123(11), 1010–1017.

Reese, L. C. and Van Impe, W. F. (2001). *Single Piles and Pile Groups Under Lateral Loading*. A.A. Balkema, Rotterdam, Netherlands.

Serafim, J. L. and Pereira, J. P. (1983). “Considerations of the geomechanics classification of Bieniawski.” *Proceedings of the International Symposium on Engineering Geology and Underground Construction*, Lisbon, Portugal, 1133–1144.

Turner, J. (2006). *NCHRP Synthesis 360: Rock-Socketed Shafts for Highway Structure Foundations*. Transportation Research Board, National Academy Press, Washington, D.C.

PEER REPORTS

PEER reports are available as a free PDF download from https://peer.berkeley.edu/peer-reports. In addition, printed hard copies of PEER reports can be ordered directly from our printer by following the instructions at https://peer.berkeley.edu/peer-reports. For other related questions about the PEER Report Series, contact the Pacific Earthquake Engineering Research Center, 325 Davis Hall, Mail Code 1792, Berkeley, CA 94720. Tel.: (510) 642-3437; and Email: peer_center@berkeley.edu.

PEER 2018/05 *Selection of Random Vibration Procedures for the NGA-East Project*. Albert Kottke, Norman A. Abrahamson, David M. Boore, Yousef Bozorgnia. Christine Goulet, Justin Hollenback, Tadahiro Kishida, Armen Der Kiureghian, Olga-Joan Ktenidou, Nicolas Kuehn, Ellen M. Rathje, Walter J. Silva, Eric Thompson, and Xiaoyue Wang. November 2018.

PEER 2018/04 *Capturing Directivity Effects in the Mean and Aleatory Variability of the NGA-West 2 Ground Motion Prediction Equations.* Jennie A. Watson-Lamprey. November 2018.

PEER 2018/03 *Probabilistic Seismic Hazard Analysis Code Verification*. Christie Hale, Norman Abrahamson, and Yousef Bozorgnia. July 2018.

PEER 2018/02 *Update of the BCHydro Subduction Ground-Motion Model using the NGA-Subduction Dataset.* Norman Abrahamson, Nicolas Kuehn, Zeynep Gulerce, Nicholas Gregor, Yousef Bozorgnia, Grace Parker, Jonathan Stewart, Brian Chiou, I. M. Idriss, Kenneth Campbell, and Robert Youngs. June 2018.

PEER 2018/01 *PEER Annual Report 2017–2018*. Khalid Mosalam, Amarnath Kasalanati, and Selim Günay. June 2018.

PEER 2017/12 *Experimental Investigation of the Behavior of Vintage and Retrofit Concentrically Braced Steel Frames under Cyclic Loading*. Barbara G. Simpson, Stephen A. Mahin, and Jiun-Wei Lai, December 2017.

PEER 2017/11 *Preliminary Studies on the Dynamic Response of a Seismically Isolated Prototype Gen-IV Sodium-Cooled Fast Reactor* (*PGSFR*). Benshun Shao, Andreas H. Schellenberg, Matthew J. Schoettler, and Stephen A. Mahin. December 2017.

PEER 2017/10 *Development of Time Histories for IEEE693 Testing and Analysis (including Seismically Isolated Equipment).* Shakhzod M. Takhirov, Eric Fujisaki, Leon Kempner, Michael Riley, and Brian Low. December 2017.

PEER 2017/09 *“”R” Package for Computation of Earthquake Ground-Motion Response Spectra.* Pengfei Wang, Jonathan P. Stewart, Yousef Bozorgnia, David M. Boore, and Tadahiro Kishida. December 2017.

PEER 2017/08 *Influence of Kinematic SSI on Foundation Input Motions for Bridges on Deep Foundations*. Benjamin J. Turner, Scott J. Brandenberg, and Jonathan P. Stewart. November 2017.

PEER 2017/07 *A Nonlinear Kinetic Model for Multi-Stage Friction Pendulum Systems*. Paul L. Drazin and Sanjay Govindjee. September 2017.

PEER 2017/06 *Guidelines for Performance-Based Seismic Design of Tall Buildings, Version 2.02*. TBI Working Group led by co-chairs Ron Hamburger and Jack Moehle: Jack Baker, Jonathan Bray, C.B. Crouse, Greg Deierlein, John Hooper, Marshall Lew, Joe Maffei, Stephen Mahin, James Malley, Farzad Naeim, Jonathan Stewart, and John Wallace. May 2017.

PEER 2017/05 *Recommendations for Ergodic Nonlinear Site Amplification in Central and Eastern North America*. Youssef M.A. Hashash, Joseph A. Harmon, Okan Ilhan, Grace A. Parker, and Jonathan P. Stewart. March 2017.

PEER 2017/04 *Expert Panel Recommendations for Ergodic Site Amplification in Central and Eastern North America*. Jonathan P. Stewart, Grace A. Parker, Joseph P. Harmon, Gail M. Atkinson, David M. Boore, Robert B. Darragh, Walter J. Silva, and Youssef M.A. Hashash. March 2017.

PEER 2017/03 *NGA-East Ground-Motion Models for the U.S. Geological Survey National Seismic Hazard Maps*. Christine A. Goulet, Yousef Bozorgnia, Nicolas Kuehn, Linda Al Atik, Robert R. Youngs, Robert W. Graves, and Gail M. Atkinson. March 2017.

PEER 2017/02 *U.S.–New Zealand–Japan Workshop: Liquefaction-Induced Ground Movements Effects, University of California, Berkeley, California, 2–4 November 2016.* Jonathan D. Bray, Ross W. Boulanger, Misko Cubrinovski, Kohji Tokimatsu, Steven L. Kramer, Thomas O’Rourke, Ellen Rathje, Russell A. Green, Peter K. Robinson, and Christine Z. Beyzaei. March 2017.

PEER 2017/01 *2016 PEER Annual Report*. Khalid M. Mosalam, Amarnath Kasalanati, and Grace Kang. March 2017.

PEER 2016/10 *Performance-Based Robust Nonlinear Seismic Analysis with Application to Reinforced Concrete Bridge Systems*. Xiao Ling and Khalid M. Mosalam. December 2016.

PEER 2017/09 *Segmental Displacement Control Design for Seismically Isolated Bridges,* Kenneth A. Ogorzalek and Stephen A. Mahin. December 2016.

PEER 2016/08 *Resilience of Critical Structures, Infrastructure, and Communities*. Gian Paolo Cimellaro, Ali Zamani-Noori, Omar Kamouh, Vesna Terzic, and Stephen A. Mahin. December 2016.

PEER 2016/07 *Hybrid Simulation Theory for a Classical Nonlinear Dynamical System*. Paul L. Drazin and Sanjay Govindjee. September 2016.

PEER 2016/06 *California Earthquake Early Warning System Benefit Study*. Laurie A. Johnson, Sharyl Rabinovici, Grace S. Kang, and Stephen A. Mahin. July 2006.

PEER 2016/05 *Ground-Motion Prediction Equations for Arias Intensity Consistent with the NGA-West2 Ground-Motion Models.* Charlotte Abrahamson, Hao-Jun Michael Shi, and Brian Yang. July 2016.

PEER 2016/04 *The M_W 6.0 South Napa Earthquake of August 24, 2014: A Wake-Up Call for Renewed Investment in Seismic Resilience Across California.* Prepared for the California Seismic Safety Commission, Laurie A. Johnson and Stephen A. Mahin. May 2016.

PEER 2016/03 *Simulation Confidence in Tsunami-Driven Overland Flow.* Patrick Lynett. May 2016.

PEER 2016/02 *Semi-Automated Procedure for Windowing time Series and Computing Fourier Amplitude Spectra for the NGA-West2 Database*. Tadahiro Kishida, Olga-Joan Ktenidou, Robert B. Darragh, and Walter J. Silva. May 2016.

PEER 2016/01 *A Methodology for the Estimation of Kappa (κ) from Large Datasets: Example Application to Rock Sites in the NGA-East Database and Implications on Design Motions.* Olga-Joan Ktenidou, Norman A. Abrahamson, Robert B. Darragh, and Walter J. Silva. April 2016.

PEER 2015/13 *Self-Centering Precast Concrete Dual-Steel-Shell Columns for Accelerated Bridge Construction: Seismic Performance, Analysis, and Design*. Gabriele Guerrini, José I. Restrepo, Athanassios Vervelidis, and Milena Massari. December 2015.

PEER 2015/12 *Shear-Flexure Interaction Modeling for Reinforced Concrete Structural Walls and Columns under Reversed Cyclic Loading*. Kristijan Kolozvari, Kutay Orakcal, and John Wallace. December 2015.

PEER 2015/11 *Selection and Scaling of Ground Motions for Nonlinear Response History Analysis of Buildings in Performance-Based Earthquake Engineering*. N. Simon Kwong and Anil K. Chopra. December 2015.

PEER 2015/10 *Structural Behavior of Column-Bent Cap Beam-Box Girder Systems in Reinforced Concrete Bridges Subjected to Gravity and Seismic Loads. Part II: Hybrid Simulation and Post-Test Analysis*. Mohamed A. Moustafa and Khalid M. Mosalam. November 2015.

PEER 2015/09 *Structural Behavior of Column-Bent Cap Beam-Box Girder Systems in Reinforced Concrete Bridges Subjected to Gravity and Seismic Loads. Part I: Pre-Test Analysis and Quasi-Static Experiments*. Mohamed A. Moustafa and Khalid M. Mosalam. September 2015.

PEER 2015/08 *NGA-East: Adjustments to Median Ground-Motion Models for Center and Eastern North America*. August 2015.

PEER 2015/07 *NGA-East: Ground-Motion Standard-Deviation Models for Central and Eastern North America*. Linda Al Atik. June 2015.

PEER 2015/06 *Adjusting Ground-Motion Intensity Measures to a Reference Site for which V_{S30} = 3000 m/sec*. David M. Boore. May 2015.

PEER 2015/05 *Hybrid Simulation of Seismic Isolation Systems Applied to an APR-1400 Nuclear Power Plant.* Andreas H. Schellenberg, Alireza Sarebanha, Matthew J. Schoettler, Gilberto Mosqueda, Gianmario Benzoni, and Stephen A. Mahin. April 2015.

PEER 2015/04 *NGA-East: Median Ground-Motion Models for the Central and Eastern North America Region*. April 2015.

PEER 2015/03 *Single Series Solution for the Rectangular Fiber-Reinforced Elastomeric Isolator Compression Modulus*. James M. Kelly and Niel C. Van Engelen. March 2015.

PEER 2015/02 *A Full-Scale, Single-Column Bridge Bent Tested by Shake-Table Excitation.* Matthew J. Schoettler, José I. Restrepo, Gabriele Guerrini, David E. Duck, and Francesco Carrea. March 2015.

PEER 2015/01 *Concrete Column Blind Prediction Contest 2010: Outcomes and Observations.* Vesna Terzic, Matthew J. Schoettler, José I. Restrepo, and Stephen A Mahin. March 2015.

PEER 2014/20 *Stochastic Modeling and Simulation of Near-Fault Ground Motions for Performance-Based Earthquake Engineering*. Mayssa Dabaghi and Armen Der Kiureghian. December 2014.

PEER 2014/19 *Seismic Response of a Hybrid Fiber-Reinforced Concrete Bridge Column Detailed for Accelerated Bridge Construction*. Wilson Nguyen, William Trono, Marios Panagiotou, and Claudia P. Ostertag. December 2014.

PEER 2014/18 *Three-Dimensional Beam-Truss Model for Reinforced Concrete Walls and Slabs Subjected to Cyclic Static or Dynamic Loading*. Yuan Lu, Marios Panagiotou, and Ioannis Koutromanos. December 2014.

PEER 2014/17 *PEER NGA-East Database.* Christine A. Goulet, Tadahiro Kishida, Timothy D. Ancheta, Chris H. Cramer, Robert B. Darragh, Walter J. Silva, Youssef M.A. Hashash, Joseph Harmon, Jonathan P. Stewart, Katie E. Wooddell, and Robert R. Youngs. October 2014.

PEER 2014/16 *Guidelines for Performing Hazard-Consistent One-Dimensional Ground Response Analysis for Ground Motion Prediction*. Jonathan P. Stewart, Kioumars Afshari, and Youssef M.A. Hashash. October 2014.

PEER 2014/15 *NGA-East Regionalization Report: Comparison of Four Crustal Regions within Central and Eastern North America using Waveform Modeling and 5%-Damped Pseudo-Spectral Acceleration Response*. Jennifer Dreiling, Marius P. Isken, Walter D. Mooney, Martin C. Chapman, and Richard W. Godbee. October 2014.

PEER 2014/14 *Scaling Relations between Seismic Moment and Rupture Area of Earthquakes in Stable Continental Regions*. Paul Somerville. August 2014.

PEER 2014/13 *PEER Preliminary Notes and Observations on the August 24, 2014, South Napa Earthquake*. Grace S. Kang and Stephen A. Mahin, Editors. September 2014.

PEER 2014/12 *Reference-Rock Site Conditions for Central and Eastern North America: Part II – Attenuation (Kappa) Definition*. Kenneth W. Campbell, Youssef M.A. Hashash, Byungmin Kim, Albert R. Kottke, Ellen M. Rathje, Walter J. Silva, and Jonathan P. Stewart. August 2014.

PEER 2014/11 *Reference-Rock Site Conditions for Central and Eastern North America: Part I - Velocity Definition*. Youssef M.A. Hashash, Albert R. Kottke, Jonathan P. Stewart, Kenneth W. Campbell, Byungmin Kim, Ellen M. Rathje, Walter J. Silva, Sissy Nikolaou, and Cheryl Moss. August 2014.

PEER 2014/10 *Evaluation of Collapse and Non-Collapse of Parallel Bridges Affected by Liquefaction and Lateral Spreading*. Benjamin Turner, Scott J. Brandenberg, and Jonathan P. Stewart. August 2014.

PEER 2014/09 *PEER Arizona Strong-Motion Database and GMPEs Evaluation*. Tadahiro Kishida, Robert E. Kayen, Olga-Joan Ktenidou, Walter J. Silva, Robert B. Darragh, and Jennie Watson-Lamprey. June 2014.

PEER 2014/08 *Unbonded Pretensioned Bridge Columns with Rocking Detail*. Jeffrey A. Schaefer, Bryan Kennedy, Marc O. Eberhard, and John F. Stanton. June 2014.

PEER 2014/07 *Northridge 20 Symposium Summary Report: Impacts, Outcomes, and Next Steps*. May 2014.

PEER 2014/06 *Report of the Tenth Planning Meeting of NEES/E-Defense Collaborative Research on Earthquake Engineering*. December 2013.

PEER 2014/05 *Seismic Velocity Site Characterization of Thirty-One Chilean Seismometer Stations by Spectral Analysis of Surface Wave Dispersion*. Robert Kayen, Brad D. Carkin, Skye Corbet, Camilo Pinilla, Allan Ng, Edward Gorbis, and Christine Truong. April 2014.

PEER 2014/04 Effect of Vertical Acceleration on Shear Strength of Reinforced Concrete Columns. Hyerin Lee and Khalid M. Mosalam. April 2014.

PEER 2014/03 *Retest of Thirty-Year-Old Neoprene Isolation Bearings.* James M. Kelly and Niel C. Van Engelen. March 2014.

PEER 2014/02 *Theoretical Development of Hybrid Simulation Applied to Plate Structures.* Ahmed A. Bakhaty, Khalid M. Mosalam, and Sanjay Govindjee. January 2014.

PEER 2014/01 *Performance-Based Seismic Assessment of Skewed Bridges.* Peyman Kaviani, Farzin Zareian, and Ertugrul Taciroglu. January 2014.

PEER 2013/26 *Urban Earthquake Engineerin*g. Proceedings of the U.S.-Iran Seismic Workshop. December 2013.

PEER 2013/25 *Earthquake Engineering for Resilient Communities: 2013 PEER Internship Program Research Report Collection.* Heidi Tremayne (Editor), Stephen A. Mahin (Editor), Jorge Archbold Monterossa, Matt Brosman, Shelly Dean, Katherine deLaveaga, Curtis Fong, Donovan Holder, Rakeeb Khan, Elizabeth Jachens, David Lam, Daniela Martinez Lopez, Mara Minner, Geffen Oren, Julia Pavicic, Melissa Quinonez, Lorena Rodriguez, Sean Salazar, Kelli Slaven, Vivian Steyert, Jenny Taing, and Salvador Tena. December 2013.

PEER 2013/24 *NGA-West2 Ground Motion Prediction Equations for Vertical Ground Motions*. September 2013.

PEER 2013/23 *Coordinated Planning and Preparedness for Fire Following Major Earthquakes*. Charles Scawthorn. November 2013.

PEER 2013/22 *GEM-PEER Task 3 Project: Selection of a Global Set of Ground Motion Prediction Equations.* Jonathan P. Stewart, John Douglas, Mohammad B. Javanbarg, Carola Di Alessandro, Yousef Bozorgnia, Norman A. Abrahamson, David M. Boore, Kenneth W. Campbell, Elise Delavaud, Mustafa Erdik, and Peter J. Stafford. December 2013.

PEER 2013/21 *Seismic Design and Performance of Bridges with Columns on Rocking Foundations*. Grigorios Antonellis and Marios Panagiotou. September 2013.

PEER 2013/20 *Experimental and Analytical Studies on the Seismic Behavior of Conventional and Hybrid Braced Frames*. Jiun-Wei Lai and Stephen A. Mahin. September 2013.

PEER 2013/19 *Toward Resilient Communities: A Performance-Based Engineering Framework for Design and Evaluation of the Built Environment.* Michael William Mieler, Bozidar Stojadinovic, Robert J. Budnitz, Stephen A. Mahin, and Mary C. Comerio. September 2013.

PEER 2013/18 *Identification of Site Parameters that Improve Predictions of Site Amplification*. Ellen M. Rathje and Sara Navidi. July 2013.

PEER 2013/17 *Response Spectrum Analysis of Concrete Gravity Dams Including Dam-Water-Foundation Interaction*. Arnkjell Løkke and Anil K. Chopra. July 2013.

PEER 2013/16 *Effect of Hoop Reinforcement Spacing on the Cyclic Response of Large Reinforced Concrete Special Moment Frame Beams.* Marios Panagiotou, Tea Visnjic, Grigorios Antonellis, Panagiotis Galanis, and Jack P. Moehle. June 2013.

PEER 2013/15 *A Probabilistic Framework to Include the Effects of Near-Fault Directivity in Seismic Hazard Assessment*. Shrey Kumar Shahi, Jack W. Baker. October 2013.

PEER 2013/14 *Hanging-Wall Scaling using Finite-Fault Simulations.* Jennifer L. Donahue and Norman A. Abrahamson. September 2013.

PEER 2013/13 *Semi-Empirical Nonlinear Site Amplification and its Application in NEHRP Site Factors*. Jonathan P. Stewart and Emel Seyhan. November 2013.

PEER 2013/12 *Nonlinear Horizontal Site Response for the NGA-West2 Project.* Ronnie Kamai, Norman A. Abramson, Walter J. Silva. May 2013.

PEER 2013/11 *Epistemic Uncertainty for NGA-West2 Models.* Linda Al Atik and Robert R. Youngs. May 2013.

PEER 2013/10 *NGA-West 2 Models for Ground-Motion Directionality.* Shrey K. Shahi and Jack W. Baker. May 2013.

PEER 2013/09 *Final Report of the NGA-West2 Directivity Working Group.* Paul Spudich, Jeffrey R. Bayless, Jack W. Baker, Brian S.J. Chiou, Badie Rowshandel, Shrey Shahi, and Paul Somerville. May 2013.

PEER 2013/08 *NGA-West2 Model for Estimating Average Horizontal Values of Pseudo-Absolute Spectral Accelerations Generated by Crustal Earthquakes*. I. M. Idriss. May 2013.

PEER 2013/07 *Update of the Chiou and Youngs NGA Ground Motion Model for Average Horizontal Component of Peak Ground Motion and Response Spectra*. Brian Chiou and Robert Youngs. May 2013.

PEER 2013/06 *NGA-West2 Campbell-Bozorgnia Ground Motion Model for the Horizontal Components of PGA, PGV, and 5%-Damped Elastic Pseudo-Acceleration Response Spectra for Periods Ranging from 0.01 to 10 sec.* Kenneth W. Campbell and Yousef Bozorgnia. May 2013.

PEER 2013/05 *NGA-West 2 Equations for Predicting Response Spectral Accelerations for Shallow Crustal Earthquakes*. David M. Boore, Jonathan P. Stewart, Emel Seyhan, and Gail M. Atkinson. May 2013.

PEER 2013/04 *Update of the AS08 Ground-Motion Prediction Equations Based on the NGA-West2 Data Set*. Norman Abrahamson, Walter Silva, and Ronnie Kamai. May 2013.

PEER 2013/03 *PEER NGA-West2 Database.* Timothy D. Ancheta, Robert B. Darragh, Jonathan P. Stewart, Emel Seyhan, Walter J. Silva, Brian S.J. Chiou, Katie E. Wooddell, Robert W. Graves, Albert R. Kottke, David M. Boore, Tadahiro Kishida, and Jennifer L. Donahue. May 2013.

PEER 2013/02 *Hybrid Simulation of the Seismic Response of Squat Reinforced Concrete Shear Walls*. Catherine A. Whyte and Bozidar Stojadinovic. May 2013.

PEER 2013/01 *Housing Recovery in Chile: A Qualitative Mid-program Review*. Mary C. Comerio. February 2013.

PEER 2012/08 *Guidelines for Estimation of Shear Wave Velocity.* Bernard R. Wair, Jason T. DeJong, and Thomas Shantz. December 2012.

PEER 2012/07 *Earthquake Engineering for Resilient Communities: 2012 PEER Internship Program Research Report Collection.* Heidi Tremayne (Editor), Stephen A. Mahin (Editor), Collin Anderson, Dustin Cook, Michael Erceg, Carlos Esparza, Jose Jimenez, Dorian Krausz, Andrew Lo, Stephanie Lopez, Nicole McCurdy, Paul Shipman, Alexander Strum, Eduardo Vega. December 2012.

PEER 2012/06 *Fragilities for Precarious Rocks at Yucca Mountain.* Matthew D. Purvance, Rasool Anooshehpoor, and James N. Brune. December 2012.

PEER 2012/05 *Development of Simplified Analysis Procedure for Piles in Laterally Spreading Layered Soils.* Christopher R. McGann, Pedro Arduino, and Peter Mackenzie–Helnwein. December 2012.

PEER 2012/04 *Unbonded Pre-Tensioned Columns for Bridges in Seismic Regions.* Phillip M. Davis, Todd M. Janes, Marc O. Eberhard, and John F. Stanton. December 2012.

PEER 2012/03 *Experimental and Analytical Studies on Reinforced Concrete Buildings with Seismically Vulnerable Beam-Column Joints*. Sangjoon Park and Khalid M. Mosalam. October 2012.

PEER 2012/02 *Seismic Performance of Reinforced Concrete Bridges Allowed to Uplift during Multi-Directional Excitation*. Andres Oscar Espinoza and Stephen A. Mahin. July 2012.

PEER 2012/01 *Spectral Damping Scaling Factors for Shallow Crustal Earthquakes in Active Tectonic Regions.* Sanaz Rezaeian, Yousef Bozorgnia, I. M. Idriss, Kenneth Campbell, Norman Abrahamson, and Walter Silva. July 2012.

PEER 2011/10 *Earthquake Engineering for Resilient Communities: 2011 PEER Internship Program Research Report Collection*. Heidi Faison and Stephen A. Mahin, Editors. December 2011.

PEER 2011/09 *Calibration of Semi-Stochastic Procedure for Simulating High-Frequency Ground Motions*. Jonathan P. Stewart, Emel Seyhan, and Robert W. Graves. December 2011.

PEER 2011/08 *Water Supply in regard to Fire Following Earthquake*. Charles Scawthorn. November 2011.

PEER 2011/07 *Seismic Risk Management in Urban Areas*. Proceedings of a U.S.-Iran-Turkey Seismic Workshop. September 2011.

PEER 2011/06 *The Use of Base Isolation Systems to Achieve Complex Seismic Performance Objectives*. Troy A. Morgan and Stephen A. Mahin. July 2011.

PEER 2011/05 *Case Studies of the Seismic Performance of Tall Buildings Designed by Alternative Means.* Task 12 Report for the Tall Buildings Initiative. Jack Moehle, Yousef Bozorgnia, Nirmal Jayaram, Pierson Jones, Mohsen Rahnama, Nilesh Shome, Zeynep Tuna, John Wallace, Tony Yang, and Farzin Zareian. July 2011.

PEER 2011/04 *Recommended Design Practice for Pile Foundations in Laterally Spreading Ground.* Scott A. Ashford, Ross W. Boulanger, and Scott J. Brandenberg. June 2011.

PEER 2011/03 *New Ground Motion Selection Procedures and Selected Motions for the PEER Transportation Research Program*. Jack W. Baker, Ting Lin, Shrey K. Shahi, and Nirmal Jayaram. March 2011.

PEER 2011/02 *A Bayesian Network Methodology for Infrastructure Seismic Risk Assessment and Decision Support*. Michelle T. Bensi, Armen Der Kiureghian, and Daniel Straub. March 2011.

PEER 2011/01 *Demand Fragility Surfaces for Bridges in Liquefied and Laterally Spreading Ground.* Scott J. Brandenberg, Jian Zhang, Pirooz Kashighandi, Yili Huo, and Minxing Zhao. March 2011.

PEER 2010/05 *Guidelines for Performance-Based Seismic Design of Tall Buildings.* Developed by the Tall Buildings Initiative. November 2010.

PEER 2010/04 *Application Guide for the Design of Flexible and Rigid Bus Connections between Substation Equipment Subjected to Earthquakes.* Jean-Bernard Dastous and Armen Der Kiureghian. September 2010.

PEER 2010/03 *Shear Wave Velocity as a Statistical Function of Standard Penetration Test Resistance and Vertical Effective Stress at Caltrans Bridge Sites.* Scott J. Brandenberg, Naresh Bellana, and Thomas Shantz. June 2010.

PEER 2010/02 *Stochastic Modeling and Simulation of Ground Motions for Performance-Based Earthquake Engineering.* Sanaz Rezaeian and Armen Der Kiureghian. June 2010.

PEER 2010/01 *Structural Response and Cost Characterization of Bridge Construction Using Seismic Performance Enhancement Strategies.* Ady Aviram, Božidar Stojadinović, Gustavo J. Parra-Montesinos, and Kevin R. Mackie. March 2010.

PEER 2009/03 *The Integration of Experimental and Simulation Data in the Study of Reinforced Concrete Bridge Systems Including Soil-Foundation-Structure Interaction.* Matthew Dryden and Gregory L. Fenves. November 2009.

PEER 2009/02 *Improving Earthquake Mitigation through Innovations and Applications in Seismic Science, Engineering, Communication, and Response*. Proceedings of a U.S.-Iran Seismic Workshop. October 2009.

PEER 2009/01 *Evaluation of Ground Motion Selection and Modification Methods: Predicting Median Interstory Drift Response of Buildings*. Curt B. Haselton, Editor. June 2009.

PEER 2008/10 *Technical Manual for Strata.* Albert R. Kottke and Ellen M. Rathje. February 2009.

PEER 2008/09 *NGA Model for Average Horizontal Component of Peak Ground Motion and Response Spectra.* Brian S.-J. Chiou and Robert R. Youngs. November 2008.

PEER 2008/08 *Toward Earthquake-Resistant Design of Concentrically Braced Steel Structures*. Patxi Uriz and Stephen A. Mahin. November 2008.

PEER 2008/07 *Using OpenSees for Performance-Based Evaluation of Bridges on Liquefiable Soils*. Stephen L. Kramer, Pedro Arduino, and HyungSuk Shin. November 2008.

PEER 2008/06 *Shaking Table Tests and Numerical Investigation of Self-Centering Reinforced Concrete Bridge Columns*. Hyung IL Jeong, Junichi Sakai, and Stephen A. Mahin. September 2008.

PEER 2008/05 *Performance-Based Earthquake Engineering Design Evaluation Procedure for Bridge Foundations Undergoing Liquefaction-Induced Lateral Ground Displacement*. Christian A. Ledezma and Jonathan D. Bray. August 2008.

PEER 2008/04 *Benchmarking of Nonlinear Geotechnical Ground Response Analysis Procedures.* Jonathan P. Stewart, Annie On-Lei Kwok, Youssef M. A. Hashash, Neven Matasovic, Robert Pyke, Zhiliang Wang, and Zhaohui Yang. August 2008.

PEER 2008/03 *Guidelines for Nonlinear Analysis of Bridge Structures in California.* Ady Aviram, Kevin R. Mackie, and Božidar Stojadinović. August 2008.

PEER 2008/02 *Treatment of Uncertainties in Seismic-Risk Analysis of Transportation Systems*. Evangelos Stergiou and Anne S. Kiremidjian. July 2008.

PEER 2008/01 *Seismic Performance Objectives for Tall Buildings.* William T. Holmes, Charles Kircher, William Petak, and Nabih Youssef. August 2008.

PEER 2007/12 *An Assessment to Benchmark the Seismic Performance of a Code-Conforming Reinforced Concrete Moment-Frame Building.* Curt Haselton, Christine A. Goulet, Judith Mitrani-Reiser, James L. Beck, Gregory G. Deierlein, Keith A. Porter, Jonathan P. Stewart, and Ertugrul Taciroglu. August 2008.

PEER 2007/11 *Bar Buckling in Reinforced Concrete Bridge Columns.* Wayne A. Brown, Dawn E. Lehman, and John F. Stanton. February 2008.

PEER 2007/10 *Computational Modeling of Progressive Collapse in Reinforced Concrete Frame Structures*. Mohamed M. Talaat and Khalid M. Mosalam. May 2008.

PEER 2007/09 *Integrated Probabilistic Performance-Based Evaluation of Benchmark Reinforced Concrete Bridges*. Kevin R. Mackie, John-Michael Wong, and Božidar Stojadinović. January 2008.

PEER 2007/08 *Assessing Seismic Collapse Safety of Modern Reinforced Concrete Moment-Frame Buildings*. Curt B. Haselton and Gregory G. Deierlein. February 2008.

PEER 2007/07 *Performance Modeling Strategies for Modern Reinforced Concrete Bridge Columns*. Michael P. Berry and Marc O. Eberhard. April 2008.

PEER 2007/06 *Development of Improved Procedures for Seismic Design of Buried and Partially Buried Structures*. Linda Al Atik and Nicholas Sitar. June 2007.

PEER 2007/05 *Uncertainty and Correlation in Seismic Risk Assessment of Transportation Systems*. Renee G. Lee and Anne S. Kiremidjian. July 2007.

PEER 2007/04 *Numerical Models for Analysis and Performance-Based Design of Shallow Foundations Subjected to Seismic Loading.* Sivapalan Gajan, Tara C. Hutchinson, Bruce L. Kutter, Prishati Raychowdhury, José A. Ugalde, and Jonathan P. Stewart. May 2008.

PEER 2007/03 *Beam-Column Element Model Calibrated for Predicting Flexural Response Leading to Global Collapse of RC Frame Buildings*. Curt B. Haselton, Abbie B. Liel, Sarah Taylor Lange, and Gregory G. Deierlein. May 2008.

PEER 2007/02 *Campbell-Bozorgnia NGA Ground Motion Relations for the Geometric Mean Horizontal Component of Peak and Spectral Ground Motion Parameters*. Kenneth W. Campbell and Yousef Bozorgnia. May 2007.

PEER 2007/01 *Boore-Atkinson NGA Ground Motion Relations for the Geometric Mean Horizontal Component of Peak and Spectral Ground Motion Parameters*. David M. Boore and Gail M. Atkinson. May 2007.

PEER 2006/12 Societal Implications of Performance-Based Earthquake Engineering. Peter J. May. May 2007.

PEER 2006/11 *Probabilistic Seismic Demand Analysis Using Advanced Ground Motion Intensity Measures, Attenuation Relationships, and Near-Fault Effects*. Polsak Tothong and C. Allin Cornell. March 2007.

PEER 2006/10 *Application of the PEER PBEE Methodology to the I-880 Viaduct*. Sashi Kunnath. February 2007.

PEER 2006/09 *Quantifying Economic Losses from Travel Forgone Following a Large Metropolitan Earthquake*. James Moore, Sungbin Cho, Yue Yue Fan, and Stuart Werner. November 2006.

PEER 2006/08 *Vector-Valued Ground Motion Intensity Measures for Probabilistic Seismic Demand Analysis*. Jack W. Baker and C. Allin Cornell. October 2006.

PEER 2006/07 *Analytical Modeling of Reinforced Concrete Walls for Predicting Flexural and Coupled–Shear-Flexural Responses*. Kutay Orakcal, Leonardo M. Massone, and John W. Wallace. October 2006.

PEER 2006/06 *Nonlinear Analysis of a Soil-Drilled Pier System under Static and Dynamic Axial Loading*. Gang Wang and Nicholas Sitar. November 2006.

PEER 2006/05 *Advanced Seismic Assessment Guidelines.* Paolo Bazzurro, C. Allin Cornell, Charles Menun, Maziar Motahari, and Nicolas Luco. September 2006.

PEER 2006/04 *Probabilistic Seismic Evaluation of Reinforced Concrete Structural Components and Systems*. Tae Hyung Lee and Khalid M. Mosalam. August 2006.

PEER 2006/03 *Performance of Lifelines Subjected to Lateral Spreading.* Scott A. Ashford and Teerawut Juirnarongrit. July 2006.

PEER 2006/02 *Pacific Earthquake Engineering Research Center Highway Demonstration Project.* Anne Kiremidjian, James Moore, Yue Yue Fan, Nesrin Basoz, Ozgur Yazali, and Meredith Williams. April 2006.

PEER 2006/01 *Bracing Berkeley. A Guide to Seismic Safety on the UC Berkeley Campus.* Mary C. Comerio, Stephen Tobriner, and Ariane Fehrenkamp. January 2006.

PEER 2005/17 *Earthquake Simulation Tests on Reducing Residual Displacements of Reinforced Concrete Bridges.* Junichi Sakai, Stephen A Mahin, and Andres Espinoza. December 2005.

PEER 2005/16 *Seismic Response and Reliability of Electrical Substation Equipment and Systems.* Junho Song, Armen Der Kiureghian, and Jerome L. Sackman. April 2006.

PEER 2005/15 *CPT-Based Probabilistic Assessment of Seismic Soil Liquefaction Initiation.* R. E. S. Moss, R. B. Seed, R. E. Kayen, J. P. Stewart, and A. Der Kiureghian. April 2006.

PEER 2005/14 *Workshop on Modeling of Nonlinear Cyclic Load-Deformation Behavior of Shallow Foundations.* Bruce L. Kutter, Geoffrey Martin, Tara Hutchinson, Chad Harden, Sivapalan Gajan, and Justin Phalen. March 2006.

PEER 2005/13 *Stochastic Characterization and Decision Bases under Time-Dependent Aftershock Risk in Performance-Based Earthquake Engineering*. Gee Liek Yeo and C. Allin Cornell. July 2005.

PEER 2005/12 *PEER Testbed Study on a Laboratory Building: Exercising Seismic Performance Assessment.* Mary C. Comerio, Editor. November 2005.

PEER 2005/11 *Van Nuys Hotel Building Testbed Report: Exercising Seismic Performance Assessment.* Helmut Krawinkler, Editor. October 2005.

PEER 2005/10 *First NEES/E-Defense Workshop on Collapse Simulation of Reinforced Concrete Building Structures.* September 2005.

PEER 2005/09 *Test Applications of Advanced Seismic Assessment Guidelines.* Joe Maffei, Karl Telleen, Danya Mohr, William Holmes, and Yuki Nakayama. August 2006.

PEER 2005/08 *Damage Accumulation in Lightly Confined Reinforced Concrete Bridge Columns.* R. Tyler Ranf, Jared M. Nelson, Zach Price, Marc O. Eberhard, and John F. Stanton. April 2006.

PEER 2005/07 *Experimental and Analytical Studies on the Seismic Response of Freestanding and Anchored Laboratory Equipment.* Dimitrios Konstantinidis and Nicos Makris. January 2005.

PEER 2005/06 *Global Collapse of Frame Structures under Seismic Excitations*. Luis F. Ibarra and Helmut Krawinkler. September 2005.

PEER 2005//05 *Performance Characterization of Bench- and Shelf-Mounted Equipment.* Samit Ray Chaudhuri and Tara C. Hutchinson. May 2006.

PEER 2005/04 *Numerical Modeling of the Nonlinear Cyclic Response of Shallow Foundations.* Chad Harden, Tara Hutchinson, Geoffrey R. Martin, and Bruce L. Kutter. August 2005.

PEER 2005/03 *A Taxonomy of Building Components for Performance-Based Earthquake Engineering.* Keith A. Porter. September 2005.

PEER 2005/02 *Fragility Basis for California Highway Overpass Bridge Seismic Decision Making*. Kevin R. Mackie and Božidar Stojadinović. June 2005.

PEER 2005/01 *Empirical Characterization of Site Conditions on Strong Ground Motion.* Jonathan P. Stewart, Yoojoong Choi, and Robert W. Graves. June 2005.

PEER 2004/09 *Electrical Substation Equipment Interaction: Experimental Rigid Conductor Studies.* Christopher Stearns and André Filiatrault. February 2005.

PEER 2004/08 *Seismic Qualification and Fragility Testing of Line Break 550-kV Disconnect Switches.* Shakhzod M. Takhirov, Gregory L. Fenves, and Eric Fujisaki. January 2005.

PEER 2004/07 *Ground Motions for Earthquake Simulator Qualification of Electrical Substation Equipment.* Shakhzod M. Takhirov, Gregory L. Fenves, Eric Fujisaki, and Don Clyde. January 2005.

PEER 2004/06 *Performance-Based Regulation and Regulatory Regimes.* Peter J. May and Chris Koski. September 2004.

PEER 2004/05 *Performance-Based Seismic Design Concepts and Implementation: Proceedings of an International Workshop.* Peter Fajfar and Helmut Krawinkler, Editors. September 2004.

PEER 2004/04 *Seismic Performance of an Instrumented Tilt-up Wall Building.* James C. Anderson and Vitelmo V. Bertero. July 2004.

PEER 2004/03 *Evaluation and Application of Concrete Tilt-up Assessment Methodologies.* Timothy Graf and James O. Malley. October 2004.

PEER 2004/02 *Analytical Investigations of New Methods for Reducing Residual Displacements of Reinforced Concrete Bridge Columns.* Junichi Sakai and Stephen A. Mahin. August 2004.

PEER 2004/01 *Seismic Performance of Masonry Buildings and Design Implications.* Kerri Anne Taeko Tokoro, James C. Anderson, and Vitelmo V. Bertero. February 2004.

PEER 2003/18 *Performance Models for Flexural Damage in Reinforced Concrete Columns.* Michael Berry and Marc Eberhard. August 2003.

PEER 2003/17 *Predicting Earthquake Damage in Older Reinforced Concrete Beam-Column Joints.* Catherine Pagni and Laura Lowes. October 2004.

PEER 2003/16 *Seismic Demands for Performance-Based Design of Bridges.* Kevin Mackie and Božidar Stojadinović. August 2003.

PEER 2003/15 *Seismic Demands for Nondeteriorating Frame Structures and Their Dependence on Ground Motions.* Ricardo Antonio Medina and Helmut Krawinkler. May 2004.

PEER 2003/14 *Finite Element Reliability and Sensitivity Methods for Performance-Based Earthquake Engineering*. Terje Haukaas and Armen Der Kiureghian. April 2004.

PEER 2003/13 *Effects of Connection Hysteretic Degradation on the Seismic Behavior of Steel Moment-Resisting Frames.* Janise E. Rodgers and Stephen A. Mahin. March 2004.

PEER 2003/12 *Implementation Manual for the Seismic Protection of Laboratory Contents: Format and Case Studies*. William T. Holmes and Mary C. Comerio. October 2003.

PEER 2003/11 *Fifth U.S.-Japan Workshop on Performance-Based Earthquake Engineering Methodology for Reinforced Concrete Building Structures*. February 2004.

PEER 2003/10 *A Beam-Column Joint Model for Simulating the Earthquake Response of Reinforced Concrete Frames.* Laura N. Lowes, Nilanjan Mitra, and Arash Altoontash. February 2004.

PEER 2003/09 *Sequencing Repairs after an Earthquake: An Economic Approach.* Marco Casari and Simon J. Wilkie. April 2004.

PEER 2003/08 *A Technical Framework for Probability-Based Demand and Capacity Factor Design (DCFD) Seismic Formats.* Fatemeh Jalayer and C. Allin Cornell. November 2003.

PEER 2003/07 *Uncertainty Specification and Propagation for Loss Estimation Using FOSM Methods.* Jack W. Baker and C. Allin Cornell. September 2003.

PEER 2003/06 *Performance of Circular Reinforced Concrete Bridge Columns under Bidirectional Earthquake Loading*. Mahmoud M. Hachem, Stephen A. Mahin, and Jack P. Moehle. February 2003.

PEER 2003/05 *Response Assessment for Building-Specific Loss Estimation.* Eduardo Miranda and Shahram Taghavi. September 2003.

PEER 2003/04 *Experimental Assessment of Columns with Short Lap Splices Subjected to Cyclic Loads*. Murat Melek, John W. Wallace, and Joel Conte. April 2003.

PEER 2003/03 *Probabilistic Response Assessment for Building-Specific Loss Estimation*. Eduardo Miranda and Hesameddin Aslani. September 2003.

PEER 2003/02 *Software Framework for Collaborative Development of Nonlinear Dynamic Analysis Program*. Jun Peng and Kincho H. Law. September 2003.

PEER 2003/01 *Shake Table Tests and Analytical Studies on the Gravity Load Collapse of Reinforced Concrete Frames.* Kenneth John Elwood and Jack P. Moehle. November 2003.

PEER 2002/24 *Performance of Beam to Column Bridge Joints Subjected to a Large Velocity Pulse.* Natalie Gibson, André Filiatrault, and Scott A. Ashford. April 2002.

PEER 2002/23 *Effects of Large Velocity Pulses on Reinforced Concrete Bridge Columns.* Greg L. Orozco and Scott A. Ashford. April 2002.

PEER 2002/22 *Characterization of Large Velocity Pulses for Laboratory Testing.* Kenneth E. Cox and Scott A. Ashford. April 2002.

PEER 2002/21 *Fourth U.S.-Japan Workshop on Performance-Based Earthquake Engineering Methodology for Reinforced Concrete Building Structures*. December 2002.

PEER 2002/20 *Barriers to Adoption and Implementation of PBEE Innovations.* Peter J. May. August 2002.

PEER 2002/19 *Economic-Engineered Integrated Models for Earthquakes: Socioeconomic Impacts.* Peter Gordon, James E. Moore II, and Harry W. Richardson. July 2002.

PEER 2002/18 *Assessment of Reinforced Concrete Building Exterior Joints with Substandard Details.* Chris P. Pantelides, Jon Hansen, Justin Nadauld, and Lawrence D. Reaveley. May 2002.

PEER 2002/17 *Structural Characterization and Seismic Response Analysis of a Highway Overcrossing Equipped with Elastomeric Bearings and Fluid Dampers: A Case Study*. Nicos Makris and Jian Zhang. November 2002.

PEER 2002/16 *Estimation of Uncertainty in Geotechnical Properties for Performance-Based Earthquake Engineering*. Allen L. Jones, Steven L. Kramer, and Pedro Arduino. December 2002.

PEER 2002/15 *Seismic Behavior of Bridge Columns Subjected to Various Loading Patterns*. Asadollah Esmaeily-Gh. and Yan Xiao. December 2002.

PEER 2002/14 *Inelastic Seismic Response of Extended Pile Shaft Supported Bridge Structures.* T.C. Hutchinson, R.W. Boulanger, Y.H. Chai, and I.M. Idriss. December 2002.

PEER 2002/13 *Probabilistic Models and Fragility Estimates for Bridge Components and Systems.* Paolo Gardoni, Armen Der Kiureghian, and Khalid M. Mosalam. June 2002.

PEER 2002/12 *Effects of Fault Dip and Slip Rake on Near-Source Ground Motions: Why Chi-Chi Was a Relatively Mild M7.6 Earthquake*. Brad T. Aagaard, John F. Hall, and Thomas H. Heaton. December 2002.

PEER 2002/11 *Analytical and Experimental Study of Fiber-Reinforced Strip Isolators*. James M. Kelly and Shakhzod M. Takhirov. September 2002.

PEER 2002/10 *Centrifuge Modeling of Settlement and Lateral Spreading with Comparisons to Numerical Analyses***.** Sivapalan Gajan and Bruce L. Kutter. January 2003.

PEER 2002/09 *Documentation and Analysis of Field Case Histories of Seismic Compression during the 1994 Northridge, California, Earthquake*. Jonathan P. Stewart, Patrick M. Smith, Daniel H. Whang, and Jonathan D. Bray. October 2002.

PEER 2002/08 *Component Testing, Stability Analysis and Characterization of Buckling-Restrained Unbonded Braces™*. Cameron Black, Nicos Makris, and Ian Aiken. September 2002.

PEER 2002/07 *Seismic Performance of Pile-Wharf Connections.* Charles W. Roeder, Robert Graff, Jennifer Soderstrom, and Jun Han Yoo. December 2001.

PEER 2002/06 *The Use of Benefit-Cost Analysis for Evaluation of Performance-Based Earthquake Engineering Decisions*. Richard O. Zerbe and Anthony Falit-Baiamonte. September 2001.

PEER 2002/05 *Guidelines, Specifications, and Seismic Performance Characterization of Nonstructural Building Components and Equipment*. André Filiatrault, Constantin Christopoulos, and Christopher Stearns. September 2001.

PEER 2002/04 *Consortium of Organizations for Strong-Motion Observation Systems and the Pacific Earthquake Engineering Research Center Lifelines Program: Invited Workshop on Archiving and Web Dissemination of Geotechnical Data, 4–5 October 2001*. September 2002.

PEER 2002/03 *Investigation of Sensitivity of Building Loss Estimates to Major Uncertain Variables for the Van Nuys Testbed*. Keith A. Porter, James L. Beck, and Rustem V. Shaikhutdinov. August 2002.

PEER 2002/02 *The Third U.S.-Japan Workshop on Performance-Based Earthquake Engineering Methodology for Reinforced Concrete Building Structures*. July 2002.

PEER 2002/01 *Nonstructural Loss Estimation: The UC Berkeley Case Study.* Mary C. Comerio and John C. Stallmeyer. December 2001.

PEER 2001/16 *Statistics of SDF-System Estimate of Roof Displacement for Pushover Analysis of Buildings.* Anil K. Chopra, Rakesh K. Goel, and Chatpan Chintanapakdee. December 2001.

PEER 2001/15 *Damage to Bridges during the 2001 Nisqually Earthquake.* R. Tyler Ranf, Marc O. Eberhard, and Michael P. Berry. November 2001.

PEER 2001/14 *Rocking Response of Equipment Anchored to a Base Foundation.* Nicos Makris and Cameron J. Black. September 2001.

PEER 2001/13 *Modeling Soil Liquefaction Hazards for Performance-Based Earthquake Engineering*. Steven L. Kramer and Ahmed-W. Elgamal. February 2001.

PEER 2001/12 *Development of Geotechnical Capabilities in OpenSees*. Boris Jeremić. September 2001.

PEER 2001/11 *Analytical and Experimental Study of Fiber-Reinforced Elastomeric Isolators*. James M. Kelly and Shakhzod M. Takhirov. September 2001.

PEER 2001/10 *Amplification Factors for Spectral Acceleration in Active Regions.* Jonathan P. Stewart, Andrew H. Liu, Yoojoong Choi, and Mehmet B. Baturay. December 2001.

PEER 2001/09 *Ground Motion Evaluation Procedures for Performance-Based Design.* Jonathan P. Stewart, Shyh-Jeng Chiou, Jonathan D. Bray, Robert W. Graves, Paul G. Somerville, and Norman A. Abrahamson. September 2001.

PEER 2001/08 *Experimental and Computational Evaluation of Reinforced Concrete Bridge Beam-Column Connections for Seismic Performance*. Clay J. Naito, Jack P. Moehle, and Khalid M. Mosalam. November 2001.

PEER 2001/07 *The Rocking Spectrum and the Shortcomings of Design Guidelines.* Nicos Makris and Dimitrios Konstantinidis. August 2001.

PEER 2001/06 *Development of an Electrical Substation Equipment Performance Database for Evaluation of Equipment Fragilities*. Thalia Agnanos. April 1999.

PEER 2001/05 *Stiffness Analysis of Fiber-Reinforced Elastomeric Isolators.* Hsiang-Chuan Tsai and James M. Kelly. May 2001.

PEER 2001/04 *Organizational and Societal Considerations for Performance-Based Earthquake Engineering*. Peter J. May. April 2001.

PEER 2001/03 *A Modal Pushover Analysis Procedure to Estimate Seismic Demands for Buildings: Theory and Preliminary Evaluation*. Anil K. Chopra and Rakesh K. Goel. January 2001.

PEER 2001/02 *Seismic Response Analysis of Highway Overcrossings Including Soil-Structure Interaction*. Jian Zhang and Nicos Makris. March 2001.

PEER 2001/01 *Experimental Study of Large Seismic Steel Beam-to-Column Connections.* Egor P. Popov and Shakhzod M. Takhirov. November 2000.

PEER 2000/10 *The Second U.S.-Japan Workshop on Performance-Based Earthquake Engineering Methodology for Reinforced Concrete Building Structures*. March 2000.

PEER 2000/09 *Structural Engineering Reconnaissance of the August 17, 1999 Earthquake: Kocaeli (Izmit), Turkey.* Halil Sezen, Kenneth J. Elwood, Andrew S. Whittaker, Khalid Mosalam, John J. Wallace, and John F. Stanton. December 2000.

PEER 2000/08 *Behavior of Reinforced Concrete Bridge Columns Having Varying Aspect Ratios and Varying Lengths of Confinement.* Anthony J. Calderone, Dawn E. Lehman, and Jack P. Moehle. January 2001.

PEER 2000/07 *Cover-Plate and Flange-Plate Reinforced Steel Moment-Resisting Connections.* Taejin Kim, Andrew S. Whittaker, Amir S. Gilani, Vitelmo V. Bertero, and Shakhzod M. Takhirov. September 2000.

PEER 2000/06 *Seismic Evaluation and Analysis of 230-kV Disconnect Switches.* Amir S. J. Gilani, Andrew S. Whittaker, Gregory L. Fenves, Chun-Hao Chen, Henry Ho, and Eric Fujisaki. July 2000.

PEER 2000/05 *Performance-Based Evaluation of Exterior Reinforced Concrete Building Joints for Seismic Excitation*. Chandra Clyde, Chris P. Pantelides, and Lawrence D. Reaveley. July 2000.

PEER 2000/04 *An Evaluation of Seismic Energy Demand: An Attenuation Approach*. Chung-Che Chou and Chia-Ming Uang. July 1999.

PEER 2000/03 *Framing Earthquake Retrofitting Decisions: The Case of Hillside Homes in Los Angeles.* Detlof von Winterfeldt, Nels Roselund, and Alicia Kitsuse. March 2000.

PEER 2000/02 *U.S.-Japan Workshop on the Effects of Near-Field Earthquake Shaking*. Andrew Whittaker, Editor. July 2000.

PEER 2000/01 *Further Studies on Seismic Interaction in Interconnected Electrical Substation Equipment.* Armen Der Kiureghian, Kee-Jeung Hong, and Jerome L. Sackman. November 1999.

PEER 1999/14 *Seismic Evaluation and Retrofit of 230-kV Porcelain Transformer Bushings*. Amir S. Gilani, Andrew S. Whittaker, Gregory L. Fenves, and Eric Fujisaki. December 1999.

PEER 1999/13 *Building Vulnerability Studies: Modeling and Evaluation of Tilt-up and Steel Reinforced Concrete Buildings*. John W. Wallace, Jonathan P. Stewart, and Andrew S. Whittaker, Editors. December 1999.

PEER 1999/12 *Rehabilitation of Nonductile RC Frame Building Using Encasement Plates and Energy-Dissipating Devices*. Mehrdad Sasani, Vitelmo V. Bertero, James C. Anderson. December 1999.

PEER 1999/11 *Performance Evaluation Database for Concrete Bridge Components and Systems under Simulated Seismic Loads*. Yael D. Hose and Frieder Seible. November 1999.

PEER 1999/10 *U.S.-Japan Workshop on Performance-Based Earthquake Engineering Methodology for Reinforced Concrete Building Structures*. December 1999.

PEER 1999/09 *Performance Improvement of Long Period Building Structures Subjected to Severe Pulse-Type Ground Motions*. James C. Anderson, Vitelmo V. Bertero, and Raul Bertero. October 1999.

PEER 1999/08 *Envelopes for Seismic Response Vectors.* Charles Menun and Armen Der Kiureghian. July 1999.

PEER 1999/07 *Documentation of Strengths and Weaknesses of Current Computer Analysis Methods for Seismic Performance of Reinforced Concrete Members*. William F. Cofer. November 1999.

PEER 1999/06 *Rocking Response and Overturning of Anchored Equipment under Seismic Excitations*. Nicos Makris and Jian Zhang. November 1999.

PEER 1999/05 *Seismic Evaluation of 550 kV Porcelain Transformer Bushings.* Amir S. Gilani, Andrew S. Whittaker, Gregory L. Fenves, and Eric Fujisaki. October 1999.

PEER 1999/04 *Adoption and Enforcement of Earthquake Risk-Reduction Measures*. Peter J. May, Raymond J. Burby, T. Jens Feeley, and Robert Wood. August 1999.

PEER 1999/03 *Task 3 Characterization of Site Response General Site Categories*. Adrian Rodriguez-Marek, Jonathan D. Bray and Norman Abrahamson. February 1999.

PEER 1999/02 *Capacity-Demand-Diagram Methods for Estimating Seismic Deformation of Inelastic Structures: SDF Systems*. Anil K. Chopra and Rakesh Goel. April 1999.

PEER 1999/01 *Interaction in Interconnected Electrical Substation Equipment Subjected to Earthquake Ground Motions*. Armen Der Kiureghian, Jerome L. Sackman, and Kee-Jeung Hong. February 1999.

PEER 1998/08 *Behavior and Failure Analysis of a Multiple-Frame Highway Bridge in the 1994 Northridge Earthquake*. Gregory L. Fenves and Michael Ellery. December 1998.

PEER 1998/07 *Empirical Evaluation of Inertial Soil-Structure Interaction Effects.* Jonathan P. Stewart, Raymond B. Seed, and Gregory L. Fenves. November 1998.

PEER 1998/06 *Effect of Damping Mechanisms on the Response of Seismic Isolated Structures*. Nicos Makris and Shih-Po Chang. November 1998.

PEER 1998/05 *Rocking Response and Overturning of Equipment under Horizontal Pulse-Type Motions*. Nicos Makris and Yiannis Roussos. October 1998.

PEER 1998/04 *Pacific Earthquake Engineering Research Invitational Workshop Proceedings, May 14–15, 1998: Defining the Links between Planning, Policy Analysis, Economics and Earthquake Engineering*. Mary Comerio and Peter Gordon. September 1998.

PEER 1998/03 *Repair/Upgrade Procedures for Welded Beam to Column Connections*. James C. Anderson and Xiaojing Duan. May 1998.

PEER 1998/02 *Seismic Evaluation of 196 kV Porcelain Transformer Bushings.* Amir S. Gilani, Juan W. Chavez, Gregory L. Fenves, and Andrew S. Whittaker. May 1998.

PEER 1998/01 *Seismic Performance of Well-Confined Concrete Bridge Columns.* Dawn E. Lehman and Jack P. Moehle. December 2000.

PEER REPORTS: ONE HUNDRED SERIES

The following PEER reports are available by Internet only at http://peer.berkeley.edu/publications/peer_reports_complete.html.

PEER 2012/103 *Performance-Based Seismic Demand Assessment of Concentrically Braced Steel Frame Buildings.* Chui-Hsin Chen and Stephen A. Mahin. December 2012.

PEER 2012/102 *Procedure to Restart an Interrupted Hybrid Simulation: Addendum to PEER Report 2010/103.* Vesna Terzic and Bozidar Stojadinovic. October 2012.

PEER 2012/101 *Mechanics of Fiber Reinforced Bearings.* James M. Kelly and Andrea Calabrese. February 2012.

PEER 2011/107 *Nonlinear Site Response and Seismic Compression at Vertical Array Strongly Shaken by 2007 Niigata-ken Chuetsu-oki Earthquake.* Eric Yee, Jonathan P. Stewart, and Kohji Tokimatsu. December 2011.

PEER 2011/106 *Self Compacting Hybrid Fiber Reinforced Concrete Composites for Bridge Columns.* Pardeep Kumar, Gabriel Jen, William Trono, Marios Panagiotou, and Claudia Ostertag. September 2011.

PEER 2011/105 *Stochastic Dynamic Analysis of Bridges Subjected to Spacially Varying Ground Motions.* Katerina Konakli and Armen Der Kiureghian. August 2011.

PEER 2011/104 *Design and Instrumentation of the 2010 E-Defense Four-Story Reinforced Concrete and Post-Tensioned Concrete Buildings.* Takuya Nagae, Kenichi Tahara, Taizo Matsumori, Hitoshi Shiohara, Toshimi Kabeyasawa, Susumu Kono, Minehiro Nishiyama (Japanese Research Team) and John Wallace, Wassim Ghannoum, Jack Moehle, Richard Sause, Wesley Keller, Zeynep Tuna (U.S. Research Team). June 2011.

PEER 2011/103 *In-Situ Monitoring of the Force Output of Fluid Dampers: Experimental Investigation.* Dimitrios Konstantinidis, James M. Kelly, and Nicos Makris. April 2011.

PEER 2011/102 *Ground-Motion Prediction Equations 1964–2010.* John Douglas. April 2011.

PEER 2011/101 *Report of the Eighth Planning Meeting of NEES/E-Defense Collaborative Research on Earthquake Engineering.* Convened by the Hyogo Earthquake Engineering Research Center (NIED), NEES Consortium, Inc. February 2011.

PEER 2010/111 *Modeling and Acceptance Criteria for Seismic Design and Analysis of Tall Buildings.* Task 7 Report for the Tall Buildings Initiative - Published jointly by the Applied Technology Council. October 2010.

PEER 2010/110 *Seismic Performance Assessment and Probabilistic Repair Cost Analysis of Precast Concrete Cladding Systems for Multistory Buildlings.* Jeffrey P. Hunt and Božidar Stojadinovic. November 2010.

PEER 2010/109 *Report of the Seventh Joint Planning Meeting of NEES/E-Defense Collaboration on Earthquake Engineering. Held at the E-Defense, Miki, and Shin-Kobe, Japan, September 18–19, 2009.* August 2010.

PEER 2010/108 *Probabilistic Tsunami Hazard in California.* Hong Kie Thio, Paul Somerville, and Jascha Polet, preparers. October 2010.

PEER 2010/107 *Performance and Reliability of Exposed Column Base Plate Connections for Steel Moment-Resisting Frames.* Ady Aviram, Božidar Stojadinovic, and Armen Der Kiureghian. August 2010.

PEER 2010/106 *Verification of Probabilistic Seismic Hazard Analysis Computer Programs.* Patricia Thomas, Ivan Wong, and Norman Abrahamson. May 2010.

PEER 2010/105 *Structural Engineering Reconnaissance of the April 6, 2009, Abruzzo, Italy, Earthquake, and Lessons Learned.* M. Selim Günay and Khalid M. Mosalam. April 2010.

PEER 2010/104 *Simulating the Inelastic Seismic Behavior of Steel Braced Frames, Including the Effects of Low-Cycle Fatigue.* Yuli Huang and Stephen A. Mahin. April 2010.

PEER 2010/103 *Post-Earthquake Traffic Capacity of Modern Bridges in California.* Vesna Terzic and Božidar Stojadinović. March 2010.

PEER 2010/102 *Analysis of Cumulative Absolute Velocity (CAV) and JMA Instrumental Seismic Intensity (I_{JMA}) Using the PEER–NGA Strong Motion Database.* Kenneth W. Campbell and Yousef Bozorgnia. February 2010.

PEER 2010/101 *Rocking Response of Bridges on Shallow Foundations.* Jose A. Ugalde, Bruce L. Kutter, and Boris Jeremic. April 2010.

PEER 2009/109 *Simulation and Performance-Based Earthquake Engineering Assessment of Self-Centering Post-Tensioned Concrete Bridge Systems.* Won K. Lee and Sarah L. Billington. December 2009.

PEER 2009/108 *PEER Lifelines Geotechnical Virtual Data Center.* J. Carl Stepp, Daniel J. Ponti, Loren L. Turner, Jennifer N. Swift, Sean Devlin, Yang Zhu, Jean Benoit, and John Bobbitt. September 2009.

PEER 2009/107 *Experimental and Computational Evaluation of Current and Innovative In-Span Hinge Details in Reinforced Concrete Box-Girder Bridges: Part 2: Post-Test Analysis and Design Recommendations.* Matias A. Hube and Khalid M. Mosalam. December 2009.

PEER 2009/106 *Shear Strength Models of Exterior Beam-Column Joints without Transverse Reinforcement.* Sangjoon Park and Khalid M. Mosalam. November 2009.

PEER 2009/105 *Reduced Uncertainty of Ground Motion Prediction Equations through Bayesian Variance Analysis.* Robb Eric S. Moss. November 2009.

PEER 2009/104 *Advanced Implementation of Hybrid Simulation.* Andreas H. Schellenberg, Stephen A. Mahin, Gregory L. Fenves. November 2009.

PEER 2009/103 *Performance Evaluation of Innovative Steel Braced Frames.* T. Y. Yang, Jack P. Moehle, and Božidar Stojadinovic. August 2009.

PEER 2009/102 *Reinvestigation of Liquefaction and Nonliquefaction Case Histories from the 1976 Tangshan Earthquake.* Robb Eric Moss, Robert E. Kayen, Liyuan Tong, Songyu Liu, Guojun Cai, and Jiaer Wu. August 2009.

PEER 2009/101 *Report of the First Joint Planning Meeting for the Second Phase of NEES/E-Defense Collaborative Research on Earthquake Engineering.* Stephen A. Mahin et al. July 2009.

PEER 2008/104 *Experimental and Analytical Study of the Seismic Performance of Retaining Structures.* Linda Al Atik and Nicholas Sitar. January 2009.

PEER 2008/103 *Experimental and Computational Evaluation of Current and Innovative In-Span Hinge Details in Reinforced Concrete Box-Girder Bridges. Part 1: Experimental Findings and Pre-Test Analysis.* Matias A. Hube and Khalid M. Mosalam. January 2009.

PEER 2008/102 *Modeling of Unreinforced Masonry Infill Walls Considering In-Plane and Out-of-Plane Interaction.* Stephen Kadysiewski and Khalid M. Mosalam. January 2009.

PEER 2008/101 *Seismic Performance Objectives for Tall Buildings.* William T. Holmes, Charles Kircher, William Petak, and Nabih Youssef. August 2008.

PEER 2007/101 *Generalized Hybrid Simulation Framework for Structural Systems Subjected to Seismic Loading*. Tarek Elkhoraibi and Khalid M. Mosalam. July 2007.

PEER 2007/100 *Seismic Evaluation of Reinforced Concrete Buildings Including Effects of Masonry Infill Walls.* Alidad Hashemi and Khalid M. Mosalam. July 2007.

The Pacifi c Earthquake Engineering Research Center (PEER) is a multi-institutional research and education center with headquarters at the University of California, Berkeley. Investigators from over 20 universities, several consulting companies, and researchers at various state and federal government agencies contribute to research programs focused on performance-based earthquake engineering.

These research programs aim to identify and reduce the risks from major earthquakes to life safety and to the economy by including research in a wide variety of disciplines including structural and geotechnical engineering, geology/seismology, lifelines, transportation, architecture, economics, risk management, and public policy.

PEER is supported by federal, state, local, and regional agencies, together with industry partners.

PEER Core Institutions

University of California, Berkeley (Lead Institution)
California Institute of Technology
Oregon State University
Stanford University
University of California, Davis
University of California, Irvine
University of California, Los Angeles
University of California, San Diego
University of Nevada, Reno
University of Southern California
University of Washington

PEER reports can be ordered at https://peer.berkeley.edu/peer-reports or by contacting

Pacific Earthquake Engineering Research Center
University of California, Berkeley
325 Davis Hall, Mail Code 1792
Berkeley, CA 94720-1792
Tel: 510-642-3437
Email: peer_center@berkeley.edu

ISSN 2770-8314
https://doi.org/10.55461/NSOS1322